Die approbierte Originalversion dieser Dissertation ist in der Hauptbibliothek der Technischen Universität Wien aufgestellt und zugänglich.
http://www.ub.tuwien.ac.at

The approved original version of this thesis is available at the main library of the Vienna University of Technology.
http://www.ub.tuwien.ac.at/eng

Dissertation

Near Ambient Pressure Spectroscopy on UHV-grown Model Systems of Reforming Catalysts: CO, H_2O and CO_2 on Ultrathin Zirconia Layers

ausgeführt zum Zwecke der Erlangung des akademischen Grades eines Doktors der technischen Wissenschaften unter der Leitung von

Univ.Prof. Mag.rer.nat. Dr.rer.nat. Günther Rupprechter

und

Dr.rer.nat. Christoph Rameshan

Institut für Materialchemie E165

eingereicht an der Technischen Universität Wien

Fakultät für Technische Chemie

von

MSc. Hao Li

Matrikelnummer: 1129503

Kleistgasse 31/22

1030 Wien

Wien, am 08.06.2015

Zusammenfassung

Ziel dieser Arbeit war die Untersuchung der Eigenschaften von ultradünnen Zirkondioxidfilmen (ZrO_2) als Supportmaterial für Modellkatalysatoren, welche für die Dampfreformierung von Methanol (Methanol Steam Reforming, MSR) Frage kommen.

Die Untersuchungen erfolgten im Ultrahochvakuum (UHV) mittels Röntgenphotoelektronenspektroskopie (X-ray Photoelectron Spectroscopy, XPS), Beugung niederenergetischer Elektronen an Oberflächen (Low Energy Electron Diffraction, LEED), Infrarot-Reflexions-Absorptions-Spektroskopie (Infrared Reflection Adsorption Spectroscopy, IRAS) und Temperatur-programmierter Desorption (Temperature Programmed Desorption, TPD).

In situ Untersuchungen mittels Synchrotron-Röntgenphotoelektronenspektroskopie nahe dem Umgebungsdruck (Near Ambient Pressure, NAP-XPS) wurden eingesetzt, um auch den für die angewandte Katalyse relevanteren Bereich höherer Drücke abzudecken.

Ergänzt wurden die erhaltenen Resultate durch Rastertunnelmikroskopie (Scanning Tunneling Microscopy, STM) und Dichtefunktionaltheorie (Density Functional Theory, DFT), welche von Kooperationspartnern des vom FWF finanzierten SFB FOXSI Projekts (Functional Oxide Surfaces and Interfaces) durchgeführt wurden.

Zunächst wurde **das Wachstum von ultradünnen ZrO_2 Filmen auf Pt_3Zr Einkristallen** untersucht. Dabei bildete sich auf der Oberfläche eine vollständige Oxidschicht, welche sowohl aus einem dreilagigen O−Zr−O Film, als auch aus Oxidclustern (ca. 10-15% der Oberfläche) bestand. Die chemische Verschiebung des Zr betrug +2,1 eV (gegenüber reinem Zr) für den O−Zr−O Film und +4,2 eV für die Oxidcluster.

Beim Erhitzen konnte die Zersetzung der Oxidcluster unter Bildung des dreilagigen O-Zr-O Films beobachtet werden.

Die Wechselwirkung zwischen D_2O (bzw. H_2O) und dem O−Zr−O Film wurde im Anschluss daran untersucht. D_2O adsorbiert auf reinem ZrO_2 sowohl in molekularer Form, als auch unter Dissoziation, wobei D_2O unter Rekombination von der Oberfläche desorbiert. Auf einem Oxidfilm mit Fehlstellen ("softly sputtered") adsorbiert D_2O ebenfalls sowohl molekular, als auch unter Dissoziation, allerdings erfolgt die anschließende Desorption ohne Rekombination. Diese Effekte wurden als Funktion des Drucks mittels NAP-XPS bestimmt, jedoch wurde auch die durch Röntgenstrahlung induzierte Desorption beobachtet.

Abschließend wurde **die Aktivierung von CO_2 auf ultradünnen ZrO_2 Filmen** untersucht. Es zeigte sich, dass CO_2 unter UHV Bedingungen nur schwach auf den hergestellten Filmen adsorbiert. Die mittels TPD bestimmte Desorptionstemperatur betrug 117 K. Bei höheren Drücken im Bereich von einigen mbar, konnte keine Adsorption von CO_2 bei 343 K beobachtet werden. Die Kodosierung von H_2O führte zur Aktivierung von CO_2. Mittels NAP-XPS konnte - nach Exposition des ultradünnen ZrO_2 Films mit CO_2 und H_2O - die Bildung von H_x−C−O und O−C=O Spezies beobachtet werden, wobei Zr^{4+} teilweise zu Zr_x reduziert wurde. IRAS Messungen zeigten - nach Dosierung der CO_2/H_2O Reaktionsmischung - ebenfalls die Anwesenheit von H_x−C−O und O−C=O Spezies auf der Oberfläche. Durch Referenzmessungen mit Ameisensäure (HCOOH) und Formaldehyd (HCHO) konnten diese H_2−C−O und COOH zugeordnet werden. Des Weiteren konnte mit NAP-XPS gezeigt werden, dass COOH thermisch weniger stabil ist als H_2−C−O.

Beim Abkühlen der Probe in der Reaktionsmischung wurde die reversible Bildung der desorbierten/dissoziierten COOH und H_2−C−O Spezies beobachtet.

Abstract

The aim of this thesis was to investigate the properties of an ultrathin zirconium dioxide (ZrO_2) film, intended to serve as a well-defined supporting oxide for a model reforming catalyst. For ultrahigh vacuum (UHV) characterization of the model system, both lab-based and synchrotron-based X-ray Photoelectron Spectroscopy (XPS), Low Energy Electron Diffraction (LEED), Infrared Reflection Adsorption Spectroscopy (IRAS) and Temperature Programmed Desorption (TPD) have been employed as combined techniques. For in situ studies in the mbar pressure range, both lab-based and synchrotron-based (Near Ambient Pressure) NAP-XPS have been applied to study the model system under catalytically relevant conditions. The experimental findings of this thesis were complemented by Scanning Tunneling Microscopy (STM) and Density Functional Theory (DFT), performed by collaboration partners with the FWF funded SFB FOXSI (Functional Oxide Surfaces and Interfaces).

The growth of an ultrathin ZrO_2 film on a Pt_3Zr single crystal substrate was studied first. The formed oxide fully covers the substrate and has two rotational domains. Furthermore, the oxide overlayer consists of a trilayer film (O-Zr-O) as well as of oxide clusters (the latter covering about 10-15% of the surface). These two species have different core level shifts relative to pure Zr, i.e. +2.1 eV for the trilayer film and +4.2 eV for the clusters. Upon increasing the post-annealing temperature of the film, the oxide clusters more and more decompose, leading to the O-Zr-O trilayer film.

The interaction of D_2O (or H_2O) with the ultrathin ZrO_2 trilayer film was investigated second. D_2O adsorbs on pristine ZrO_2 both molecularly and dissociatively, and the dissociated

D_2O desorbs recombinatively from the pristine oxide surface. On a ("softly sputtered") defective oxide, D_2O also adsorbs both molecularly and dissociatively, with the latter increased, but the D_2O dissociated on the defects quenches the defects and desorbs non-recombinatively. All effects were examined as a function of pressure by NAP-XPS. However, X-ray-induced desorption of D_2O (or H_2O) was observed in for lab-based and synchrotron-based XPS measurements.

The activation of CO_2 by the ultrathin ZrO_2 film was examined third. The results show that CO_2 adsorbs only weakly on the ultrathin ZrO_2 film under UHV conditions and desorbs at 117 K according to TPD. At elevated (mbar) pressure, CO_2 alone does not adsorb on the ZrO_2 ultrathin film at 343 K. However, CO_2 can be activated by co-dosed H_2O (even trace amounts). In situ NAP-XPS detected the formation of H_x-C-O and O-C=O species when ZrO_2 ultrathin films were subjected to CO_2 and H_2O reaction mixtures. By forming such C-containing species, Zr^{4+} within the ultrathin ZrO_2 film is partially converted to Zr_x. IRAS measurements of formic acid HCOOH and formaldehyde HCHO adsorption revealed the typical adsorption bands of the relevant functional groups. By using them as reference, the H_x-C-O and O-C=O IRAS bands observed on the surface upon dosing CO_2 and H_2O reaction mixtures were assigned to H_2-C-O and COOH. In situ NAP-XPS also showed that the thermal stability of COOH species was smaller than that of H_2-C-O. After cooling the sample in the reaction (CO_2 and H_2O) mixture, the desorbed/decomposed COOH and H_2-C-O species were formed reversibly.

Acknowledgement

The presented thesis is a summary of my scientific research conducted in the course of my PhD study from April 2012 to April 2015. The work has been funded by the FWF Spezialforschungsbereich (SFB) Functional Oxide Surfaces and Interfaces (FOXSI)) program. The chapters represent papers that were published by or are being prepared for international journals and conference proceedings.

I would like to thank many *wonderful* people who have supported me during my entire doctoral work:

Prof. Günther Rupprechter for the continuous support and his precious guidance, as well as for the opportunity he gave me to conduct my thesis;

Prof. Michael Schmid for being my second examiner and for reading my thesis, as well as for many stimulating and illuminating discussions and support throughout the thesis;

Dr. Christoph Rameshan and Dr. Christian Weilach for being my direct scientific advisors, for their support and instruction on a daily basis, as well as for the trust and encouragement they gave to me to design and conduct my experiments;

Dr. Harald Holzapfel for introducing me to the experimental setup; **Kresimir Anic** for offering me helping hands in the lab and for countless interesting discussions; **Martin Datler** and **Ivan Bespalov** for sharing the lab, as well as the tools from time to time; **Dr. Andrey V. Bukhtiyarov** for sharing his precious knowledge on UHV systems and his very warm hospitality in Novosibirsk;

Liliana Lukashuk for sharing office and snacks, for being the bridge to the world of "real catalysts";

Rainald Rosner, Johannes Frank and **Rupert Kleinl** for all the technical support;

Melanie Schärer and **Anita Demaj** for helping me dealing with all kinds of paper work;

and **all other colleagues** in the Institute of Materials Chemistry at TU Vienna;

Jake Choi and Wernfried Mayr-Schmölzer in the Institute of Applied Physics at TU Vienna for fruitful collaborations;

my **Chinese friends** here in Vienna for supporting me through good and bad times;

my **parents**, for offering me their endless love and great encouragement, although they are far away from me.

Table of Contents

Zusammenfassung i

Abstract iii

Acknowledgement v

1. Introduction 10

2. Techniques 19

2.1. X-ray Photoelectron Spectroscopy (XPS) 19

2.1.1. In situ (Near Ambient Pressure) NAP-XPS at elevated pressure 23

2.2. Infrared Spectroscopy 25

2.2.1. Theory of molecular vibrations 25

2.2.2. Fourier-Transform Infrared (FTIR) Spectroscopy 27

2.2.3. Infrared Reflection-Absorption Spectroscopy (IRAS) 29

2.3. Low Energy Electron Diffraction (LEED) 32

2.4. Temperature programmed desorption (TPD) 36

2.5. Vienna Set-up 38

3. Growth of ZrO_2 model ultrathin films on Pt_3Zr 44

3.1. Introduction 44

3.2. Experimental 45

3.3. Results and discussion 46

3.3.1. The trilayer oxide: LEED and CO TPD 46

3.3.2. Core level shifts: two oxide species 51

3.3.3. Influence of the annealing temperature 57

3.4. Summary 62

4. Interaction of Water with Ultrathin ZrO_2 Films 66

4.1. Introduction 66

4.2. Experimental 67

4.3. Results and discussion 68

4.3.1. Characterization of pristine and defect-enriched oxide films 68

4.3.2. D2O-TPD: high temperature desorption features 72

4.3.3. XPS: molecularly and dissociatively adsorbed D_2O 74

4.3.4. IRAS 82

4.3.5. NAP-XPS: dissociation of x-ray induced desorption 85

4.4. Summary 87

5. CO_2 and H_2O (co)Adsorption on a ZrO_2 Thin Film 92

5.1. Introduction 92

5.2. Experimental 92

5.3. Results and discussion 93

5.3.1. CO_2 TPD 93

5.3.2. Synchrotron-based in situ NAP-XPS measurements of CO_2 adsorption 95

5.3.3. Lab-based in situ NAP-XPS measurement of CO_2 adsorption, and CO_2 and H_2O co-adsorption 97

5.3.4. IRAS measurements of HCOOH and HCHO adsorption 102

5.3.5. IRAS measurements of CO_2 and H_2O co-adsorption 104

5.4. Summary 106

6. Conclusions 109

Publications 113

CURRICULUM VITAE ..... **Error! Bookmark not defined.**

1. Introduction

Metal oxides are of great importance in various areas of materials chemistry. Their applications encompass optoelectronics, sensors, reflective and protective coatings, as well as energy and environment-related catalysis. Particularly in catalysis metal oxides can be used as active catalysts or as support material for dispersing the active metal particles.[1] There the surface properties of the oxide materials, and rather the surface than the bulk properties play a major role. In order to understand the surface properties and to correlate them with their function in catalytic reactions, studies of metal oxides at an atomic level are crucial. However, industrial-grade powder materials often exhibit high porosity, poorly defined structures and morphology which is typically not suited for fundamental investigations at an atomic or molecular level.[2] Such drawbacks can be overcome by studying model metal oxides grown under ultrahigh vacuum (UHV) conditions. In contrast to industrially used oxides, they exhibit well-defined chemical and morphological properties as well as nonporous surfaces. Model surfaces of metal oxides which are studied in surface science can be roughly divided into three classes: a) oxide single crystals; b) ultrathin oxide films; and c) oxide layers that are formed on the top of the metal itself.[3] A drawback for the research on metal oxides is often their bad electric conductivity, which causes serve complications in sample characterization by spectroscopy. Among the oxide materials, ultrathin oxide films exhibit both enough conductivity and good planarity, and thus they allow us to use the whole arsenal of surface science techniques.[4] In addition, one can easily tune the chemical composition and defect concentration of the ultrathin oxide films by changing the preparation conditions.[5] The

complexity of the models can be further increased by growing metal nanoparticles on the surface of ultrathin oxide films at UHV conditions, what allows us to even study oxide supported metal catalysts. Such model systems offer the advantage of fully controllable parameters, while they still can be investigated by all kinds of surface science techniques to correlate electronic and geometrical properties with catalytic behavior. Comparing with traditionally used single crystal surfaces, the so called materials gap can be also bridged. In addition, experimental results obtained from such well-defined model system can be directly compared with density functional theory (DFT) calculations.

Traditionally surface science studies have been mainly performed under UHV conditions or low pressures (up to 10^{-6} mbar), whereas most catalytic reactions usually take place at pressures in the range of 1~100 bar. The difference between UHV and industrial conditions is known as the "pressure gap". The "pressure gap" makes it difficult to extrapolate the results obtained from surface science studies under UHV conditions to real catalysis. It has been shown that adsorbates can form new structures under high pressure exceeding the saturation coverage obtained under UHV.[6,7] It has been also reported that species formed under low pressure conditions can be removed by reacting with gas phase molecules at elevated pressures at a given temperature.[8] In addition, at elevated pressures and temperatures a reconstruction of the catalyst surface may occur.[9,10]

In the last decade strong efforts have been made to bridge the prominent "pressure gap" by developing experimental surface specific techniques, which can provide spectroscopic and microscopic information of model catalysts in a wide pressure range from UHV to ambient conditions. For example, X-ray Absorption Spectroscopy (XAS),[11] Near Ambient Pressure X-ray Photoelectron Spectroscopy (NAP-XPS),[12] High Pressure Scanning Tunneling Microscopy (HP-STM),[6] Sum Frequency Generation (SFG) spectroscopy[2] and Polarization-Modulation Infrared Reflection Absorption Spectroscopy (PM-IRAS)[2] have been developed

to detect chemical composition and structure of the surface and of adsorbates bound to the surface, both under UHV and under high pressure conditions.

In this thesis Zirconia (ZrO_2) was chosen to be investigated as a core material, which is widely used in heterogeneous catalysis and known as an excellent support material. Furthermore it can act as a catalysts itself, due to its favorable chemical and mechanical stability.[13] However, single-crystal ZrO_2 exhibits poor electrical conductivity and is prone to charging, which usually hinders the application of many surface science techniques.[14] On the other hand, thin ZrO_2 films, which were prepared by depositing and oxidizing zirconium (Zr) on a suitable single crystal substrate, usually contain a substantial amount of defects.[15] Lately, an alternative route to ultrathin ZrO_2 films via oxidation of a $Pt_3Zr(0001)$ alloy single crystal has been reported by Antlanger et al.[16] Their STM study showed that a planar oxide film (almost defect free) consisting of an O-Zr-O trilayer was formed. The starting point of this thesis was the examination of the mechanism of formation and of the structure of ultrathin ZrO_2 films grown on a $Pt_3Zr(0001)$ single crystal by oxidation and post-annealing. This work was intended to get a better understanding of the involved processes. One crucial issue regarding the growth of a thin film oxide on a substrate is its continuity. For following systematic adsorption/reactivity studies the model oxide should entirely cover the substrate. Therefore, when a complete coverage is suggested by extended STM studies (local technique), the results should be corroborated by an integral method such as temperature-programmed desorption (TPD) (for example with CO as probe molecule). Another general concern regarding ultrathin films is whether their stoichiometry and electronic structure represents the bulk material. Therefore, the model ZrO_2 ultrathin film was also investigated by synchrotron-based high resolution XPS (HR-XPS) (including depth profiling) and low-energy electron diffraction (LEED).

After a detailed characterization of the initial state of the model system, the adsorption of water (D_2O or H_2O) on the ultrathin ZrO_2 film (both in its pristine and defect-enriched (sputtered) state) was investigated. Hydroxyl groups are of paramount importance in surface chemistry and catalysis, for instance, they can directly participate in reactions,[17] or affect the size (dispersion) and the structure of the metal nanoparticles grown on oxides.[18,19] It has also been shown that both the defects on the oxide surface[20] as well as the water pressure influence the hydroxylation process.[21] Therefore, the interaction of water with pristine and defective ZrO_2 was studied in a pressure regime from UHV to 10^{-3} mbar by applying lab-based and synchrotron-based (NAP-)XPS, TPD, and Infrared Reflection Absorption Spectroscopy (IRAS).

As a next step, the interaction between CO_2 and the ultrathin ZrO_2 film was examined. Being a carbon source, the utilization of carbon dioxide (CO_2) has become attractive from both an environmental and economic point of view. However, CO_2 is a very stable molecule, thus, to induce a reaction the activation of CO_2 by a catalyst is required. One way of activating CO_2 is dry reforming of methane (DRM), when CH_4 is reformed by CO_2 on Ni or Pt particles supported by ZrO_2.

$$CH_4+CO_2 \leftrightarrow 2H_2+2CO$$

During DRM, CO_2 is reduced to carbon monoxide (CO) via reaction precursors or intermediates, the released O can further oxidize the carbon formed via CH_4 dissociation. Such activation can occur on the ZrO_2 or on the interfacial sites.[22] As a support, technical ZrO_2 powder material can activate CO_2 by forming carbonate with basic anionic sites, or by forming formate with hydroxyl groups. Therefore, systematic studies of the interaction between CO_2 and a pristine ZrO_2 ultra-thin film (CO_2 adsorption on ZrO_2) as well as the

interaction between CO_2 and a hydroxylated ZrO_2 ultra-thin film (CO_2 and H_2O co-adsorption) were carried out.

The thesis is organized as follows: chapter 2 introduces the basics of the main techniques which were used throughout the thesis. The experimental setup employed in this work is then shortly described. Chapter 3 deals with the preparation of the ultrathin ZrO_2 film on a $Pt_3Zr(0001)$ single crystal. First of all the different CO adsorption behavior on the $Pt_3Zr(0001)$ and on the ultrathin ZrO_2 film is described. Second, the core level shifts of Zr 3d and O 1s monitored by synchrotron-based HR-XPS is discussed. Based on the calculated stoichiometry and the depth profiling results, the co-existence of an ultrathin ZrO_2 film and 3-dimensional ZrO_2 clusters is proposed. Finally, the influence of annealing temperature on the two ZrO_2 species (film and clusters) is mentioned.

Chapter 4 is dedicated to the water adsorption on the ultrathin ZrO_2 film. The characterization of the $Pt_3Zr(0001)$ substrate, the pristine ZrO_2 and the defective ZrO_2 by XPS, LEED and CO TPD is firstly introduced. Then investigations of different D_2O related species formed on both ultrathin pristine and defective ZrO_2 films using TPD, XPS and IRAS are presented. Finally, the influence of water pressure on the hydroxylation of the ZrO_2 film, probed by synchrotron-based in-situ XPS, is shown.

Chapter 5 is focused on the CO_2 and H_2O (co)adsorption on the ultrathin ZrO_2 film. First, CO_2 adsorption on the ultrathin ZrO_2 film, examined by lab-based in-situ XPS, is presented. Thereafter, the interaction between CO_2 and a hydroxylated ZrO_2 ultrathin film (CO_2 and H_2O co-adsorption) studied by both lab-based in-situ XPS and IRAS follows. The vibrational frequencies for the measured absorption bands induced by CO_2 and H_2O co-adsorption is compared to the reference data obtained by measuring formic acid (HCOOH) and formaldehyde (HCHO) dosed on the ultrathin ZrO_2 film. At the end, the most important findings and results of this thesis are summarized in Chapter 6.

Bibiliography

1. (a) Shaikhutdinov, S.; Freund, H. J., Ultrathin Oxide Films on Metal Supports: Structure-Reactivity Relations. *Annual Review of Physical Chemistry* **2012,** *63* (1), 619-633; (b) Hayek, K.; Fuchs, M.; Klötzer, B.; Reichl, W.; Rupprechter, G., Studies of metal–support interactions with "real" and "inverted" model systems: reactions of CO and small hydrocarbons with hydrogen on noble metals in contact with oxides. *Topics in Catalysis* **2000,** *13* (1-2), 55-66; (c) Dellwig, T.; Hartmann, J.; Libuda, J.; Meusel, I.; Rupprechter, G.; Unterhalt, H.; Freund, H. J., Complex model catalysts under UHV and high pressure conditions: CO adsorption and oxidation on alumina-supported Pd particles. *Journal of Molecular Catalysis A: Chemical* **2000,** *162* (1–2), 51-66; (d) Freund, H. J.; Kuhlenbeck, H.; Libuda, J.; Rupprechter, G.; Bäumer, M.; Hamann, H., Bridging the pressure and materials gaps between catalysis and surface science: clean and modified oxide surfaces. *Topics in Catalysis* **2001,** *15* (2-4), 201-209; (e) Rupprechter, G., Surface vibrational spectroscopy from ultrahigh vacuum to atmospheric pressure: adsorption and reactions on single crystals and nanoparticle model catalysts monitored by sum frequency generation spectroscopy. *Physical Chemistry Chemical Physics* **2001,** *3* (21), 4621-4632; (f) Freund, H., Preparation and characterization of model catalysts: from ultrahigh vacuum to in situ conditions at the atomic dimension. *Journal of Catalysis* **2003,** *216* (1-2), 223-235; (g) Rupprechter, G., A surface science approach to ambient pressure catalytic reactions. *Catalysis Today* **2007,** *126* (1–2), 3-17; (h) Baumer, M.; Libuda, J.; Neyman, K. M.; Rosch, N.; Rupprechter, G.; Freund, H.-J., Adsorption and reaction of methanol on supported palladium catalysts: microscopic-level

studies from ultrahigh vacuum to ambient pressure conditions. *Physical Chemistry Chemical Physics* **2007,** *9* (27), 3541-3558; (i) Rupprechter, G.; Weilach, C., Spectroscopic studies of surface–gas interactions and catalyst restructuring at ambient pressure: mind the gap! *Journal of Physics: Condensed Matter* **2008,** *20* (18), 184019.

2. Rupprechter, G., Sum Frequency Generation and Polarization–Modulation Infrared Reflection Absorption Spectroscopy of Functioning Model Catalysts from Ultrahigh Vacuum to Ambient Pressure. *Advances in Catalysis* **2007,** *51*, 133-263.

3. Diebold, U.; Li, S.-C.; Schmid, M., Oxide surface science. *Annual review of physical chemistry* **2010,** *61*, 129-48.

4. Chen, M. S.; Goodman, D. W., Ultrathin, ordered oxide films on metal surfaces. *Journal of Physics: Condensed Matter* **2008,** *20* (26), 264013.

5. Kuhlenbeck, H.; Shaikhutdinov, S.; Freund, H.-J., Well-ordered transition metal oxide layers in model catalysis--a series of case studies. *Chemical reviews* **2013,** *113* (6), 3986-4034.

6. Jensen, J. A.; Rider, K. B.; Salmeron, M.; Somorjai, G. A., High Pressure Adsorbate Structures Studied by Scanning Tunneling Microscopy: CO on Pt(111) in Equilibrium with the Gas Phase. *Physical Review Letters* **1998,** *80* (6), 1228-1231.

7. (a) Su, X.; Cremer, P. S.; Shen, Y. R.; Somorjai, G. A., High-Pressure CO Oxidation on Pt(111) Monitored with Infrared−Visible Sum Frequency Generation (SFG). *Journal of the American Chemical Society* **1997,** *119* (17), 3994-4000; (b) Somorjai, G. A.; Rupprechter, G., Molecular Studies of Catalytic Reactions on Crystal Surfaces at High Pressures and High Temperatures by Infrared−Visible Sum Frequency Generation (SFG) Surface Vibrational Spectroscopy. *The Journal of Physical Chemistry B* **1999,** *103* (10), 1623-1638.

8. Toyoshima, R.; Yoshida, M.; Monya, Y.; Suzuki, K.; Amemiya, K.; Mase, K.; Mun, B. S.; Kondoh, H., High-Pressure NO-Induced Mixed Phase on Rh(111): Chemically Driven Replacement. *The Journal of Physical Chemistry C* **2015,** *119* (6), 3033-3039.

9. Bernal, S.; Botana, F. J.; Calvino, J. J.; Cifredo, G. A.; Pe´rez-Omil, J. A.; Pintado, J. M., HREM study of the behaviour of a Rh/CeO2 catalyst under high temperature reducing and oxidizing conditions. *Catalysis Today* **1995,** *23* (3), 219-250.

10. Schalow, T.; Brandt, B.; Starr, D. E.; Laurin, M.; Schauermann, S.; Shaikhutdinov, S. K.; Libuda, J.; Freund, H. J., Oxygen-induced Restructuring of a Pd/Fe3O4 Model Catalyst. *Catal Lett* **2006,** *107* (3-4), 189-196.

11. Bare, S. R.; Ressler, T., Characterization of Catalysts in Reactive Atmospheres by X-ray Absorption Spectroscopy. *Advances in Catalysis* **2009,** *52*, 339-465.

12. (a) Salmeron, M.; Schlogl, R., Ambient pressure photoelectron spectroscopy: A new tool for surface science and nanotechnology. *Surface Science Reports* **2008,** *63* (4), 169-199; (b) Kaichev, V. V.; Prosvirin, I. P.; Bukhtiyarov, V. I.; Unterhalt, H.; Rupprechter, G.; Freund, H.-J., High-Pressure Studies of CO Adsorption on Pd(111) by X-ray Photoelectron Spectroscopy and Sum-Frequency Generation. *The Journal of Physical Chemistry B* **2003,** *107* (15), 3522-3527.

13. Tanabe, K.; Yamaguchi, T., Acid-base bifunctional catalysis by ZrO_2 and its mixed oxides. *Catalysis Today* **1994,** *20* (2), 185-197.

14. Lou, J. R.; Hess, U.; Mitchell, K. A. R., The growth of zirconium oxide thin films on Au(111) single-crystal surfaces. *Applied Surface Science* **1992,** *62*, 175-180.

15. Maurice, V.; Salmeron, M.; Somorjai, G. A., The epitaxial growth of zirconium on Pt(111) single crystal surfaces. *Surface Science* **1990,** *237*, 116-126.

16. (a) Antlanger, M.; Mayr-schmölzer, W.; Pavelec, J.; Mittendorfer, F.; Redinger, J.; Varga, P.; Diebold, U.; Schmid, M., $Pt_3Zr(0001)$: A substrate for growing well-ordered

ultrathin zirconia films by oxidation. *Physical Review B* **2012,** (0001), 035451-035451; (b) Li, H.; Choi, J.-I. J.; Mayr-Schmölzer, W.; Weilach, C.; Rameshan, C.; Mittendorfer, F.; Redinger, J.; Schmid, M.; Rupprechter, G., Growth of an Ultrathin Zirconia Film on Pt_3Zr Examined by High-Resolution X-ray Photoelectron Spectroscopy, Temperature-Programmed Desorption, Scanning Tunneling Microscopy, and Density Functional Theory. *The Journal of Physical Chemistry C* **2014,** *119* (5), 2462-2470.

17. Graf, P. O.; de Vlieger, D. J. M.; Mojet, B. L.; Lefferts, L., New insights in reactivity of hydroxyl groups in water gas shift reaction on Pt/ZrO_2. *Journal of Catalysis* **2009,** *262* (2), 181-187.

18. Moreau, F.; Bond, G. C.; Taylor, A. O., Gold on titania catalysts for the oxidation of carbon monoxide: control of pH during preparation with various gold contents. *Journal of Catalysis* **2005,** *231* (1), 105-114.

19. (a) Qian, K.; Fang, J.; Huang, W.; He, B.; Jiang, Z.; Ma, Y.; Wei, S., Understanding the deposition–precipitation process for the preparation of supported Au catalysts. *Journal of Molecular Catalysis A: Chemical* **2010,** *320* (1–2), 97-105; (b) Brown, M. A.; Fujimori, Y.; Ringleb, F.; Shao, X.; Stavale, F.; Nilius, N.; Sterrer, M.; Freund, H.-J., Oxidation of Au by Surface OH: Nucleation and Electronic Structure of Gold on Hydroxylated MgO(001). *Journal of the American Chemical Society* **2011,** *133* (27), 10668-10676.

20. Hugenschmidt, M. B.; Gamble, L.; Campbell, C. T., The interaction of H_2O with a TiO_2(110) surface. *Surface Science* **1994,** *302* (3), 329-340.

21. Shavorskiy, A.; Müller, K.; Newberg, J. T.; Starr, D. E.; Bluhm, H., Hydroxylation of Ultrathin Al2O3/NiAl(110) Films at Environmental Humidity. *The Journal of Physical Chemistry C* **2014**.

22. Pakhare, D.; Schwartz, V.; Abdelsayed, V.; Haynes, D.; Shekhawat, D.; Poston, J.; Spivey, J., Kinetic and mechanistic study of dry (CO2) reforming of methane over Rh-substituted La2Zr2O7 pyrochlores. *Journal of Catalysis* **2014,** *316,* 78-92.

2. Techniques

2.1. X-ray Photoelectron Spectroscopy (XPS)

The photoelectric effect ("the effect of light on the generation of electric sparks") was discovered by H. Hertz in 1887,[1] and the quantum theoretical explanation was later given by A. Einstein in 1905.[2] In 1914, it was shown by Rutherford and coworkers that the kinetic energy of the emitted electron is the difference between X-ray energy and electron binding energy.[3,4] In the 1960s, the precise electron spectrometers developed by Kai Siegbahn in Uppsala led to XPS spectra with high resolution.[5,6] Since then, XPS has become one of the most versatile techniques for studies in surface science.

Figure 2-1 schematically shows a typical lab-based XPS experimental set-up. The X-ray source is usually equipped with a twin anode to provide Mg K_α radiation at 1253.6 eV and Al K_α radiation at 1486.6 eV. Photoelectrons are generated by the interaction between X-rays with energy $h\nu$ (e.g. Mg K_α or Al K_α) and electrons in the atomic shell of atoms in the sample, based on the photoelectric effect. While the generated photoelectrons are travelling towards the surface they experience various scattering processes (those which are inelastically scattered are causing a background). After the photoelectrons reached the surface and have overcome the work function, they are emitted into the vacuum, exhibiting a specific kinetic

energy $E_{kin,S}$. This energy depends on the binding energy E_b of the core electron, the energy of X-ray hv, and the work function of the sample Φ_s. After passing the electron lens system, which is used to yield ultimate transmission and well-defined optical properties, photoelectrons are detected by the electron energy analyzer. Nowadays, hemispherical analyzers are the most frequently used analyzer in XPS. For a fixed potential difference applied to the hemispheres, only photoelectrons with kinetic energies (passing energy) in a certain range can pass through the analyzer. The vacuum level in the analyzer is usually different from the vacuum level of the sample, thus, the kinetic energy $E_{kin,A}$, measured by the analyzer is given by the equation below and is also illustrated in Figure 2-1:

$$E_{kin,A} = hv - E_b - \Phi_S - (\Phi_A - \Phi_s) = hv - E_b - \Phi_A \quad (2\text{-}1)$$

in which Φ_A is the work function of the analyzer of the spectrometer, which is usually calibrated by setting the energy scale to zero at the Fermi edge of reference samples (Au or Ag). After that, the measured $E_{kin,A}$ can be simply related to the E_b characteristic of the sample as follows:

$$E_{kin,A} = hv - E_b \quad (2\text{-}2)$$

It should be noted that the equation above is only valid when the Fermi level is equal for the sample and analyzer, in other words, the sample should be conductive and there has to be an electric connection between the sample and the analyzer. For insulators or in case of charging, an additional shift of the energy scale has to be taken into account due to the ill-defined (or shifted) Fermi level.

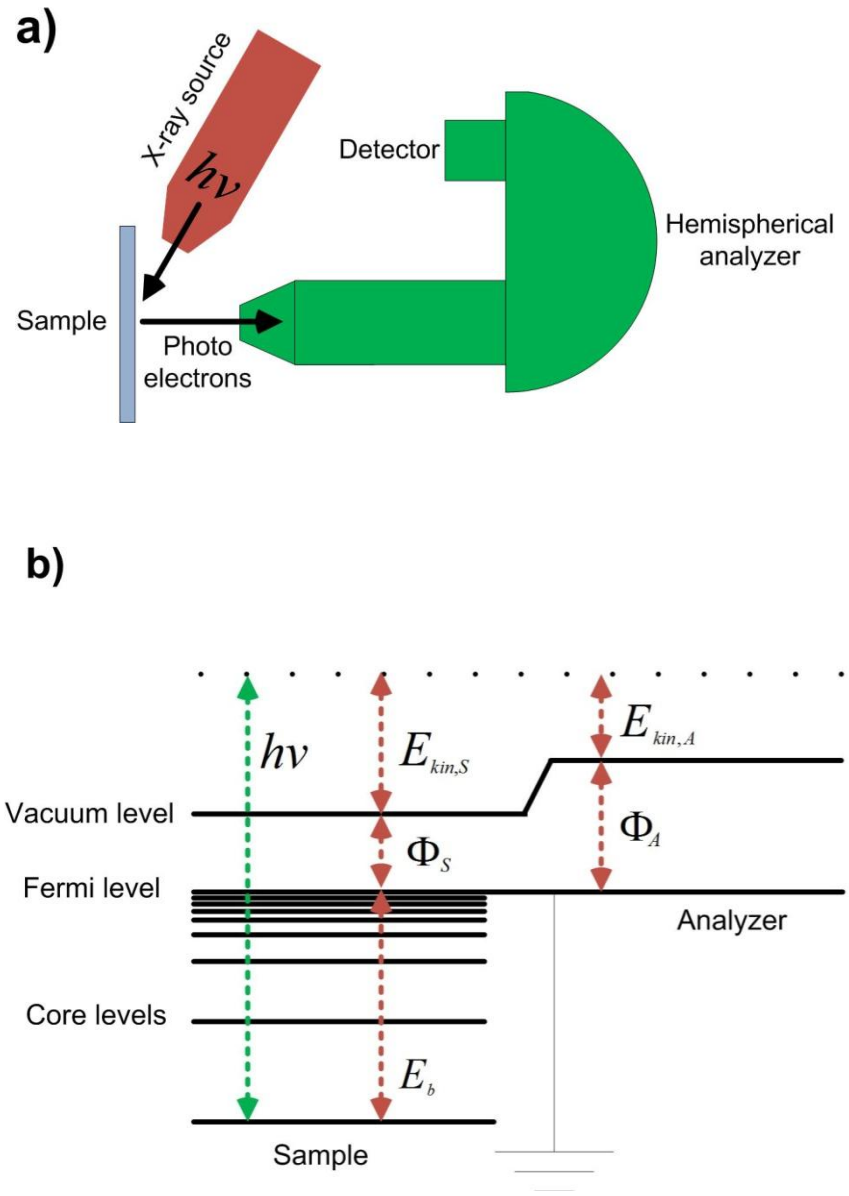

Figure 2-1. Scheme of a) lab-based XPS experimental set-up and b) energy levels in XPS

An XPS spectrum is a plot of intensities of photoelectrons against their binding energy (or kinetic energy). For a simple sample with a homogeneous concentration, the intensity can be expressed as:

$$I = F_X(h\nu)S(E_{kin})\sigma(E_{kin})n\lambda(E_{kin})cos\theta \qquad (2\text{-}3)$$

in which I is the intensity of the XPS peak, F_X is the incident X-ray flux on the sample at a certain energy $h\nu$, $S(E_{kin})$ is the analyzer efficiency for detecting the electron at certain

kinetic energy (also called transmission function), $\sigma(E_{kin})$ is the photoelectron cross-section, n is the concentration of the atoms, $\lambda(E_{kin})$ is the mean free path of the photoelectrons and will be discussed later in more detail, θ is the so called take-off angle, which is the angle between the surface normal and the ejection of the photoelectrons towards the analyzer (larger θ leads to higher surface sensitivity).

In addition to the photoelectron peaks, Auger electron peaks can be detected in a photoelectron spectrum originating from the Auger process, which is due to the relaxation of the excited ions remaining after photoemission. In this process an electron from a higher energy level fills the hole resulting from the emission of the photoelectron and the difference in energy between these two levels is compensated either by X-ray fluorescence (a minor process in this energy range which competes with the Auger process) or transferred to the Auger electron. Besides, satellite peaks can also occur in the spectrum due to a non-monochromatized X-ray source, plasmon loss and shake-up or shake-off effect. Plasmon excitation loss peaks are caused by discrete losses due to collective electron oscillations in the valence band, and are typically on the order of 10-20 eV.[7] The shake-up/shake-off induced satellites are due to a sudden change in coulombic potential as the photoelectron passes through the valence band.

The line width of an XPS peak is determined by the lifetime of the core hole state left after photoemission, the instrument (due to both X-ray source and analyzer) and temperature induced broadening. Therefore, the line shape is represented by a combination of both Lorentzian and Gaussian functions. For metals such a symmetric line shape is usually replaced by an asymmetric shape with a tail to higher binding energy, which is caused by many-body interactions of the photoelectron with free electrons at the Fermi edge, as shown by Doniach and Sunjic.[8]

X-rays penetrate several micrometers into the sample, the photoelectrons, however, interact strongly with matter and can thus only travel short distance before they lose too much energy before escaping to the vacuum. The average distance electrons can travel, before loosing energy due to collision, is called the inelastic mean free path λ, which is typically a few Å for electrons in solids, depending on their kinetic energy. Given that almost all photoelectrons used in XPS have kinetic energies in the range of 0.2-1.5 keV, λ is restricted to less than 1-2 nm. Thus, the probing depth of XPS (usually taken as 3 λ) is around 1.5-6 nm, and this makes XPS a powerful tool to probe the surface of a sample.[9]

2.1.1. In situ (Near Ambient Pressure) NAP-XPS at elevated pressure

As described in Chapter 1, it is of vital importance to perform surface science studies both under UHV and high pressure, in order to bridge the pressure gap. However, typical lab-based XPS operates under high vacuum conditions, due to both instruments requirements (X-ray source, hemispherical analyzer and detector) and scattering of photoelectrons by gas molecules.[10,11] The signal attenuation of photoelectrons at pressure P can be estimated as follows:

$$I = I_0 e^{-(\sigma d P)} \qquad (2\text{-}4)$$

in which I is the signal at pressure P, I_0 is the signal at high vacuum, d is the distance that the photoelectrons travel through the gas at pressure P, and σ is the cross section of scattering. Considering that σ is a characteristic of a certain experiment, one needs to decrease d in order to reduce the loss of the signal I when performing high pressure experiments. To this end, several differential pumping stages between the sample surface and photoelectron detection are usually employed. In this thesis, in-situ NAP-XPS measurements were performed in two systems, one located at beamline I511 at the Max Lab II electron storage ring (Lund)[10] and the

other at the Boreskov Institute of Catalysis (Novosibirisk).[12,13] The former is synchrotron-based whereas the latter is lab-based, and they will be briefly described below.

The synchrotron-based in situ XPS system is schematically shown in Figure 2-2. The photons are generated by an undulator-based soft X-ray beamline. The beam is monochromated by a monochromator and refocused by a set of optics. The high pressure cell (with gas inlet and outlet) is essentially a small cell located inside the analysis chamber. It is mounted onto a manipulator and can be attached to the pre-lens of the analyzer (SPECS PHOIBOS 150 NAP). Three differential pumping stages are inserted between the sample and the entrance slit of the hemispherical analyzer, and the fourth pumping stage is directly at the analyzer and detector.

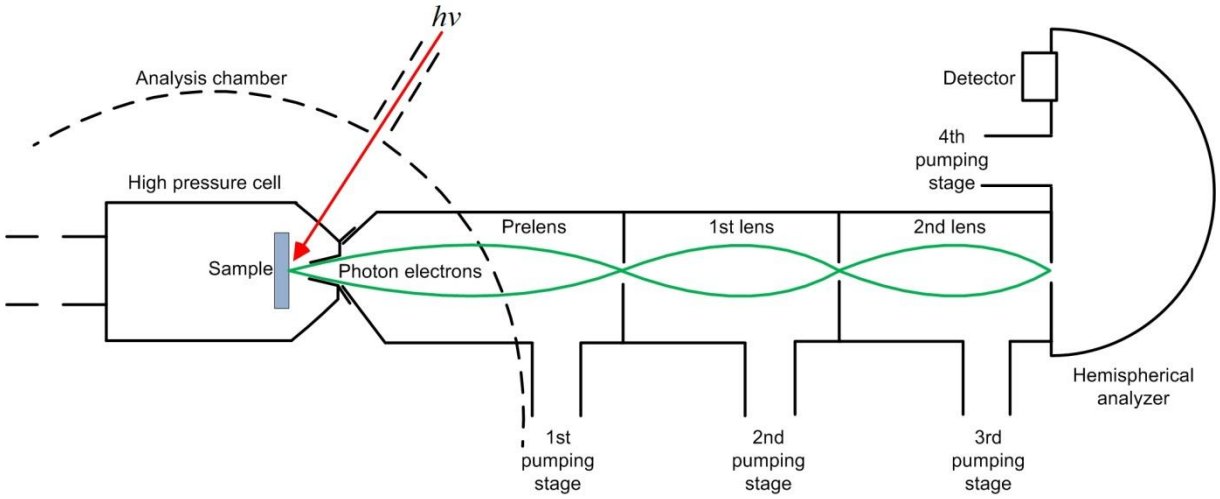

Figure 2-2. Schematic sketch of the synchrotron-based in situ XPS system in Lund (side view)

The lab-based in situ XPS is illustrated in Figure 2-3. The high pressure cell is inserted to the analyzer chamber of the XPS through the preparation chamber on the left hand side, and the pressure inside the high pressure cell is measured with a Baratron gauge.[13a] The high pressure cell has an entrance for X-rays and an exit for the photoelectrons. The analyzer chamber is pumped by a diffusion pump, and the X-ray gun and the hemispherical analyzer are pumped by two separated diffusion pumps.

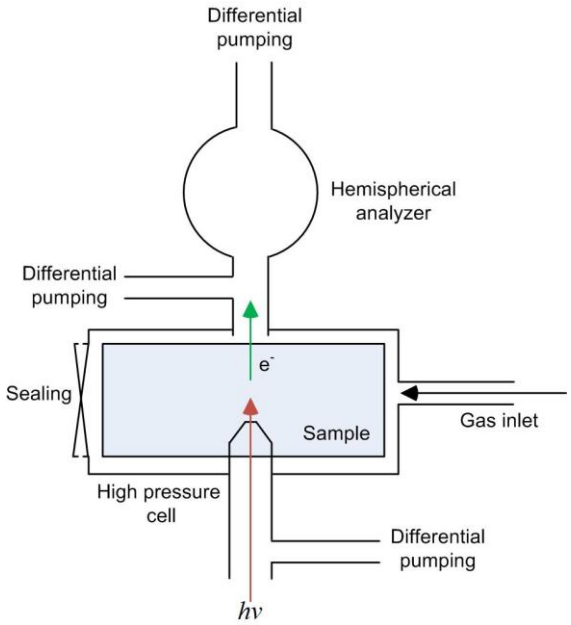

Figure 2-3. Schematic view of the lab-based in situ XPS system in Novosibirisk (top view)

2.2. Infrared Spectroscopy

2.2.1. Theory of molecular vibrations

Being one of the first spectroscopic techniques that has found general acceptance in catalysis research, infrared (IR) spectroscopy is mainly applied to detect adsorbed species on surfaces of catalysts. Most molecular vibrations are excited with mid-IR radiation, which is in the range from 200-4000cm^{-1} (corresponding to 50-2.5 μm in wavelength, and 25-496 meV in energy).

IR spectroscopy involves the transition between both vibrational and rotational energy levels of molecules. Because the main interests of this thesis are adsorbed molecules, the transition between rotational energy levels which is responsible for the gas phase signal will not be decribed further. For vibrational motions of molecules, the harmonic oscillator potential

represents a simple model. When atoms of molecules slightly deviate from their equilibrium positions, the potential energy $V(r)$ can be described as follows:

$$V(r) = \frac{1}{2}k(r - r_{eq})^2 \qquad (2\text{-}5)$$

in which, k is the force constant of the vibrating bond, r is the distance between the vibrating atoms, and r_{eq} is the equilibrium distance between the atoms. Because the harmonic oscillator potential is a parabola, the corresponding vibrational energy levels are equidistant. Solving the Schrödinger equation for the harmonic oscillator potential in the energy levels results in:

$$E_n = \left(n + \frac{1}{2}\right)hv \qquad (2\text{-}6)$$

in which E_n is the energy of the nth vibrational level, n is the vibration quantum number, h is the Planck´s constant, and v is the frequency of the vibration. Defining the reduced mass of the diatomic molecule μ as $\frac{m_1 m_2}{m_1+m_2}$, the frequency of the vibration v can be determined by:

$$v = \frac{1}{2\pi}\sqrt{\frac{k}{\mu}} \qquad (2\text{-}7)$$

Thus, it is clear that v increases with increasing bond strength and it decreases for molecules with heavier atoms. In order to allow a transition within vibrational energy levels to occur, selection rules have to be fulfilled. A general selection rule is that the dipole moment of the molecule must change in the course of vibration. It should be noted that this general selection rule does not require a molecule to possess a permanent dipole moment. Instead, the transition can also occur if a state without a dipole moment changes to a state with one (dynamic dipole moment). A specific selection rule in the harmonic approximation is that the vibrational quantum number can only change by one unit, namely, $\Delta n = \pm 1$. Except at very high temperature, vibrational ground state ($v = 0$) is the only state populated. Therefore, a vibrational spectrum usually only shows one line corresponding to the transition from $v = 0$ to $v = 1$. Overtone vibrations, namely, vibrational transitions with $\Delta n > 1$ are not included in

this model. Another limitation of the harmonic approximation is that it is only valid for small deviations of the atoms from their equilibrium positions, meaning that it does not permit the breaking of bonds between two atoms even at high vibrational excitations. In this regards, the Morse potential is a more realistic model for the potential energy $V(r)$:

$$V(r) = D(1 - e^{-a(r-r_{eq})})^2 - D \qquad (2\text{-}8)$$

in which, D is the dissociation energy of the vibrating bond, and a is the parameter which controls the steepness of the potential well, which is related to force constant k and dissociation energy D. In this model, the energy levels are no longer equidistant and they converge when approaching the dissociation limit. Another advantage of the Morse potential model is that overtones become allowed. Nevertheless, the harmonic oscillator description usually suffices when interpreting IR spectra.

A molecule consisting of N atoms has $3N$ degrees of freedom. For nonlinear molecules, $3N - 6$ normal vibrational modes should be observed, whereas for linear molecules, $3N - 5$ normal modes should be observed. Molecular vibrations can be grouped into stretching and bending modes. Stretching vibration mode is defined as the continuous change in the interatomic distance along the axis of the bond. Bending vibration mode is defined as the change in the angle occurring between two bonds. Four bending vibrations exist namely, wagging, twisting, rocking and scissoring.

2.2.2. Fourier-Transform Infrared (FTIR) Spectroscopy

Comparing to traditional dispersive spectrometers, FTIR has the advantage that all frequency components are detected simultaneously, thus the acquisition time to record a spectrum with good resolution and high signal-to-noise ratio (S/N) is less.[14] The key element in an FTIR spectrometer is an optical device called interferometer, which measures the interference signal between two light beams. Nowadays, the Michelson interferometer is the most common type

of interferometer. Figure 2-4 shows the optical design of a Michelson interferometer schematically. The Infrared source emits an IR beam, which is collected by the collimating mirror and is parallelized. Then, the collimated IR beam is reflected to the beamsplitter. One part of the beam is transmitted, and travels towards the fixed mirror, and the rest of the beam is reflected and travels towards the moving mirror. Both of the transmitted and reflected beam are reflected by the corresponding mirrors (fixed mirror and moving mirror) and travel back to the beamsplitter with a path difference δ. Depending on the wavelength of the IR light and δ, the reflected beams interfere constructively (in-phase) or destructively (out of phase). The recombined beam then leaves the interferometer, interacts with the sample and reaches the detector. The intensity of the beam is measured as a function of δ to generate a so called interferogram. When δ equals to zero (no path difference), the measured intensity is at maximum because all wavelengths of the IR beam are in-phase and constructive interference occurs. As δ changes, the intensity of the interferogram decreases quickly due to partially or totally destructive interference. The function of the interferometer is the optical transformation of the spectrum of the IR beam into the interferogram. This interferogram is measured by the IR detector and converted into a spectrum by Fourier transformation. Thus, each single scan of the interferometer can generate the entire spectrum. The signal to noise ratio increases with the number of scans.

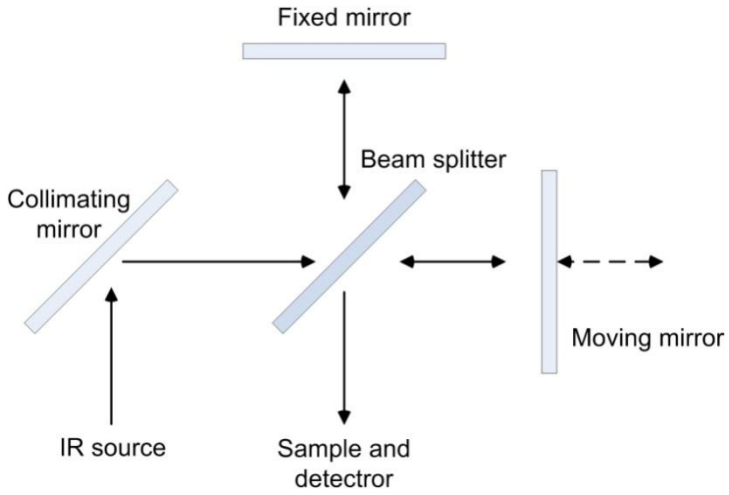

Figure 2-4. Scheme of the optical design of a Michelson interferometer.

2.2.3. Infrared Reflection-Absorption Spectroscopy (IRAS)

IRAS is used to measure the vibrations of gases adsorbed on planar surfaces, which are non transparent to the IR light.[15] The IR beam hits the surface at a grazing angle and is reflected from a highly reflective surface towards the detector. The detector measures the reflection loss due to the excitation of the adsorbed molecules and generates a reflection absorption spectrum. One important feature of this type of operation is that the so-called metal surface selection rule has to apply if the sample is metallic or an oxide thin film grown on a metallic substrate.[16,17] It has been shown for IRAS that for such surfaces only vibrations with a dipole moment (or component thereof) *perpendicular* to the surface will be excited by the p-polarized component. In order to explain the metal surface selection rule, one needs to understand the phase shift of different electric field components upon reflection at the surface.

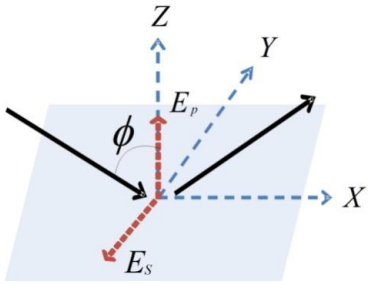

Figure 2-5. Polarization planes and angle of incidence.

In Figure 2-5, the incident IR beam strikes the surface at an angle of ∅, and ∅ is defined as the angle between the incident IR beam and the surface normal. The incidence and reflection of the radiation and the surface normal lie in the same plane, which is called the plane of incidence and is perpendicular to the surface. A wave with a polarization vector parallel to this plane is called p-polarized ("parallel"), and a wave with a polarization vector perpendicular to this plane is called s-polarized ("senkrecht"). Their corresponding electric field is denoted as E_P and E_S. In Figure 2-6, it is shown that the s-polarized component undergoes phase shift of 180° for all ∅ at the surface. Because the reflection coefficient of metals is close to unity within the IR frequency range, the electric field vanishes at the surface due to destructive interference. In fact, one of the reasons for the metal surface selection rule is that the required s-polarized electric field component E_S for the excitation of vibrations parallel to the surface is zero on the surface. The phase shift of p-polarized component is strongly dependent on ∅. When ∅ approaches 90°, its phase shifts increases and finally reaches 180°. Thus, at grazing angle, a large value of E_P occurs due to constructive interference.

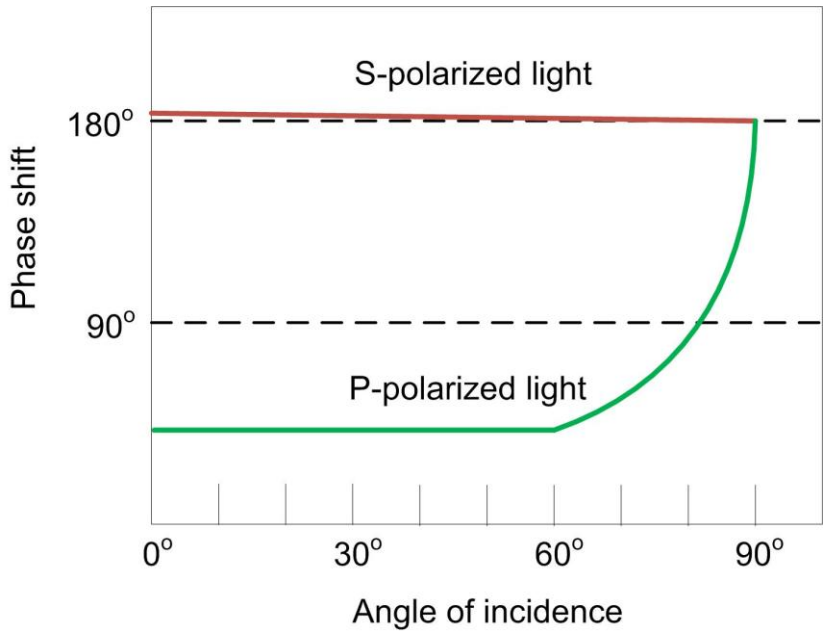

Figure 2-6. Phases shift as a function of incidence angle.

With an assumption that the intensity of adsorption depends on the square of E_P and the number of adsorbed molecules, a function as $E^2 sec\emptyset$ can be derived.[18] As shown in Figure 2-7, a sharp maximum of the surface intensity appears at high angle of incidence (grazing incidence).

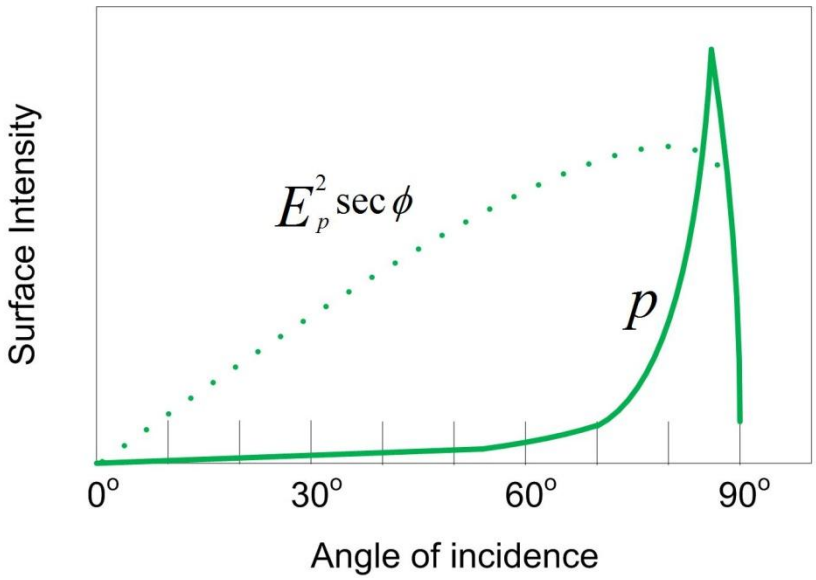

Figure 2-7. Surface Electric field (dotted line) and intensity of p-polarized light (solid line) as a function of incident angle.

Another reason for the validity of the metal surface selection rule is the interaction between the molecules´ dipole moment and its image dipole below the surface. The latter is formed by the electrons of the metallic substrate, as shown in Figure 2-8. The dipole moments of the molecule and its image charges perpendicular to the surface reinforce each other, and the vibrations perpendicular to the surface are even enhanced due to the amplified p-polarized electric filed component E_p at grazing incidence. In contrast, the dipole moments of molecules and the image charges parallel to the surface cancel as they are oriented opposite of each other and the vibration is inactive for IRAS.

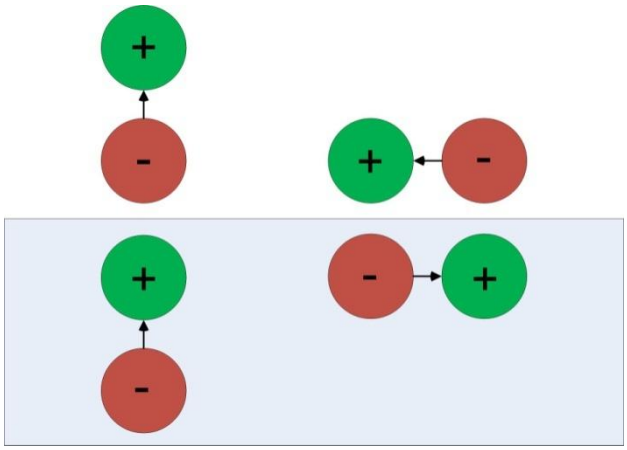

Figure 2-8. Dipole moments and its image dipole

2.3. Low Energy Electron Diffraction (LEED)

A well-defined surface structure is a major advantage of model systems over technical-grade materials. LEED is an excellent technique to study the long range structural order of a surface. The energy of the electrons used in LEED is typically ranges from 30 to 200 eV, and the de Broglie wavelength of an electron is approximated by

$$\lambda[\text{Å}] = \sqrt{\frac{150}{E(eV)}} \qquad (2\text{-}9)$$

Thus, the wavelength of these electrons is in the range of 0.8-2.2 Å, which is comparable with the atomic spacing and the atomic diffraction condition is satisfied. In addition, the low energy electrons possess very short mean free path, so most elastic collisions only occur in the very top layers of a sample. The diffraction pattern is governed only by the 2-dimensional surface periodicity, which makes LEED a powerful tool for surface analysis.[19,20]

Figure 2-9 shows a typical experimental set up for LEED.

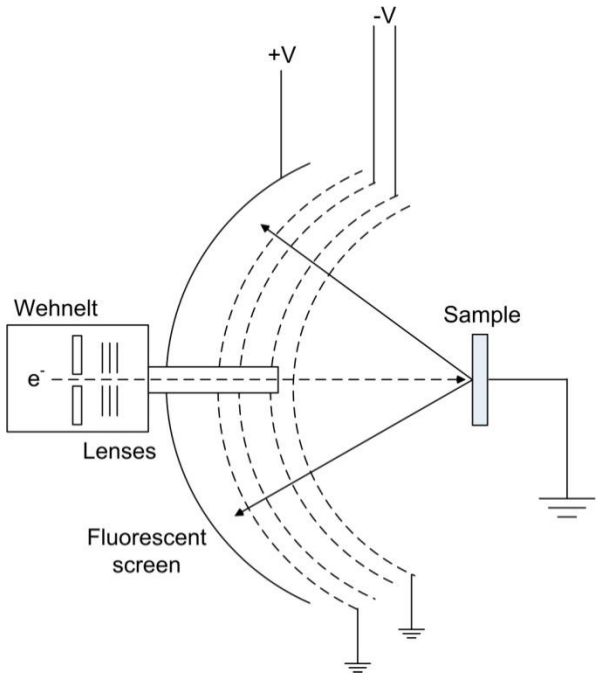

Figure 2-9. Scheme of a typical experimental set up for LEED

A collimated beam of low energy electrons is produced by an electron gun, its size and focus are controlled by a Wehnelt cylinder and electrostatic lenses, respectively. The beam then hits the sample, which is at earth potential in order to prevent charging. It should be noted that the last aperture of the electrostatic lenses and the first grid are also grounded to allow the linear beam trajectories. The second and third grids are at a potential of several volts below the incoming electron beam, thus the inelastically scattered electrons are rejected. The fourth grid is again grounded so that the other grids are not influenced by the fluorescent screen. The screen is biased to a high voltage (3-6 KV) to collect the diffracted and elastically scattered electrons and generate the diffraction pattern.

Electron diffraction can be observed in a simple form by scattering from two atoms separated by a distance d. In a LEED experiment, the electron beam is directed along the surface normal of the sample, as shown in Figure 2-10. Depending on the path difference ($dsin\theta$), the wave

scattered from the two centers will constructively or destructively interfere. Constructive interference occurs, when

$$dsin\theta = n\lambda = n\frac{2\pi}{k}, sin\theta = n\frac{2\pi}{dk} \quad (2\text{-}9)$$

in which, k is the wave vector.

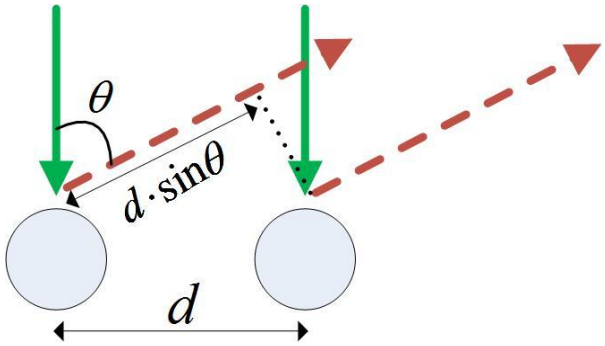

Figure 2-10. Simple scheme of electrons diffractions on 2D surface.

Usually one uses the Ewald construction to represent the diffraction. In fact, the fluorescent screen can be seen as the surface of an Ewald sphere, which intersect with the reciprocal lattice rods and the generated diffraction beam.[19] The simple construction of the reciprocal lattice in 2-dimentions is described as follows. a_1 and a_2 are the base vectors of a surface lattice, then the reciprocal lattice is defined by reciprocal lattice vectors a_1^* and a_2^*.

$a_1 \cdot a_2^* = a_2 \cdot a_1^* = 0$, implies a_1 is perpendicular to a_2^*

$a_1 \cdot a_1^* = a_2 \cdot a_2^* = 1$, implies the inverse relations between $a_1$and a_1^*, $a_2$and a_2^*

A hexagonal lattice in real space and the corresponding LEED pattern in reciprocal space are shown schematically in a) and b) of Figure 2-11. In the case that a superstructure is formed at the surface, e.g. adsorbate molecules with periodical structures, new spots can be detected in the LEED pattern, as shown in c) and d) of Figure 2-11. However, one cannot determine the exact position of the adsorbate molecules with respect to the substrate, since LEED only reflects the surface periodicity. In order to obtain information about the 3-dimensional atomic

positions, one can measure the spot intensity (I) as a function of the primary electron energy (V). However, analysis of such I-V curve is not straightforward, as the dynamic theory has to be considered due to the multiple scattering events.

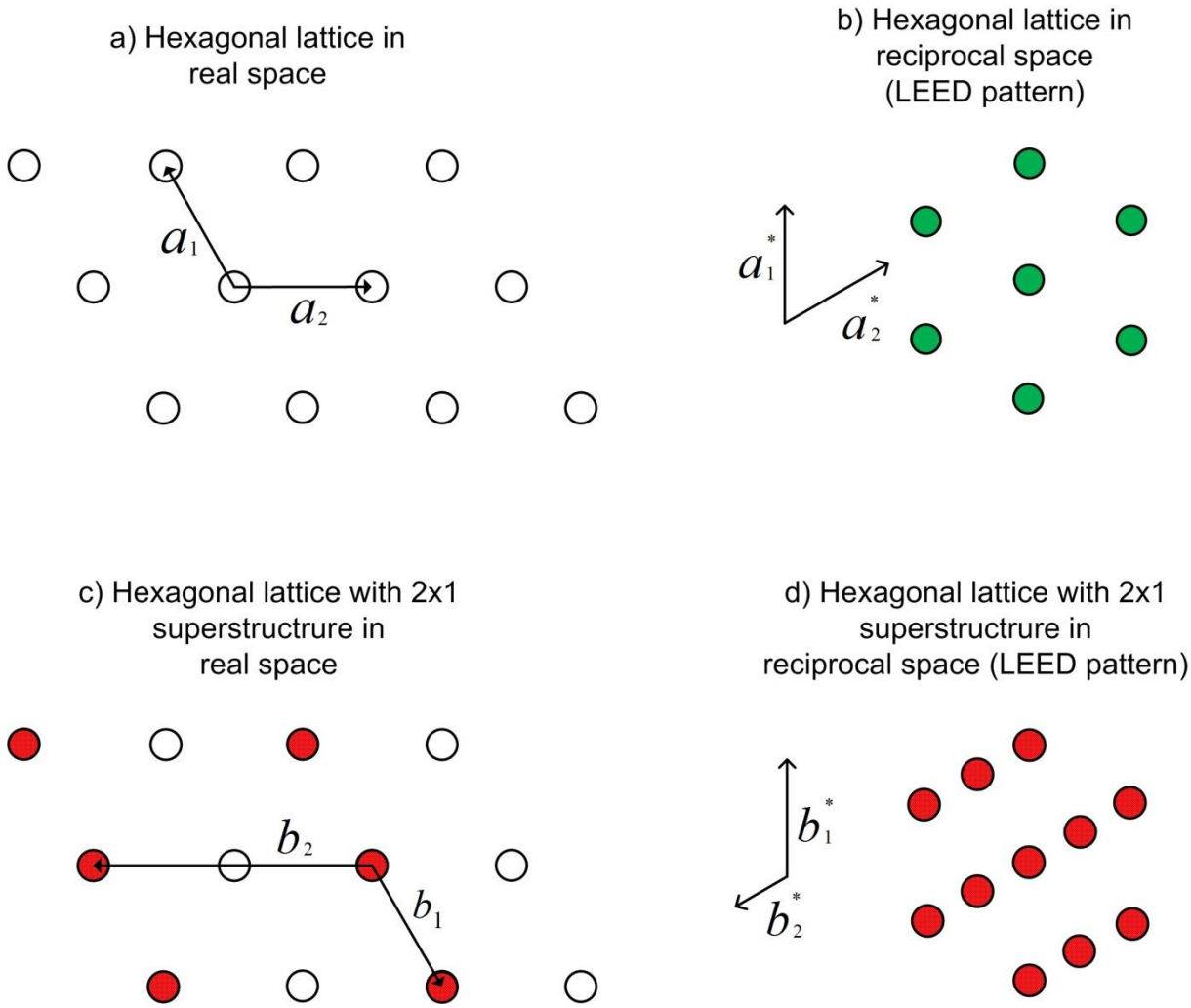

Figure 2-11. Schematic example of a) a hexagonal lattice in real space, b) its corresponding LEED pattern, c) same lattice with a 2×1 superlatice in real space and d) the corresponding LEED pattern of c).

2.4. Temperature programmed desorption (TPD)

TPD is a conceptually straightforward technique to study the desorption of molecules which were prior adsorbed on the surface of single crystals or nanostructured surfaces (but also powders), as illustrated in Figure 2-12.

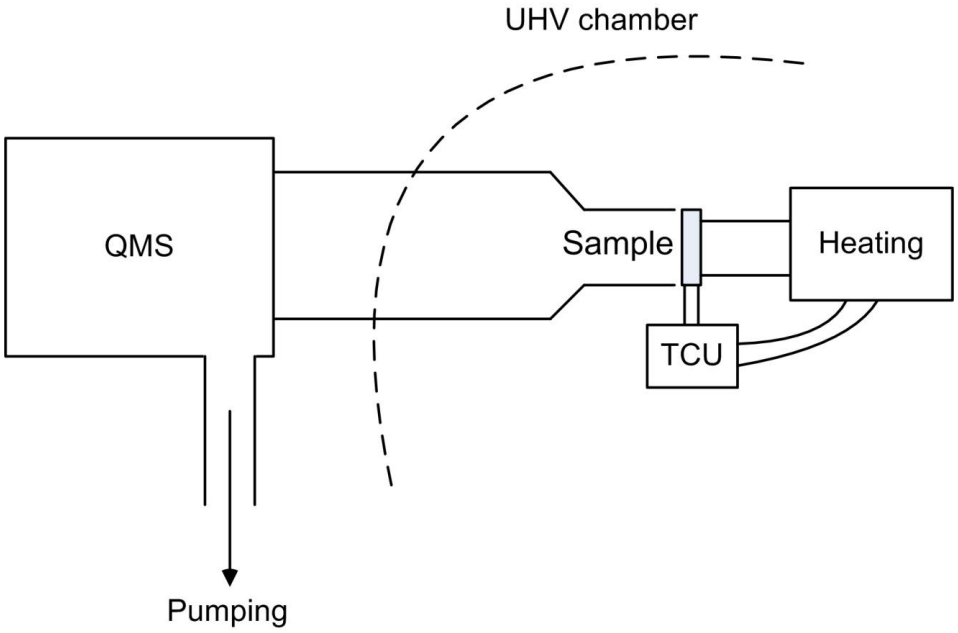

Figure 2-12. A schematic view of a TPD setup

For a TPD experiment a (clean) sample surface is first exposed to a gas, and then, after evacuation, heated up at a constant heating rate. Simultaneously, a Quadrupole Mass spectrometer (QMS) is employed to detect the molecules desorbing from the surface. A stable heating with a linear heating ramp is facilitated by using a temperature control unit (TCU), which measures the sample temperature and then tunes the heating power accordingly. In order to minimize signals coming from the sample holder and residual gases from the UHV system, the QMS is mechanically shielded by a nozzle pointing towards the sample. In order to prevent the readsorption of the desorbed species and to provide a sufficient gas flow

towards the QMS, the nozzle that is pointing towards the sample and the QMS are both differentially pumped.

The QMS is the key element of the TPD technique. The electrically heated cathode emits electrons, which are accelerated by the voltage applied between anode and cathode. Gas molecules are ionized through electron bombardment, forming single (AB^+) and multiple positive ions (AB^{2+}), as well as fractal ions ($A^+ + B^+$). The formed ions are then focused into the mass filter, consisting of four parallel rods arranged in the form of a square. Both, time independent DC potential and time dependent AC potential are applied to the rods, which influence the trajectory of ions traveling through the four rods. For an ion with given mass-to-charge ratio, it will only pass through the quadrupole filter at a certain potential. At other potentials, it will change the original path and will be neutralized on the rods. After passing through the quadrupole the ions finally enter the detector, which monitors the ions as the potential on the rods are altered. Two detector types are available: a) faraday cup, which directly measures the ion current using an electrometer amplifier; b) a secondary electron multiplier (SEM), which measures the multiple secondary electrons generated by the collision between the ion and the dynodes.

The Polanyi-Wigner equation can be used to describe the desorption rate, assuming that the adsorbate (atoms or molecules) occupies identical sites without interacting with each other:

$$r_{des} = -\frac{d\theta}{dt} = k_n\theta^n = k_n^0\theta^n \exp\left(-\frac{\mathrm{E_{des}}}{\mathrm{k_B T}}\right) \qquad (2\text{-}10)$$

in which, E_{des} is the activation energy of desorption, n is the order of the adsorption kinetics, θ is the occupied sites and k_n is the desorption rate constant. During the TPD process, the exponential term increases rapidly and the adsorbate coverage decrease, resulting in a desorption peak maximum at T_m. By using the Redhead equation,[21] E_{des} can be approximated by:

$$E_{des} = k_B T_m (l_n \frac{\nu T_m}{\beta} - 3.64) \quad (2\text{-}11)$$

in which, ν is the attempt frequency, that is roughly on the order of the atomic frequency of the crystal (~$10^{13} s^{-1}$) and β is the heating rate. The Redhead equation can only be applied when dealing with first-order desorption and assuming E_{des} and ν to be coverage independent.

2.5. Vienna Set-up

The UHV system in Vienna is the main set-up used in this thesis, all LEED, TPD, IRAS and lab-based ex situ XPS measurements were performed with this machine. Being originally designed and built by Prof. Rupprechter at the Fritz Haber Institute of the Max Planck Society in Berlin,[22,23,24,15] the chamber was upgraded several times and also moved to the Institute of Materials Chemistry at TU Wien in 2006. Specifically, this UHV system consists of two chambers: a) a UHV preparation chamber (upper part) used for sample preparation and characterization, and b) a UHV-high pressure cell (lower part) with an optimized geometry for IRAS experiments.

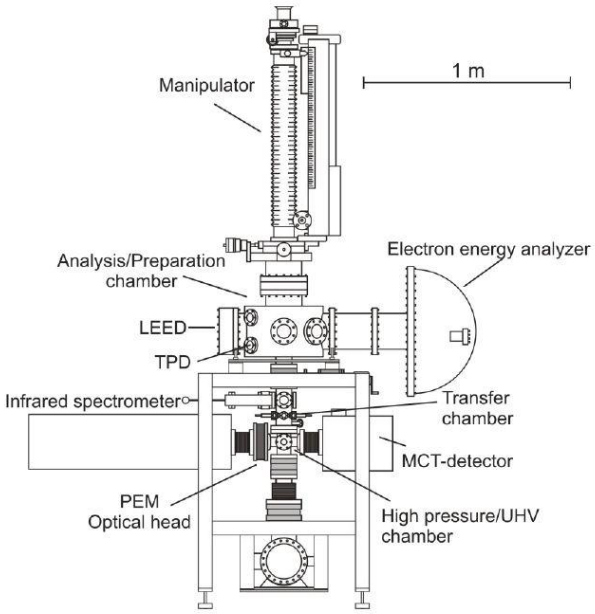

Figure 2-13. A schematic drawing of Vienna Setup (copied from PhD thesis of Dr. Christian Weilach, (2009), which is a copy from[15]

A schematic drawing of the Vienna Setup is shown in Figure 2-13. The preparation chamber is evacuated by a turbomolecular pump backed by a roughing pump, ensuring a base pressure of 5×10^{-10} mbar. The chamber is equipped with a sputter gun, a 4-grid LEED optics, XPS and TPD. The XPS system consists of a non-monochromatic Al/Mg dual anode X-ray gun (SPECS XR50), a hemispherical electron energy analyzer (SPECS PHOIBOS 150) and a 9-channel CEM detector. The TPD system consists of a nozzle (1 cm in diameter) which is connected to a QMS (MKS eVision+), that is differentially pumped by another turbo molecular pump. Different gases with high purity can be dosed to the chamber via two high precision leak valves. As shown in Figure 2-13, a PEM optical head is positioned in between the Infrared Spectrometer and the reaction cell. Such configuration is used to perform Polarization Modulation-Infrared Reflection Absorption Spectroscopy (PM-IRAS), which is dedicated to measure IRAS spectrum in-situ up to ambient pressure. In this thesis, however,

mostly IRAS was employed. For PM-IRAS spectra of CO (up to 100 mbar) adsorbed on Ni nanoparticles on zirconia trilayer the reader are refereed to the master thesis of MSc. Kresimir Anic (2013 TU Wien).

The sample (a $Pt_3Zr(0001)$ single crystal) is fixed via a Tantalum-wire grid, which is spot welded onto two Molybdenum rods. A K-type thermocouple (NiCr/Ni) is spot welded to the backside of the sample and connected to a Eurotherm 3216 PID controller for temperature reading. The two molybdenum rods and the thermocouple were fixed to a cold finger through a UHV suitable feedthrough, and the cold finger is connected to a VG Omniax MX manipulator (x,y,z, 360° rotation). The sample can be resistively heated up to 1300 K and cooled down to about 80 K by filling in liquid nitrogen to the cold finger.

For IRAS measurements, the sample is transferred to the UHV-high pressure chamber. During the transferring process, the manipulator enters differentially pumped spring loaded Teflon seals, which separate the UHV-high pressure cell from the UHV chamber. The IRAS system includes a Bruker IFS 66v spectrometer, and a liquid Nitrogen cooled Mercury Cadmium Telluride detector. The spectrometer, the detector compartment and the metal bellows connecting the detector compartment and the chamber are evacuated, and the bellow connecting the spectrometer and the chamber is purged with nitrogen. In addition, the BaF_2 windows are recessed inside the chamber to shorten the path of the IR beam in the gas atmosphere. Therefore, the gas phase contribution to the IR spectrum along the beam pathway is greatly minimized.

In addition, two other UHV-machines were employed in this thesis. The synchrotron-based XPS system located at beamline I511 at the Max Lab II electron storage ring[10] was used to study the electronic structure of the ultra-thin ZrO_2 film, as well as the interaction between the film and water. A lab-based XPS system located at the Boreskov Institute of Catalysis[13a,13b]

was used to study the interaction between the film and CO_2 (and water). More details of these two machines will be mentioned in the experimental part of the following chapters.

High purity gases were used throughout the thesis: 5.0 (99.999%) for oxygen (O_2), argon (Ar) and nitrogen (N_2), 4.7 (99.997%) for carbon monoxide (CO) and 4.5 (99.995%) for carbon dioxide (CO_2). In addition, CO was further purified by passing it over a carbonyl absorber cartridge and a cold trap (mixture of ethanol and liquid nitrogen at around 180 K). Water and heavy water were purified by conducting multiple freeze-pump-thaw cycles.

Bibiliography

1. Hertz, H., Ueber einen Einfluss des ultravioletten Lichtes auf die electrische Entladung. *Annalen der Physik* **1887,** *267* (8), 983-1000.

2. Einstein, A., Über einen die Erzeugung und Verwandlung des Lichtes betreffenden heuristischen Gesichtspunkt. *Annalen der Physik* **1905,** *322* (6), 132-148.

3. Rutherford, E., XXXVII. The connexion between the β and γ ray spectra. *Philosophical Magazine Series 6* **1914,** *28* (165), 305-319.

4. Rutherford, E.; Robinson, H.; Rawlinson, W. F., XXXIV. Spectrum of the β rays excited by γ rays. *Philosophical Magazine Series 6* **1914,** *28* (164), 281-286.

5. Hagström, S.; Nordling, C.; Siegbahn, K., Electron spectroscopy for chemical analyses. *Physics Letters* **1964,** *9* (3), 235-236.

6. Fahlman, A.; Hamrin, K.; Hedman, J.; Nordberg, R.; Nordling, C.; Siegbahn, K., Electron Spectroscopy and Chemical Binding. *Nature* **1966,** *210* (5031), 4-8.

7. Hofmann, S., *Auger- and X-Ray Photoelectron Spectroscopy in Materials Science: A User-Oriented Guide*. Springer Berlin Heidelberg: 2012.

8. Doniach, S.; Sunjic, M., Many-electron singularity in X-ray photoemission and X-ray line spectra from metals. *Journal of Physics C: Solid State Physics* **1970,** *3* (2), 285.

9. Niemantsverdriet, J. W., *Spectroscopy in Catalysis: An Introduction*. Wiley: 2000.

10. Schnadt, J.; Knudsen, J.; Andersen, J. N.; Siegbahn, H.; Pietzsch, A.; Hennies, F.; Johansson, N.; Mårtensson, N.; Öhrwall, G.; Bahr, S.; Mähl, S.; Schaff, O., The new ambient-pressure X-ray photoelectron spectroscopy instrument at MAX-lab. *Journal of synchrotron radiation* **2012,** *19* (Pt 5), 701-704.

11. Starr, D. E.; Liu, Z.; Havecker, M.; Knop-Gericke, A.; Bluhm, H., Investigation of solid/vapor interfaces using ambient pressure X-ray photoelectron spectroscopy. *Chemical Society Reviews* **2013,** *42* (13), 5833-5857.

12. Joyner, R. W.; Roberts, M. W.; Yates, K., A "high-pressure" electron spectrometer for surface studies. *Surface Science* **1979,** *87* (2), 501-509.

13. (a) Bukhtiyarov, V. I.; Kaichev, V. V.; Prosvirin, I. P., X-ray photoelectron spectroscopy as a tool for in-situ study of the mechanisms of heterogeneous catalytic reactions. *Topics in Catalysis* **2005,** *32* (1-2), 3-15; (b) Kaichev, V. V.; Prosvirin, I. P.; Bukhtiyarov, V. I.; Unterhalt, H.; Rupprechter, G.; Freund, H.-J., High-Pressure Studies of CO Adsorption on Pd(111) by X-ray Photoelectron Spectroscopy and Sum-Frequency Generation. *The Journal of Physical Chemistry B* **2003,** *107* (15), 3522-3527; (c) Rupprechter, G.; Kaichev, V. V.; Unterhalt, H.; Morkel, M.; Bukhtiyarov, V. I., CO dissociation and CO hydrogenation on smooth and ion-bombarded Pd(111): SFG and XPS spectroscopy at mbar pressures. *Applied Surface Science* **2004,** *235* (1–2), 26-31.

14. Smith, B. C., *Fundamentals of Fourier Transform Infrared Spectroscopy*. Taylor & Francis: 1995.

15. Rupprechter, G., Sum Frequency Generation and Polarization–Modulation Infrared Reflection Absorption Spectroscopy of Functioning Model Catalysts from Ultrahigh Vacuum to Ambient Pressure. *Advances in Catalysis* **2007,** *51*, 133-263.

16. Greenler, R. G., Infrared Study of Adsorbed Molecules on Metal Surfaces by Reflection Techniques. *The Journal of Chemical Physics* **1966,** *44* (1), 310-310.

17. Hoffmann, F. M., INFRARED REFLECTION-ABSORPTION ADSORBED MOLECULES SPECTROSCOPY. *Surface Science Reports* **1983,** *3*, 107-192.

18. Hollins, P., The influence of surface defects on the infrared spectra of adsorbed species. *Surface Science Reports* **1992,** *16* (2), 51-94.

19. Hudson, J. B., *Surface Science: An Introduction*. Wiley: 1998.

20. Somorjai, G. A.; Rupprechter, G., The Flexible Surface: Molecular Studies Explain the Extraordinary Diversity of Surface Chemical Properties. *Journal of Chemical Education* **1998,** *75* (2), 161.

21. P.A.Redhead, Thermal Desorption of Gases. *VACUUM* **1962,** *12* (4), 203-211.

22. Rupprechter, G.; Dellwig, T.; Unterhalt, H.; Freund, H. J., CO adsorption on Ni(100) and Pt(111) studied by infrared–visible sum frequency generation spectroscopy : design and application of an SFG-compatible UHV–high-pressure reaction cell. *Topics in Catalysis* **2001,** *15* (1), 19-26.

23. Rupprechter, G., Surface vibrational spectroscopy from ultrahigh vacuum to atmospheric pressure: adsorption and reactions on single crystals and nanoparticle model catalysts monitored by sum frequency generation spectroscopy. *Physical Chemistry Chemical Physics* **2001,** *3* (21), 4621-4632.

24. Rupprechter, G., A surface science approach to ambient pressure catalytic reactions. *Catalysis Today* **2007,** *126* (1–2), 3-17.

3. Growth of ZrO_2 model ultrathin films on Pt_3Zr

3.1. Introduction

Zirconia is widely used in heterogeneous catalysis and is known as an excellent support (e.g. for Ni nanoparticles of reforming catalysts) and as catalyst itself, due to its favorable chemical and mechanical stability.[1] However, molecular mechanisms of the functionality of ZrO_2 and in particular of the oxide-metal interface, needs a better understanding. In order to conduct fundamental studies on ZrO_2 via surface-science methods it is required to prepare and thoroughly characterize a model zirconia support, an approach that has been successfully applied to various other oxides.[2,3,4] However, single crystal (bulk) ZrO_2 exhibits poor electrical conductivity and induces charging, which usually hinders applying many surface science techniques.[5] In order to overcome this problem ultrathin ZrO_2 films are prepared on a conducting substrate.

One way of growing such ultrathin films is to deposit and oxidize zirconium (Zr) on a suitable single crystal substrate, resulting in the epitaxial growth of (111) oriented films with cubic fluorite structure.[6,7,8,9] However, STM images of these films typically revealed ZrO_2 films with non-uniform thickness, containing a substantial amount of defects.[6] Furthermore, Zr evaporation is rather difficult and slow due to its high melting temperature and low vapour pressure at the melting point.

Recently, an alternative route to ultrathin ZrO_2 films via oxidation of a Pt_3Zr (0001) alloy single crystal has been reported by Antlanger et al.[10] Owing to the strong bond between Pt and Zr, and the fact that Pt is more inert to oxidation than Zr, the oxidation process is rather slow,

which is very favorable for growing ordered ultrathin films. After post-annealing, a planar oxide film consisting of an O-Zr-O trilayer was observed by STM.[10]

In order to further examine and better understand the mechanism of the formation and the structure of ultrathin ZrO_2 films grown on a Pt_3Zr (0001) single crystal, we applied (synchrotron based) XPS - including depth profiling - to study and identify the core level shifts of oxidic Zr species. Furthermore, we have CO as a probe molecule to investigate the continuity of the oxide films by performing TPD. LEED was used to study the structure of the oxide. In this study, we also collaborated closely with our project partners on DFT calculations, and STM. The former was used to support our findings of the core level shifts of oxidic Zr species, and the latter was used to observe directly the structure of the oxide after post-annealing at varied temperatures. Because DFT calculation and STM are not in the scope of this thesis, the reader is referred to our joint publication for details.[11]

3.2. Experimental

In order to prepare a model zirconia thin film, a $Pt_3Zr(0001)$ single crystal was cleaned by sputtering (8×10^{-6} mbar Ar, 2 kV) at room temperature (20 min), annealing in UHV at 1173 K (10 min), sputtering (20 min) during cooling from 673 K to 373 K, and finally annealing in UHV at 1173 K (10 min). After cleaning, the $Pt_3Zr(0001)$ single crystal was exposed to 1×10^{-7} mbar O_2 at 673 K for 30 min, followed by annealing in UHV at 1023 K or 1073 K for 20 min. This procedure follows the recipe described in the work of Antlanger et al,[10] but the final annealing temperatures are at the lower end of the range given there (up to 1173 K).

Synchrotron-based high resolution (HR) XPS measurements were carried out at beamline I511 at the MAX II electron storage ring (Lund setup), which is a soft-X-ray beamline equipped with a modified SX-700 monochromator for high photon energy resolution. Details of this setup can be found elsewhere.[12] In short, the system consists of two UHV chambers

with base pressures of ~5×10^{-10} mbar. The preparation chamber is equipped with a sputter gun and LEED (4-grid optics), which was used for cleaning the sample surface and to control surface structure, respectively. The analysis chamber is equipped with a SPECS PHOIBOS 150 NAP (near ambient pressure) analyzer. The binding energy of photoelectron peaks was calibrated by measuring the Fermi edge. The program XPSPEAK was used to conduct peak deconvolution and Shirley background subtraction. The Zr 3d spectra and O 1s spectra were fitted by use of Gauss-Lorentz sum functions with asymmetric peak shape (described by the parameters named TS (peak shape asymmetry) and TL (tail extension asymmetry)). The shapes and FWHM have been fixed and propagated along the series of spectra.

The TPD measurements were performed using the Vienna setup, which was described in detail in Chapter 2. TPD spectra were collected by a differentially pumped MKS eVision+ quadrupole mass spectrometer, and temperature ramping was performed by a Eurotherm 3216 PID controller, with a heating rate of 60 K/min.

3.3. Results and discussion

3.3.1. The trilayer oxide: LEED and CO TPD

The atomic surface structure of the Pt_3Zr alloy and of the thin oxide film were already reported in the study of Antlanger et al.[10] Pt_3Zr forms an ordered alloy and crystallizes in the Ni_3Ti ($D0_{24}$) structure, which can be considered as a hybrid of the face-centred cubic and hexagonally close-packed structures, with an in-plane lattice constant of a = 0.562 nm and 2×2 surface atoms in this unit cell. The oxide film consists of an O-Zr-O trilayer, which has an in-plane lattice constant of 0.350 nm. In addition, the consumption of Zr, when growing the oxide, results in at least one pure Pt(111) layer beneath the oxide (lattice constant of ≈0.28 nm), as shown schematically in Figure 3-1(b).

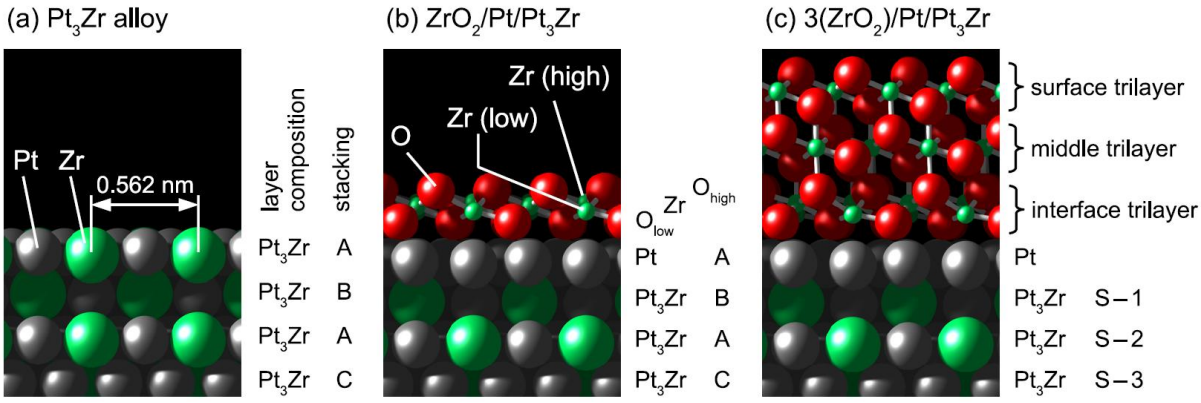

Figure 3-1. Side views of (a) the Pt_3Zr substrate and (b) the structure of the trilayer oxide film. Frame (c) shows the three-trilayer film used for core level calculations, together with the layer designations.[11]

The LEED images in Figure 3-2 show the electron diffraction pattern of the clean Pt_3Zr (0001) substrate as well as of the model zirconium oxide film after oxidation and post-annealing. The LEED patterns of the clean alloy (Figure 3-2(a)) clearly exhibits a hexagonal lattice, both first-order diffraction spots (corresponding to the 0.56 nm alloy cell; inner hexagon in Figure 3-2(a)) and second-order spots (vertices of the outer hexagon) can be observed. After oxidation and post-annealing (Figure 3-2(b)), the inner hexagon disappears, whereas the outer hexagon seems to remain. As mentioned, oxidation leads to the accumulation of pure Pt(111) at the interface, with a lattice constant of 0.28 nm, half of the lattice constant in the alloy. Therefore, the outer hexagon (blue) in Figure 3-2(b) can be assigned to the Pt(111) beneath the oxide. In addition, two additional hexagonal pattern appear, shown by the two black hexagons. Their lattice constant is 1.25 times that of Pt(111) and the rotation angle is ≈6° relative to Pt(111). These values are in line with the previous STM results (rotation angle ±6.8°),[10] and thus the two hexagonal pattern correspond to two rotational domains of the oxide. Also, additional spots could be observed, two of them are

indicated by orange circles. Such spots are assigned to a Moiré pattern which is caused by the superposition of the Pt(111) and the zirconium oxide lattice. In Figure 3-2(b), two moiré vectors are shown as difference vectors (red and green dashed line) between the reciprocal-space vectors of Pt(111) and ZrO_2 spots, and the two moiré spots marked by orange circles can be explained by adding the moiré vectors to a first-order spot of the Pt(111) lattice.

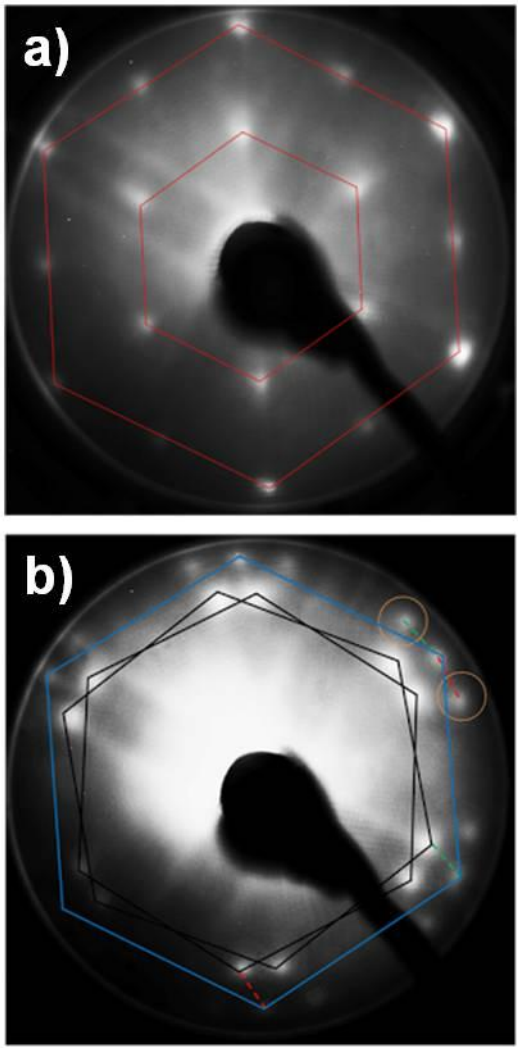

Figure 3-2. Diffraction pattern obtained from a) clean Pt_3Zr (0001) and from b) the Zr oxide film. Both patterns were acquired with an electron energy of 80 eV.[11]

One important issue regarding the growth of a thin film oxide on a substrate is its continuity. For systematic adsorption/reactivity studies the model oxide should entirely cover the

substrate, so that the interpretation is not interfered by signals resulting from the bare substrate. Extended STM studies have indicated complete coverage, but this should be corroborated by an integral method such as TPD using CO as probe molecule.

CO adsorption on Pt or Pt alloys has been well studied and excellent reference data exist.[13,14,15,16] On the clean Pt(111) surface, CO-TPD features a broad main peak at around 450 K, shifting to 410 K upon increasing the exposure, assigned to desorption from large and smooth terraces. CO desorption from steps produces a small hump around 500 K; even at highly stepped surfaces this signal reaches saturation already at an exposure of about 0.5 Langmuirs (L).[15] Figure 3-3 shows a CO dosage series of TPD spectra on the alloy and on the oxide. The desorption peak below 140 K results from CO desorbing from the Ta heating wires. In case of the alloy, at 0.1 and 0.5 L exposure a (main) species at around 373 K and a broader feature around 450 K are observed. As the exposure increases to 1 L, the main species grows and shifts to 340 K (due to intermolecular repulsion weakening the binding energy), similar to the behavior of CO desorption from large planar Pt(111) terraces. In contrast, the high-temperature 450 K shoulder is unaffected, resulting from CO adsorption on the steps of Pt(111). We thus attribute the main 373/340 K peak to CO desorption from Pt atoms in the alloy, and the small shoulder to CO desorption from Pt atoms at defects/steps.

Higher exposures (2, 5, 10 L) broaden (but do not shift) the main peak and also produce a low-temperature shoulder, which might be related to CO at Zr sites (1/4 of all surface atoms).

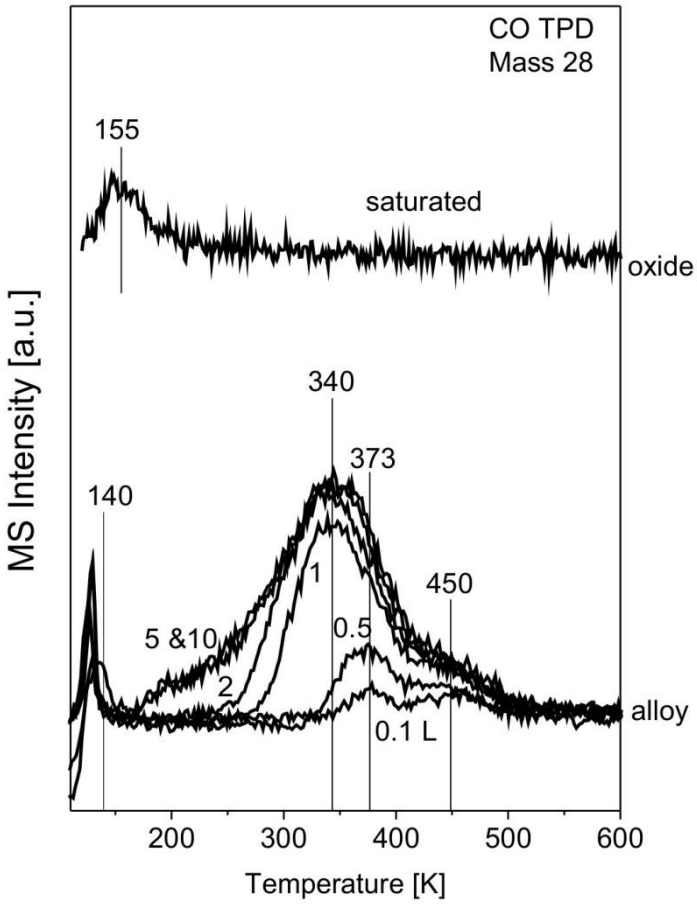

Figure 3-3. CO-TPD spectra of clean Pt_3Zr alloy (0.1 L, 0.5 L, 2 L, 5 L and 10 L CO dosed at 90 K) and of Zr-oxide covered Pt_3Zr (cooling in $1\times^{-6}$ mbar CO from 300 K to 120 K).[11]

The adsorption energy was also estimated by applying the Redhead equation.[17] A pre-exponential factor for desorption of 10^{13} s^{-1} was used. For the alloy, the desorption maximum at a temperature of 340 K corresponds to a desorption energy of $E_{TPD} \approx 0.91$ eV.

For the oxide annealed at 1073 K, CO desorption was observed at 155 K (for CO saturation; topmost trace in Fig. 3-3), corresponding to a desorption energy of ≈ 0.42 eV (again assuming a pre-exponential factor of 10^{13} s^{-1}), which is consistent with the value calculated by DFT.[11] Altogether, this clearly proves that the alloy substrate is fully covered by the thin oxide film, and no Pt_3Zr or Pt is exposed at the solid-vacuum (or solid-gas) interface.

3.3.2. Core level shifts: two oxide species

The growth of the oxide on Pt_3Zr was also monitored by synchrotron-based HR-XPS, as shown in Figure 3-4 and Table 3-1. The spectra were recorded at normal emission with photon energies of 320 and 670 eV for the Zr 3d and O 1s range, respectively, yielding in both cases photoelectrons with a kinetic energy of ~140 eV. With that kinetic energy for both signals only the photoelectrons from the topmost surface layers escape. By use of NIST Standard Reference Database 71,[18] the inelastic mean free path (IMFP) for ZrO_2 corresponding to 140 eV is 0.54 nm, showing that mainly the first two layers are probed. The Zr 3d spectrum of the clean alloy exhibits a pronounced doublet at 179.6 eV and 182.0 eV due to Zr $3d_{5/2}$ and Zr $3d_{3/2}$ with a spin orbit splitting of 2.4 eV, respectively. In addition, another doublet with much lower intensity was observed at 180.7 eV and 183.1 eV. Almost no signal could be detected in the O 1s region; thus the doublet with higher intensity is assigned to metallic Zr in Pt_3Zr, whereas the small features were assigned to Zr bound to residual oxygen. For comparison with pure Zr, we will use the value of 178.6 eV reported for a Zr(0001) single crystal,[19] thus the alloyed Zr is shifted to higher binding energy (BE) by +1.0 eV.

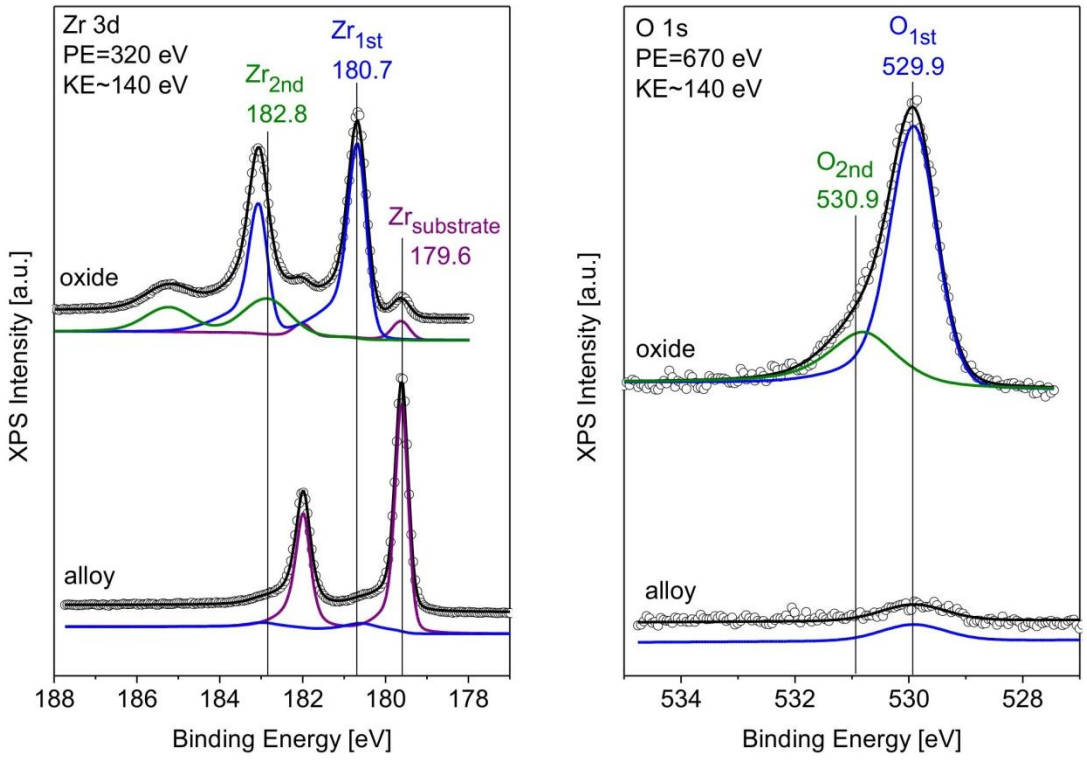

Figure 3-4. Zr 3d (left) and O 1s (right) spectra of the clean alloy and of the oxide annealed at 1023 K (spectra taken at 300 K, kinetic energy of photoelectrons ≈ 140 eV).[11]

After oxidation at 673 K and post-annealing at 1023 K the signal of metallic (alloyed) Zr from the substrate ($Zr_{substrate}$) could still be observed, although strongly attenuated by the oxide and interfacial Pt. However, the Zr 3d spectrum now also displays two doublets, originating from two different oxidic species (Zr_{1st} and Zr_{2nd}). Detailed peak deconvolution shows that the main peak Zr_{1st} is located at 180.7 eV (Zr $3d_{5/2}$), shifted by +2.1 eV relative to pure Zr. In contrast, the smaller Zr_{2nd} species is positioned at 182.8 eV, shifted by +4.2 eV with respect to pure Zr. This position is characteristic of bulk ZrO_2 (around 183 eV), as indicated by experiments.[20,21] The shift between Zr_{1st} and Zr_{2nd} is 2.1 eV and the ratio of the intensities is 3:1, based on the integration of the peak areas. In the O 1s region we also observe two species, the main peak (O_{1st}) is located at 529.9 eV, with a shoulder (O_{2nd}) at approximately 530.9 eV, and the ratio of the intensities is again 3:1.

XPS studies of thin Zr oxide layers grown by oxidation of metallic Zr (Zr single crystals and polycrystalline foil) were reported in the literature.[19,20,22] For oxides of several nanometer thickness, Zr^{4+} generally shifts ~+4.5 eV relative to metallic Zr, whereas binding energy shifts of +2.5 to +3.5 eV were attributed to suboxides (formed upon exposure to low O_2 amounts).[19,20] An exact identification of the different oxide components has, however, not yet been achieved. Gao et al.[9] applied XPS to study the growth of ZrO_2 film on Pt(111) by vapor deposition of zirconium in an oxygen atmosphere (10^{-7} Torr). They also observed a Zr $3d_{5/2}$ binding energy of 182.9 eV corresponding to bulk-like ZrO_2 up to ≈5 ML; an additional shift of +0.7 eV at higher thickness (8.3 ML) was attributed to surface charging due to the poor oxide conductivity.[9] As also the substrate Pt line was reported to be shifted by about the same amount, this additional shift is questionable.

In summary, Zr_{2nd} has similar binding energy as Zr^{4+} species reported in the literature, whereas Zr_{1st} has a binding energy similar to the literature value attributed to Zr suboxide. These values have been summarized in Table 3-1.

Table 3-1.

Summary of literature values and our results for the binding energy of the $Zr3d_{5/2}$ levels for Zr and Zr oxides.[11]

	Zr $3d_{5/2}$	Reference
Substrates (bulk)		
Pure Zr (single crystal)	178.6	[19]
Pt_3Zr	179.6	This work
ZrO_2 (thicker layer)		
ZrO_2 (oxidation of Zr single crystal)	183.1	[19]
ZrO_2 grow by PVD on Pt(111)	182.9	[9]
Trilayer ZrO_2/Pt/Pt_3Zr		
Zr_{1st} (oxidation of Pt_3Zr)	180.7	This work
Zr_{2nd} (oxidation of Pt_3Zr)	182.8	This work

In order to determine the stoichiometry of the ultrathin oxide grown on the Pt_3Zr substrate the following equation is used:

$$\frac{N_{Zr}}{N_O} = \frac{I_{Zr}}{\sigma_{Zr} \times F_{Zr}} \times \frac{\sigma_O \times F_O}{I_O} \qquad (3\text{-}1)$$

I represents the intensities of photoelectrons, σ represents the cross section of atoms, taken from the published atomic subshell photoionization cross sections,[23] and F_x represents the flux of incident photons, given by the flux calibration for the I511 beamline in MAX-lab. Specifically, σ_{Zr} and σ_O are 4.259 Mb and 0.313 Mb,[30] and F_{Zr} and F_O were 1.47×10^{13} and 4.36×10^{12} photons/s in our experiment. The calculations result in a Zr to O ratio of 0.55 (1:1.82) for both oxidic species. Within the accuracy expected for such a calculation this result fits the Zr to O ratio of 0.50 in ZrO_2. Thus, both of the oxidic species should be assigned to ZrO_2 rather than to a suboxide.

As mentioned above,[9] the increase of binding energy with increasing thickness of ZrO_2 films (between 5.2 and 8.3 ML average film thickness deposited on Pt) has been attributed to surface charging. If charging would play a significant role in our experiments, it should be much more pronounced in the synchrotron-based experiments, where the photon flux (and, hence the current of photoelectrons leaving the sample) is high, compared to experiments with a laboratory x-ray source. However, we did not find any difference between the core level shifts of our synchrotron and laboratory measurements (the latter using an Al Kα source operated at 300 W). Thus, we exclude charging as a reason for the different '1st' and '2nd' components of the ZrO_2 spectra.

To examine the two oxide features in more detail we have also performed XPS depth profiling, by varying the incident excitation energy, in order to determine the thickness of the two oxidic species (Figure 3-5). The incident photon energies were 320, 440 and 560 eV for Zr 3d, leading to kinetic energies of photoelectrons of 140, 260 and 380 eV, respectively. The

corresponding IMFP are 0.54, 0.72 and 0.90 nm, respectively.[18] For O 1s corresponding measurements were taken at 670 and 910 eV (kinetic energy of 140 and 380 eV, respectively). As a result, the signal for $Zr_{substrate}$ rises with increasing kinetic energy (increasing probing depth), consequently the relative intensities of both Zr_{1st} and Zr_{2nd} decrease (Figure 3-6). However, with increasing probing depth the higher binding energy component Zr_{2nd} decreases less in intensity than Zr_{1st} does, thus Zr_{1st}/Zr_{2nd} decreases, what leads to the result that Zr_{2nd} is more "3-dimensional". In the O 1s region the ratio O_{1st}/O_{2nd} also decreases with probing depth (from 3.04 to 2.42). Therefore, it is clear that Zr_{2nd} is "thicker" than Zr_{1st}, meaning that the former grows three dimensionally, whereas the latter is more planar.

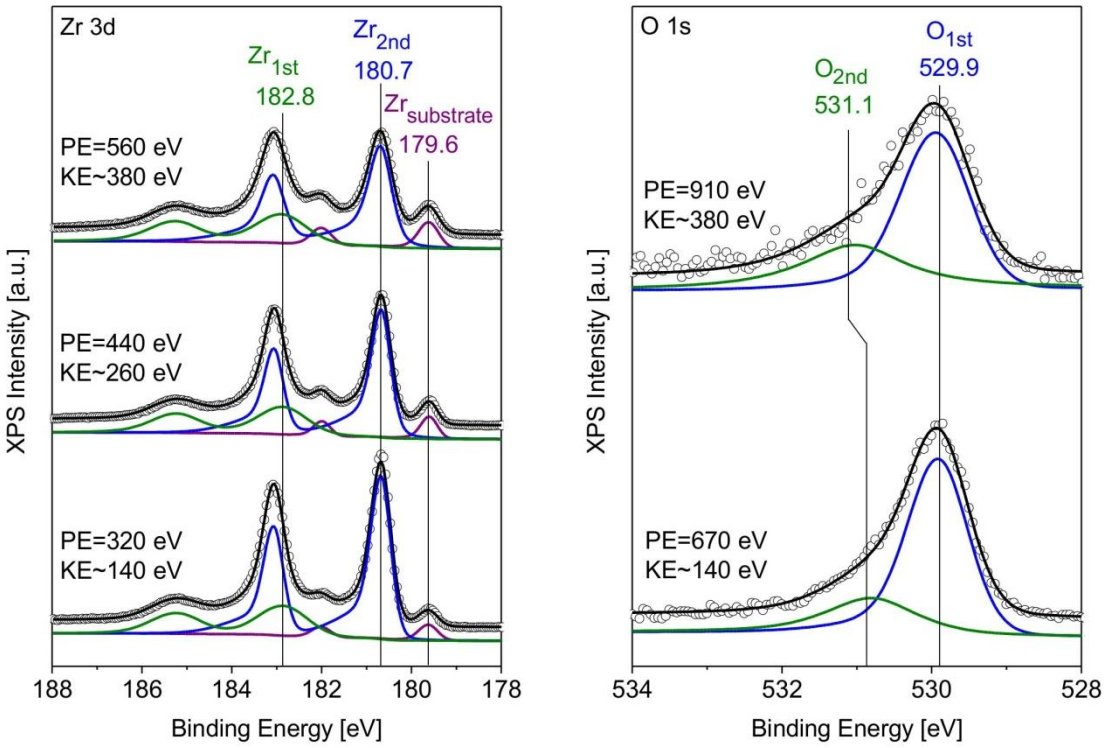

Figure 3-5. Zr 3d (left) and O 1s (right) spectra of the oxide at different kinetic energies of the photoelectrons (spectra taken at 300 K).[11]

.

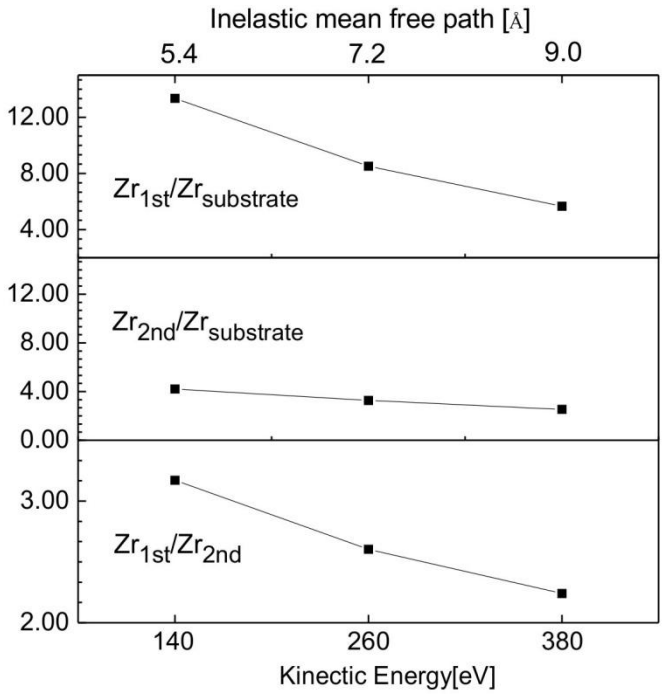

Figure 3-6. Ratio between different Zr species for kinetic energies of the photoelectrons of 140, 260 and 380 eV.[11]

Obviously, we produced two stoichiometric ZrO_2 types of the same Zr to O ratio, but with different thickness and binding energies. Our data suggest that Zr_{1st} corresponds to the surface oxide tri-layer film, whereas Zr_{2nd} belongs to a thicker "bulk" oxide. Additional support also come from both DFT calculations and STM.[11] Concerning XPS peak fitting, note that asymmetry (high-energy tail) is induced by many-body interactions of photoelectrons with free electrons at the Fermi edge. The ultrathin oxide film has a well-defined Fermi edge (like a metal), and thus Zr_{1st} exhibits asymmetry, whereas the electron density around the Fermi level of the more insulating clusters is much less, leading to more symmetric Zr_{2nd}.

3.3.3. Influence of the annealing temperature

Previous STM studies have shown that a planar oxide-covered surface was obtained after oxidation at 673 K and post-annealing above 1023 K,[10] annealing to lower temperatures resulted in many islands. Upon post-annealing at 1023 K, our synchrotron XPS results show that the intensity ratio between Zr_{1st} and Zr_{2nd} is 3.2:1. As explained above, Zr_{1st} and O_{1st} correspond to the tri-layer film, whereas the Zr_{2nd} and O_{2nd} should be assigned to a thicker component, namely ZrO_2 clusters. Thus, no homogeneous trilayer oxide is formed after annealing at 1023 K, but STM indicates a homogeneous oxide after annealing at higher temperatures, up to the point where the oxide decomposes (>1173 K).[10] This means that the surface state after oxidation strongly depends on the post-annealing temperature. Therefore, a study by synchrotron-based XPS of the oxides before and after annealing at different temperatures should enable us to better understand the formation of the ZrO_2 ultrathin film and the ZrO_2 clusters as a function of the post-annealing temperature.

After oxidation at 673 K the Zr 3d spectrum exhibits both the metallic (alloy) Zr signal of the substrate underneath and broad peaks of oxidic species Zr_{oxide} (Figure 3-7). Zr_{oxide} is shifted by +2.9 eV relative to pure Zr. This shift is larger than the one of ZrO_2 film ($Zr_{1st(film)}$, +2.1 eV) but smaller than that of ZrO_2 clusters ($Zr_{2nd(cluster)}$, +4.2 eV). Furthermore, analysis of the stoichiometry revealed a Zr to O ratio of 0.2 (1:5). Likewise, the Pt 4f spectrum shows both the metallic (alloy) Pt signal ($4f_{7/2}$ at 71.4 eV) and an additional oxidic species (Pt_{ox}), which is shifted by +0.5 eV relative to alloy Pt. It is known that O_2 can dissociate on Pt(111) above 160 K[24] and it can form Pt-O and PtO_2-like surface oxides.

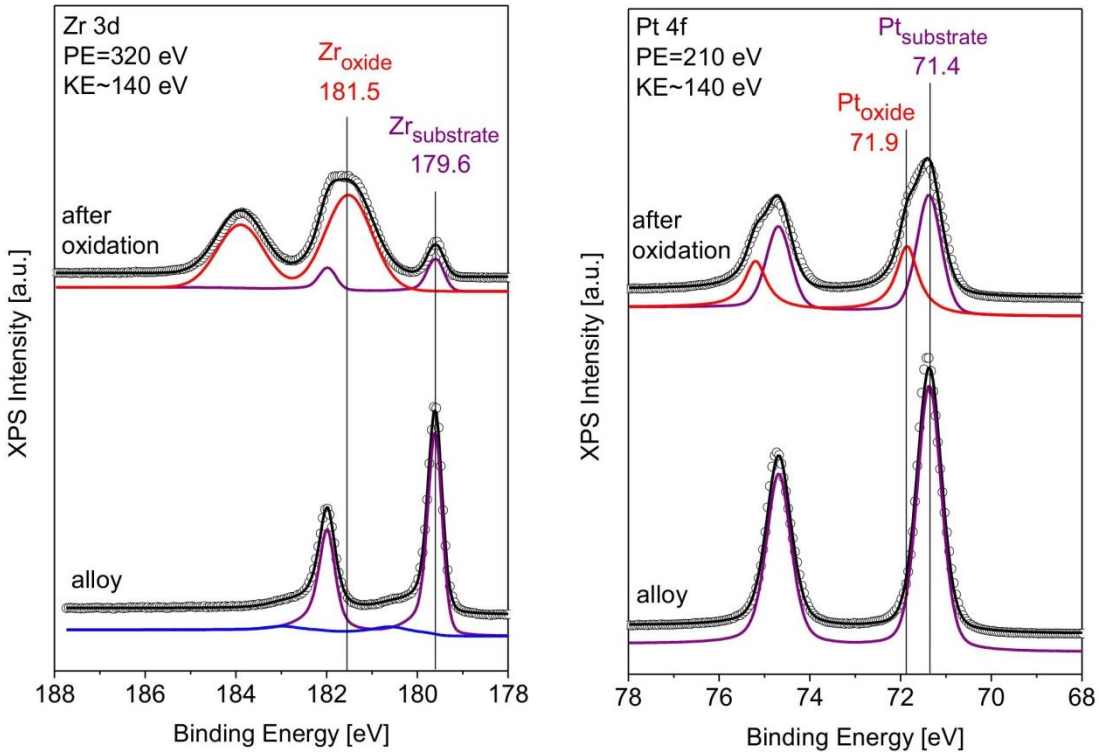

Figure 3-7. Zr 3d (left) and Pt 4f (right) spectra of the clean alloy and of the oxide prepared by oxidation of alloy at 673 K in 1×10^{-7} mbar O_2 for 30 min (spectra taken at 300 K, kinetic energy of photoelectrons ≈ 140 eV).[11]

Chemisorbed oxygen induces a shift of ~0.6 eV of the Pt 4f peak relative to surface metallic Pt[25,26] (i.e. from 70.5 to 71.1 eV). For various surface oxide phases, higher Pt 4f binding energies are reported at around ~72.3 eV.[27,28] The Pt_{ox} peak in our study (71.9 eV) therefore lies between the peaks of chemisorbed O on the Pt(111) surface (~71.1 eV) and those of heavily oxidized PtO_x surface oxides (~72.3 eV). Considering that Zr also affects the Pt BE, the identification of the PtO_x signal must remain uncertain, but the relatively low chemical potential of oxygen (μ_O = –1.37 eV) at 10^{-7} mbar O_2 and 673 K is probably outside the stability range of any Pt surface oxides. Together with the observation of islands by STM,[10] our results imply that the oxidation of Pt_3Zr leads to an intermediate state of disordered ZrO_x

islands. The high O/Zr ratio and the Pt 4f spectra indicate additional oxygen binding to Pt, e.g. at the interface or in the form of O dissolved in near-surface layers of the substrate.

When the thin oxide film was then post-annealed at 923 K the two distinct ZrO_2 species ($Zr_{1st(film)}$ and $Zr_{2nd(cluster)}$) were already formed (Figure 3-8), and the Pt_{ox} signal vanished (Figure 3-9). The intensity of the total oxidic Zr signal increased, whereas the total O signal remained unchanged. Apparently, post-annealing in ultra-high vacuum pulled up more Zr atoms from the alloy substrate underneath, entering the surface layer and reacting with the excess oxygen created by breaking Pt-O bonds, forming ZrO_2 (as indicated by the same Zr:O ratio as obtained at higher *T* for both film and clusters). If the amount of ZrO_2 is too high to be accommodated in a trilayer oxide film, the remaining ZrO_2 will form clusters.

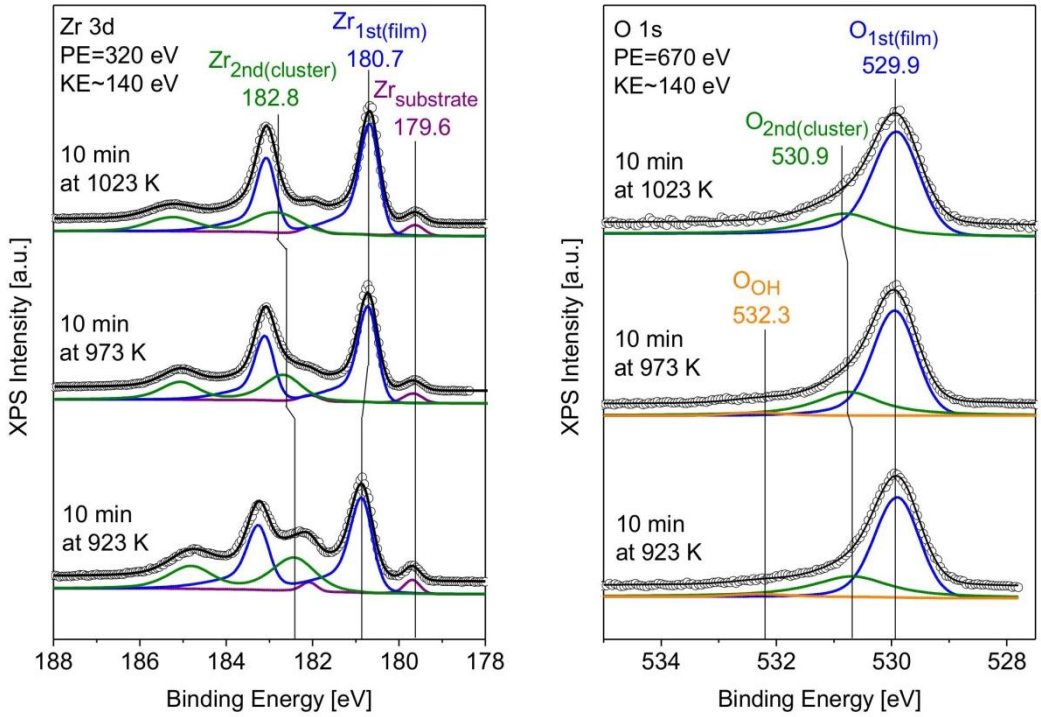

Figure 3-8. Zr 3d (left) and O 1s (right) spectra of the oxide formed at 673 K and post-annealed at 923 K, 973 K and 1023 K (spectra taken at 300 K, kinetic energy of photoelectrons ≈ 140 eV).[11]

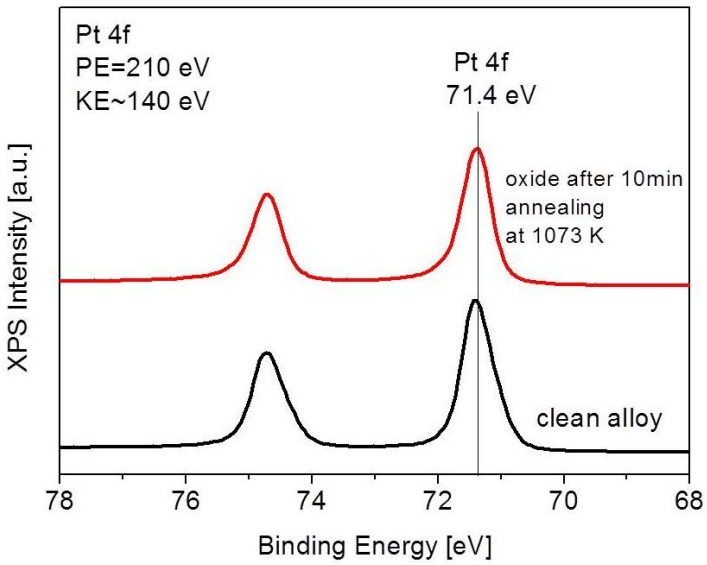

Figure 3-9. Pt 4f spectra of the clean alloy and the oxide after 10 min annealing at 1073 K (spectra taken at 300 K, kinetic energy of photoelectrons ≈ 140 eV).[11]

XPS also shows that post-annealing at 923 K results in a $Zr_{1st(film)}$ to $Zr_{2nd(cluster)}$ ratio of 2:1, which increases to 2.4:1 upon post-annealing at 973 K, and further increases to 3.2:1 as the post-annealing temperature reaches 1023 K (Figure 3-10).

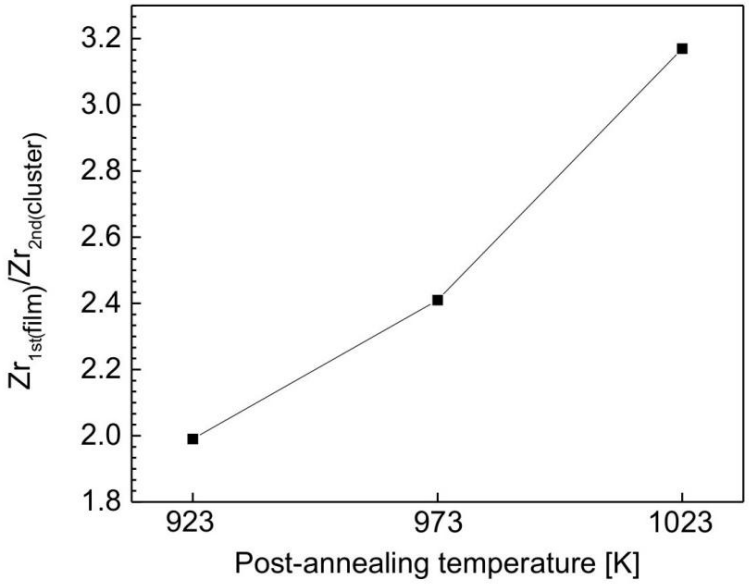

Figure 3-10. The ratio between $Zr_{1st(film)}$ and $Zr_{2nd(cluster)}$ after annealing at 923 K, 973 K and 1023 K.[11]

In contrast, the $Zr_{1st(film)}$ to $Zr_{substrate}$ ratio does not change significantly with increasing post-annealing temperature, staying around 18.0. Assuming that the clusters are thick enough to block the $Zr_{substrate}$ signal, this indicates that the decomposition of the clusters leads to a tri-layer film; i.e., all the area initially covered by clusters is then covered by the trilayer film, as already indicated by our TPD data.

To properly fit the O 1s spectra in Figure 3-8, a very weak component at 532.3 eV was included. Most likely, this is due to minute amounts of O dissolve into the subsurface. OH groups or H_2O would be positioned at different binding energies (please see chapter 4). And C 1s did not indicate any carbon so that (adventitious) C-O containing species can be excluded. In any case, this feature was extremely weak.

Previous STM studies show that when annealing temperature exceeds 1173 K, in some areas the trilayer oxide disappears, and the substrate is exposed to the surface.[10] Considering the strong Zr–O bonds and the low vapor pressure of ZrO_2, the only explanation is the dissolution of oxygen into the Pt_3Zr substrate. This observation is also a clue to why the oxide clusters disappear when annealing the sample: With increasing temperature, more and more oxygen dissolves in the substrate. Since the substrate is Zr-depleted after forming the oxide, the remaining Zr is easily accommodated in the substrate as well.

This explanation also suggests that the trilayer ZrO_2 film is thermodynamically more favorable than thick ZrO_2 clusters on the surface. This essentially means that ZrO_2 grows in Stranski-Krastanov mode, first a monolayer forms, then the extra material creates 3D clusters. In the group of our project partner Prof. Michael Schmid, the same mechanism has recently been suggested for ZrO_2 grown on Pd_3Zr.[29] Upon dissolution of oxygen, the reverse sequence happens: First the 3D clusters disappear, and then the (more favorable) 2D trilayer begins to dissolve.

3.4. Summary

We have studied the ultrathin ZrO_2 oxide film formed upon oxidation and annealing of a $Pt_3Zr(0001)$ single crystal, employing a combination of (synchrotron) HR-XPS, TPD and LEED. The results indicate that at moderate annealing temperatures the oxide overlayer is comprised of a trilayer film (O-Zr-O), as well as of oxide clusters. The two species have different core level shifts, +2.1 eV for the trilayer film, and +4.2 for the clusters (both referenced to pure Zr); the latter have a clearly insulating nature. The oxide clusters decompose upon high-temperature (>1023 K) annealing, resulting in the formation of a continuous tri-layer ZrO_2 film that is well-suited as model support for reforming catalysts or fuel cell anodes.

Our results also indicate that the usual assignment of Zr core level shifts between those of metallic Zr and bulk ZrO_2 as suboxides is not necessarily correct. The ultrathin trilayer oxide clearly has ZrO_2 stoichiometry (with O binding to the Zr, not to the substrate) and a band gap; nevertheless it would be interpreted as a substoichiometric oxide based on its core level shift. We consider it likely that what has been assigned to ZrO_x suboxides based on core level shifts is in many cases rather ultrathin ZrO_2 or metal/ZrO_2 interface, as the substrate beneath also electronically affects the ultrathin ZrO_2.

Bibiliography

1. Tanabe, K.; Yamaguchi, T., Acid-base bifunctional catalysis by ZrO_2 and its mixed oxides. *Catalysis Today* **1994,** *20* (2), 185-197.

2. Freund, H.-J.; Pacchioni, G., Oxide ultra-thin films on metals: new materials for the design of supported metal catalysts. *Chemical Society reviews* **2008,** *37* (10), 2224-42.

3. Kuhlenbeck, H.; Shaikhutdinov, S.; Freund, H.-J., Well-ordered transition metal oxide layers in model catalysis--a series of case studies. *Chemical reviews* **2013,** *113* (6), 3986-4034.

4. Diebold, U.; Li, S.-C.; Schmid, M., Oxide surface science. *Annual review of physical chemistry* **2010,** *61*, 129-48.

5. Lou, J. R.; Hess, U.; Mitchell, K. A. R., The growth of zirconium oxide thin films on Au(111) single-crystal surfaces. *Applied Surface Science* **1992,** *62*, 175-180.

6. Maurice, V.; Salmeron, M.; Somorjai, G. A., The epitaxial growth of zirconium on Pt(111) single crystal surfaces. *Surface Science* **1990,** *237*, 116-126.

7. Meinel, K.; Schindler, K.-M.; Neddermeyer, H., Growth, structure and annealing behaviour of epitaxial ZrO2 films on Pt(111). *Surface Science* **2003,** *532-535*, 420-424.

8. Meinel, K.; Eichler, A.; Förster, S.; Schindler, K. M.; Neddermeyer, H.; Widdra, W., Surface and interface structures of epitaxial ZrO2 films on Pt(111): Experiment and density-functional theory calculations. *Physical Review B* **2006,** *74* (23), 235444-235444.

9. Gao, Y.; Zhang, L.; Pan, Y. H.; Wang, G. D.; Xu, Y.; Zhang, W. H.; Zhu, J. F., Epitaxial growth of ultrathin ZrO2(111) films on Pt(111). *Chinese Science Bulletin* **2011,** *56* (6), 502-507.

10. Antlanger, M.; Mayr-schmölzer, W.; Pavelec, J.; Mittendorfer, F.; Redinger, J.; Varga, P.; Diebold, U.; Schmid, M., Pt_3Zr(0001): A substrate for growing well-ordered ultrathin zirconia films by oxidation. *Physical Review B* **2012,** (0001), 035451-035451.

11. Li, H.; Choi, J.-I. J.; Mayr-Schmölzer, W.; Weilach, C.; Rameshan, C.; Mittendorfer, F.; Redinger, J.; Schmid, M.; Rupprechter, G., Growth of an Ultrathin Zirconia Film on Pt3Zr Examined by High-Resolution X-ray Photoelectron Spectroscopy, Temperature-Programmed Desorption, Scanning Tunneling Microscopy, and Density Functional Theory. *The Journal of Physical Chemistry C* **2014,** *119* (5), 2462-2470.

12. Schnadt, J.; Knudsen, J.; Andersen, J. N.; Siegbahn, H.; Pietzsch, A.; Hennies, F.; Johansson, N.; Mårtensson, N.; Öhrwall, G.; Bahr, S.; Mähl, S.; Schaff, O., The new ambient-pressure X-ray photoelectron spectroscopy instrument at MAX-lab. *Journal of synchrotron radiation* **2012,** *19* (Pt 5), 701-704.

13. Sun, Y. N.; Qin, Z. H.; Lewandowski, M.; Shaikhutdinov, S.; Freund, H. J., CO adsorption and dissociation on iron oxide supported Pt particles. *Surface Science* **2009,** *603* (20), 3099-3103.

14. Rupprechter, G.; Dellwig, T.; Unterhalt, H.; Freund, H. J., CO adsorption on Ni(100) and Pt(111) studied by infrared–visible sum frequency generation spectroscopy : design and application of an SFG-compatible UHV–high-pressure reaction cell. *Topics in Catalysis* **2001,** *15* (1), 19-26.

15. Hopster, H.; Ibach, H., Adsorption of CO on Pt(111) and Pt6(111)x(111) studied by high resolution electron energy loss spectroscopy and thermal desorption spectroscopy. *Surface Science* **1978,** *77*, 109-117.

16. Rupprechter, G.; Dellwig, T.; Unterhalt, H.; Freund, H. J., High-Pressure Carbon Monoxide Adsorption on Pt(111) Revisited: A Sum Frequency Generation Study †. *The Journal of Physical Chemistry B* **2001,** *105* (18), 3797-3802.

17. P.A.Redhead, Thermal Desorption of Gases. *VACUUM* **1962,** *12* (4), 203-211.

18. Powell, C. J.; Jablonski, A., NIST Electron Inelastic-Mean-Free-Path Database, NIST Standard Reference Database 71 version 1.2. *Gaithersburg* **2010**.

19. Bakradze, G.; Jeurgens, L. P. H.; Mittemeijer, E. J., The different initial oxidation kinetics of Zr(0001) and Zr(1010) surfaces. *Journal of Applied Physics* **2011,** *110* (2), 024904-024904.

20. Morant, C.; Sanz, J. M.; Galan, L.; Soriano, L.; Rueda, F., An XPS study of the interaction of oxygen with zirconium. *Surface Science* **1989,** *218*, 331-345.

21. Bakradze, G.; Jeurgens, L. P. H.; Mittemeijer, E. J., Valence-Band and Chemical-State Analyses of Zr and O in Thermally Grown Thin Zirconium-Oxide Films : An XPS Study. *The Journal of Physical Chemistry C* **2011,** *115*, 19841-19848.

22. De Gonzalez, C. O.; Garcia, E. A., An X-Ray photoelectron spectroscopy study of the surface oxidation of zirconium. *Surface Science* **1988,** *193*, 305-320.

23. Yeh, J. J.; Lindau, I., Atomic Subshell Photoionization Cross Sections and Asymmety Parameters: 1⩽Z⩽103. *Atomic Data and Nuclear Data Taples* **1985,** *32* (l), 1-155.

24. Avery, N. R., Adsorption of formic acid on clean and oxygen covered Pt(111). *Applications of Surface Science* **1982,** *11–12* (0), 774-783.

25. Miller, D. J.; Öberg, H.; Kaya, S.; Sanchez Casalongue, H.; Friebel, D.; Anniyev, T.; Ogasawara, H.; Bluhm, H.; Pettersson, L. G. M.; Nilsson, A., Oxidation of Pt(111) under Near-Ambient Conditions. *Physical Review Letters* **2011,** *107* (19), 195502-195502.

26. Puglia, C.; Nilsson, A.; Hernnäs, B.; Karis, O.; Bennich, P.; Martensson, N., Physisorbed , chemisorbed and dissociated O2 on Pt(111) studied by different core level spectroscopy methods. *Surface Science* **1995,** *342*, 119-133.

27. Kim, Y. S.; Bostwick, A.; Rotenberg, E.; Ross, P. N.; Hong, S. C.; Mun, B. S., The study of oxygen molecules on Pt(111) surface with high resolution x-ray photoemission spectroscopy. *The Journal of chemical physics* **2010,** *133* (3), 034501-034501.

28. Parkinson, C. R.; Walker, M.; McConville, C. F., Reaction of atomic oxygen with a Pt(111) surface: chemical and structural determination using XPS, CAICISS and LEED. *Surface Science* **2003,** *545* (1-2), 19-33.

29. Choi, J. I. J.; Mayr-Schmölzer, W.; Mittendorfer, F.; Redinger, J.; Diebold, U.; Schmid, M., The growth of ultra-thin zirconia films on Pd3Zr(0001). *Journal of physics. Condensed matter* **2014,** *26* (22), 225003-225003.

4. Interaction of Water with Ultrathin ZrO_2 Films

4.1. Introduction

Typically, the surface of ZrO_2 is covered with hydroxyl (OH) groups,[1] which is of great importance in surface chemistry and catalysis, due to the reactivity of OH. Hydroxyl groups can directly participate in reactions,[2,3] or they can affect the size (dispersion) and the structure of the metal nanoparticles grown on oxides.[4,5,6,7] The interaction of water with surface metal cations plays an important role in the formation of hydroxyl groups,[8] and it has been shown that both the defects on the oxide surface[9] as well as water pressure[10] influence the hydroxylation process.

The hydroxylation of technical ZrO_2 has been mainly studied by transmission FT-IR spectroscopy.[11,12,13] It has been reported that free hydroxyl groups are located at terminal or bridge sites of Zr cations, giving rise to two sharp adsorption bands at around 3770 cm^{-1} and 3670 cm^{-1}, respectively. Moreover, water also strongly bonds to ZrO_2 molecularly (i.e. non-dissociatively), exhibiting a broad absorption band in IR. However, only few fundamental studies have been performed in order to study the hydroxylation of ZrO_2 via a surface science approach.[14,15] Maurice et al. applied TPD to study the interaction of H_2O with pristine and defective ZrO_2 thin films grown on Pt(111).[15] Hydrogen (H_2) desorption from the defective surface was observed at 340, 420 and 500 K indicating the dissociation of H_2O molecules on the surface, whereas only H_2O desorption was observed on the ordered pristine ZrO_2 thin film. However, the potentially different sites for H_2O dissociation (based on the three different H_2 desorption temperatures) were not analyzed in detail and the electronic structure of ZrO_2 upon water adsorption was also not studied. Thus, there is still a need to systematically study the

influence of surface defects and H_2O pressure on H_2O adsorption and dissociation on ZrO_2 thin films. We have thus revisited the interaction of water with pristine and defective ZrO_2 at pressures ranging from UHV to 10^{-3} mbar, applying lab-based and synchrotron-based NAP-XPS, TPD, and IRAS.

4.2. Experimental

The model ZrO_2 thin film was prepared by the procedure described in Chapter 2 (oxidation and post-annealing of a $Pt_3Zr(0001)$ single crystal). The laboratory measurements were conducted using the Vienna setup, which was also introduced in detail in Chapter 2. In an effort to exclude effects of residual H_2O (at least for TPD and IRAS), D_2O cleaned by repeated freeze-pump-thaw cycles was used for XPS, TPD and IRAS. For TPD and XPS, D_2O was dosed via a capillary doser at a background pressure of 1×10^{-8} mbar (distance to the sample was 1 mm), yielding an effective pressure of $\sim1\times10^{-6}$ mbar of D_2O at the sample surface. TPD spectra were collected by a differentially-pumped MKS eVision+ quadrupole mass spectrometer, and temperature ramping was performed by a Eurotherm 3216 PID controller, with a heating rate of 60 K/min. Photoelectron spectra were collected by using Al Kα radiation (1486.6 eV) at an electron emission angle of 60º. Constant pass energy of 20 eV was used for the hemispherical energy analyzer (SPECS PHOIBOS 150). The program XPSPEAK was used for peak deconvolution, using the same peak fitting procedure as described in Chapter 3. For IRAS experiments, D_2O was dosed via a leak valve, and spectra were collected at grazing incidence on a Bruker IFS66v/S spectrometer with a liquid nitrogen-cooled mercury-cadmium-telluride (MCT) detector. All spectra were obtained by averaging 2048 interferograms with spectral resolutions of 4 cm^{-1}. Synchrotron-based elevated NAP-XPS measurements were carried out at beamline I511 at the MAX II electron storage ring

(Lund setup), a detailed description is included in Chapter 2 and 3. H_2O was used for the synchrotron-based experiments.

In order to create a limited number of surface defects such as oxygen vacancies we have applied "soft sputtering" of the ZrO_2 thin films, using 8×10^{-7} mbar Ar (450 eV at 300 K for only 2 minutes). As discussed below, this creates defects and destroys the long range order of the oxide, but the overall film composition, CO adsorption properties and full coverage of the substrate remain (nearly) unchanged.

4.3. Results and discussion

4.3.1. Characterization of pristine and defect-enriched oxide films

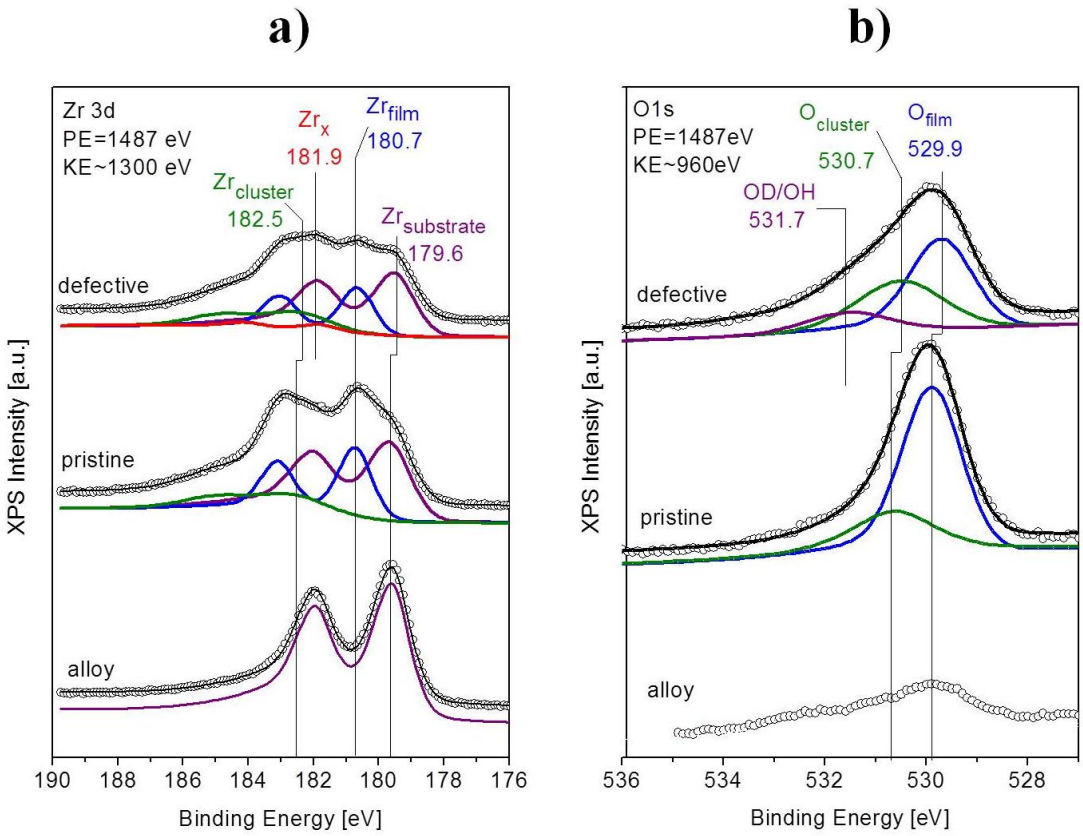

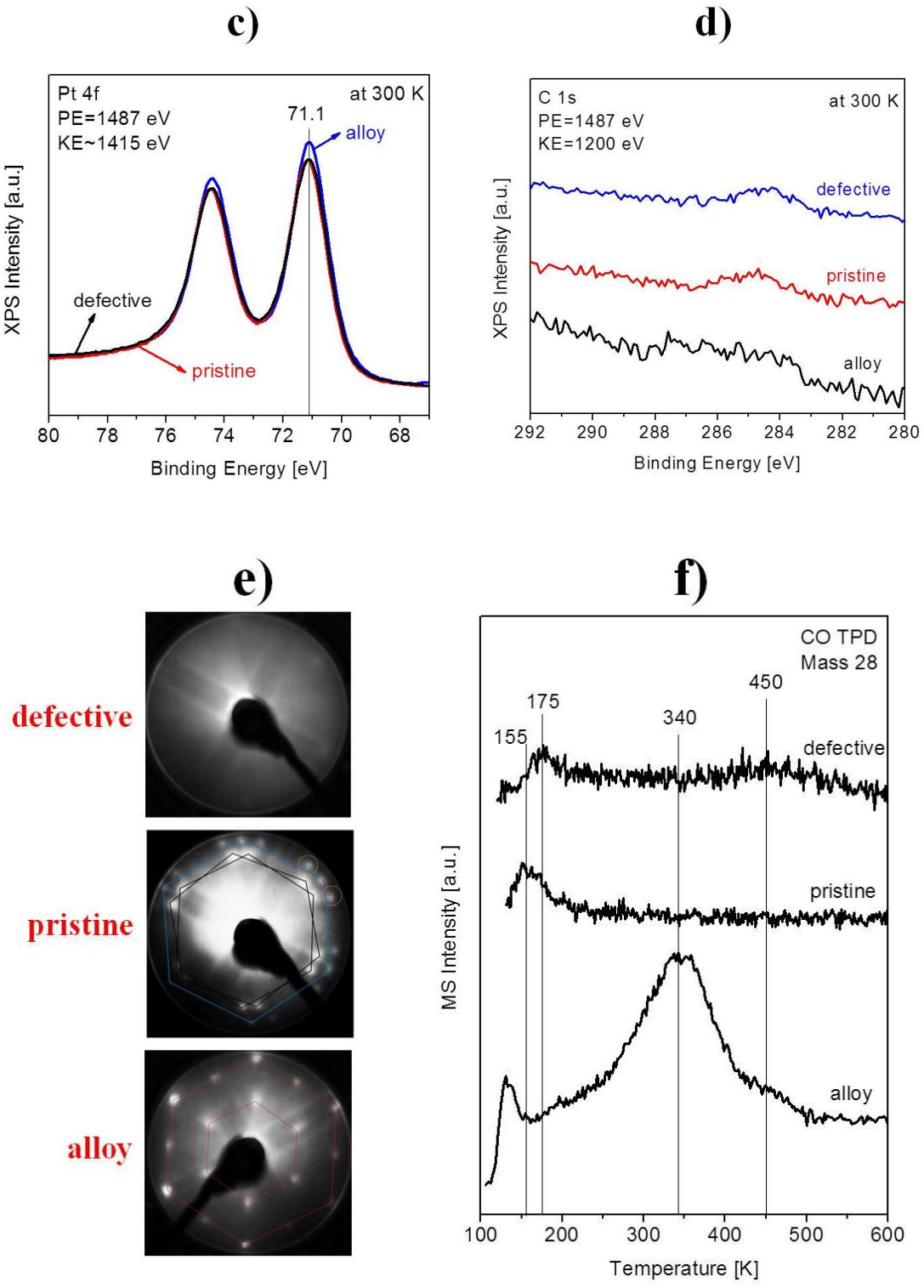

Figure 4-1. (a) Zr 3d, (b) O 1s, (c) Pt 4f and (d) C 1s XP spectra of clean $Pt_3Zr(0001)$ alloy, pristine ZrO_2/Pt_3Zr and defective ZrO_2/Pt_3Zr measured with lab XPS (spectra taken at 300 K). (e) Diffraction pattern obtained from corresponding samples, all patterns were required with an electron energy ≈ 80 eV. (f) CO-TPD spectra of Pt_3Zr alloy (10 L CO dosed at 90 K), pristine Pt_3Zr/ZrO_2 and defective Pt_3Zr/ZrO_2 (cooling in $1\times^{-6}$ mbar CO from 300 K to 120 K).

Figure 4-1 shows the Zr 3d, O 1s and C 1s XP spectra, LEED patterns and CO-TPD spectra of clean $Pt_3Zr(0001)$ alloy, of pristine ZrO_2/Pt_3Zr and of defective (soft sputtered) ZrO_2/Pt_3Zr. The Zr 3d spectrum of the clean alloy exhibits a doublet at 179.6 eV (Zr $3d_{5/2}$) and 182.0 eV (Zr $3d_{3/2}$), which is assigned to metallic Zr in the Pt_3Zr alloy.[16] The small amount of signal detected in the O 1s region can be attributed to the O dissolved in the substrate. Almost no signal is detected in the C 1s region. The LEED image shows both first-order and second-order diffraction spots. CO-TPD indicates CO desorption from Pt (terrace) atoms in the alloy (at 340 K), and from Pt atoms at defects/steps (at around 450 K). The peak at 140 K is an artefact resulting from CO desorbing from the Ta heating wires.

The Zr 3d spectrum of the pristine oxide shows two new species, accompanied by a decrease of the intensity of the $Zr_{substrate}$ signal. In chapter 3, we assigned the feature at a binding energy of 180.7 eV to the ZrO_2 trilayer film (O-Zr-O), and the signal at a binding energy of 182.5 eV to ZrO_2 clusters (size from 0.5 to 10 nm, area coverage approximately 10-15%). Also O 1s displays two features, at 529.9 eV (trilayer film) and 530.7 eV (ZrO_2 clusters). A slight decrease of the intensity in the Pt 4f region is observed, due to the attenuation of Pt signal by the ZrO_2 layer formed above. The LEED image exhibits two hexagonal patterns corresponding to two rotational domains of the oxide, as well as additional moiré spots caused by the double diffraction by the oxide and the substrate lattice. No CO desorption from Pt can be observed anymore, only CO weakly bonded to the oxide and desorbing at 155 K is observed (corresponding to a BE of 0.42 eV).

After soft sputtering, both the intensities and peak positions of the Zr 3d and O 1s species change. The peak positions of $Zr_{substrate}$, $Zr_{cluster}$, O_{film} and $O_{cluster}$ are shifted by around +0.2 eV. Furthermore, new species at binding energies of 181.9 eV (Zr_x) and 531.7 eV (OD/OH) are detected both in Zr 3d and O 1s regions. They are likely formed due to the dissociation of residual H_2O/D_2O on the oxygen vacancies (as discussed below). Compared to the pristine

oxide, the $Zr_{film}/Zr_{substrate}$ ratio decreased from 0.58 to 0.48 (assuming that the substrate signal does not change because about 5 layers are probed at a KE of 1300 eV). Upon sputtering, the total (film and cluster) $Zr:Zr_{substrate}$ ratio decreases from 0.83 to 0.78 whereas the total (film and cluster) $O:Zr_{substrate}$ ratio decreases from 0.85 to 0.74, suggesting a preferential removal of O atoms and the creation of oxygen vacancies. No change in the Pt 4f spectra can be registered.

The diffraction pattern characteristics of the thin oxide film also vanishes upon soft sputtering, indicating that the long range order of the well-defined thin oxide film is lost.[17] In the CO-TPD spectra, a desorption peak at ~ 175 K is observed, which is 20 K higher than the temperature of CO desorption from the pristine oxide. Such increase of the desorption temperature can be attributed to a more strongly bonded CO (adsorption energy of 0.46 eV; estimated by applying the Redhead equation, with a pre-exponential factor for desorption of 10^{13} s^{-1})[18] on the defects.[19] In addition, a tiny hump at around 450 K is observed on the defective oxide. Such feature has been previously assigned to CO desorption from Pt atoms at defects/steps. Although we cannot exclude the possibility that some Pt atoms are exposed to the surface after soft sputtering, their amount must be very small. It should be noted, that ion scattering spectroscopy was recently conducted in Prof. Michael Schmid´s group (our project partner) in order to study the defective film prepared by the similar procedure as ours. The results shows that 40% of the oxide is destroyed and that the Pt signal intensity increased significantly (up to 70% of clean alloy) upon Ar^+ sputtering. Such observation is not in agreement with our current results regarding the defective oxide (no change in Pt 4f region, and very little amount of CO desorption from Pt sites). Further experiments are planned to study the defective oxide in more detail.

4.3.2. D2O-TPD: high temperature desorption features

Figure 4-2 shows TPD spectra of D_2O after dosing at 190 K, with masses 20 (D_2O^+) and 4 (D_2^+) being monitored. According to XPS, the coverage of the ZrO_2 ultrathin film after dosing 20 L D_2O is 17.8. Upon 1st dosing (Figure 4-1 left), D_2O readily desorbs *molecularly* upon heating, as a pronounced peak of D_2O^+ is detected at 487 K. It corresponds to a desorption energy of $E_{TPD} \approx 1.3$ eV, estimated by applying the Redhead equation[18] (assuming a pre-exponential factor for desorption as 10^{13} s^{-1}). However, no D_2^+ signal was registered which would indicate D recombination and thus water dissociation. Upon repeated D_2O adsorption and desorption cycles, no significant changes were observed (Figure 4-2 right).

Somorjai and coworkers studied the adsorption of H_2O on ZrO_2 thin films (> 7 zirconia layers) prepared by physical vapor deposition (PVD) on a Pt(111) substrate.[14] At saturation, three H_2O peaks at 190, 275 and 370 K were observed in their work, and were assigned to different binding sites. H_2 desorption was also not observed for the pristine surface. It should be mentioned that PVD-prepared ZrO_2 often shows non-uniform thickness and is thus not homogenous.[20] This may explain why, in comparison to their work, only one D_2O desorption feature was observed for our well-defined ZrO_2 trilayer film.

At this point, we should also compare D_2O desorption from ZrO_2 thin films with that from other thin films. On ultrathin Al_2O_3 films, D_2O desorption was observed at 168 K.[21] On thin FeO films, D_2O desorption was observed at 169 K.[22] Therefore, the high temperature D_2O desorption can be either attributed to the strong bonding between D_2O molecules and Zr cation sites at the surface, or to the recombination of OD and D from D_2O dissociated on the surface. Recombinative desorption of water has been observed for several oxides, including both ideal and defective surfaces.[23,24] On ideal surfaces, such a process is often fully reversible.

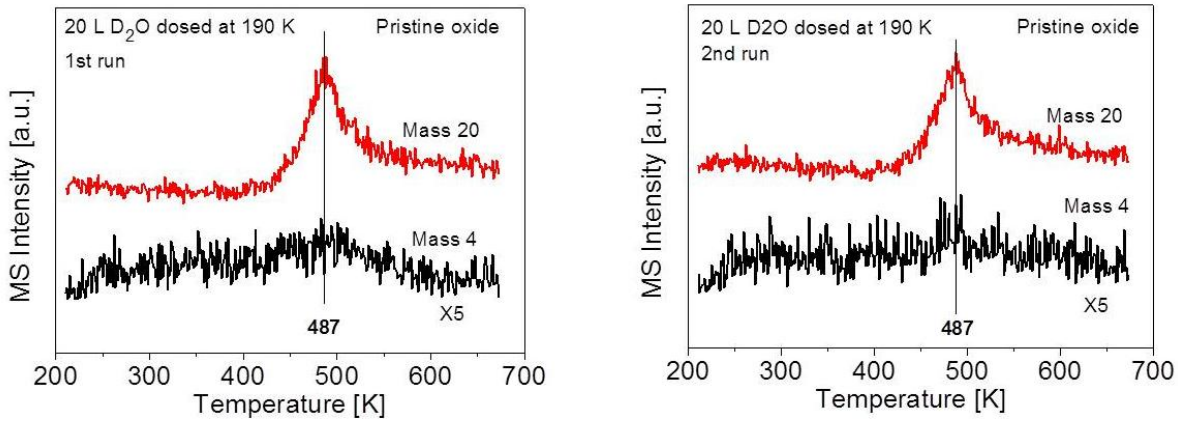

Figure 4-2. D_2O TPD of pristine ZrO_2/Pt_3Zr. D_2O was dosed at 190 K, and both Mass 20 (D_2O^+) and Mass 4 (D_2^+) were monitored. Left: 1st run. Right: 2nd run.

The defective oxide film was also examined via D_2O TPD, and the results are shown in Figure 4-3. For the 1st run, desorption signals both for D_2O and D_2 are detected at around 490 K. For the 2nd run, only D_2O desorption occurred at 487 K. Takeuchi et al. also studied the adsorption of H_2O on ZrO_2 thin films after ion bombardment.[14] In addition to H_2O desorption, they also initially observed H_2 desorption at 340 K, 420 K and 500 K. Upon repeated water adsorption and desorption cycles, the amount of H_2 decreased.

Qualitatively, our results of D_2O TPD on (defective) ultrathin ZrO_2 are in line with Somorjai´s results, although our film seems to be more homogeneous. We thus suggest that D_2O partially dissociates on the surface defects (oxygen vacancies) on the ZrO_2 film produced by "soft" Ar ion bombardment. However, the oxygen vacancies are quenched by water adsorption so that the second TPD runs become identical for pristine and (originally) defective ZrO_2. It should be noted that D_2O TPD of defective ZrO_2/Pt_3Zr should be repeated and double check in the future, as the desorption peak of D_2 has similar temperature maximum and shape as D_2O.

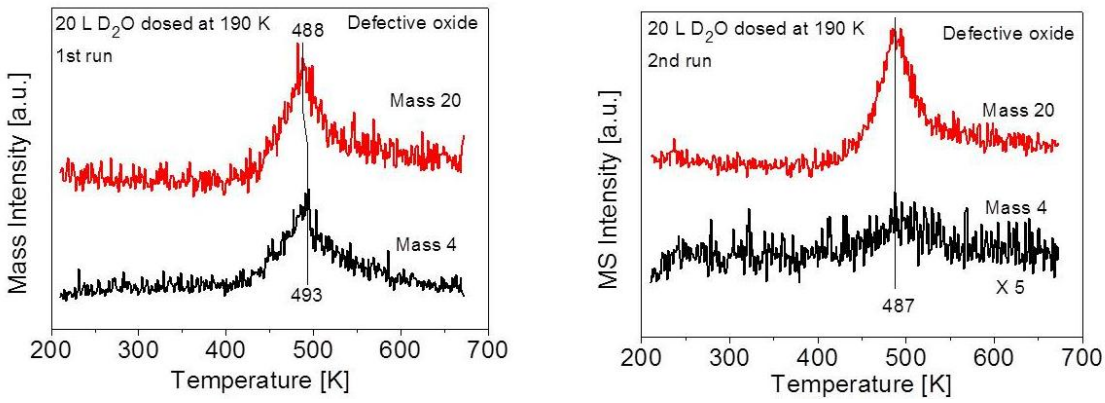

Figure 4-3. D_2O TPD of defective ZrO_2/Pt_3Zr. D_2O was dosed at 190 K, and both Mass 20 (D_2O^+) and Mass 4 (D_2^+) was monitored. Left: 1st run. Right: 2nd run.

4.3.3. XPS: molecularly and dissociatively adsorbed D_2O

The interaction between the pristine oxide and D_2O was also monitored by lab-based XPS, as shown in Figure 4-4. After dosing 20 L D_2O at 190 K, a new feature with a binding energy of 182.0 eV is observed in the Zr 3d region, whereas in the O 1s region two new species appear at 531.6 eV (1.9 eV higher than O_{film}) and 533.5 eV (3.6 eV higher than O_{film}). No significant changes in the Pt 4f and C 1s region are registered; the slight decrease of the Pt 4f signal intensity is due to the attenuation by the adsorbates. The O 1s binding energies of molecularly adsorbed water and of hydroxyl groups have been measured for various systems, and adsorbed H_2O usually appears at higher binding energies than OH. On α-Fe_2O_3(0001), molecularly adsorbed water appears at 533.2 eV (3.2 eV higher than the oxide peak), whereas hydroxyl groups appears at 531.5 eV (1.5 eV higher than the oxide peak).[25] On FeO(111) thin films, dosing water at 120 K and subsequently heating to 190 K reveals a feature attributed to molecularly adsorbed water at around 533.5 eV (3 eV higher than the oxide peak), and a feature attributed to hydroxyl group at around 531.5 eV (1 eV higher than the oxide peak).[26] DFT calculations by Redinger and coworkers show that molecularly adsorbed water and dissociated water (hydroxyls) have similar adsorption energies on Zr sites, and both of them may exist on the ultrathin ZrO_2 surface upon water adsorption. Final state core level shifts

calculations reveal that the molecularly adsorbed water has a shift of +4.6 eV relative to O_{film}, and hydroxyls have a shift of +1.7 eV. Thus, we attribute the 533.5 eV feature observed in our XP spectra to molecularly adsorbed D_2O, and the 531.6 eV feature to OD.

Ratios of the different Zr and O species relative to $Zr_{substrate}$ for both pristine oxide and oxide exposed to D_2O (at 190 K) are summarized in Table 4-1. Upon D_2O dosing, Zr_{film} to $Zr_{substrate}$ ratio decreases from 0.58 to 0.52, indicating the trilayer ZrO_2 film strongly interacts with D_2O/OD, and is partially converted to ZrO_x. O_{film} to $Zr_{substrate}$ ratio decreases from 0.59 to 0.56, suggesting part of O_{film} is covered by OD. Both $Zr_{cluster}/Zr_{substrate}$ and $O_{cluster}$ /$Zr_{substrate}$ slightly increase, mainly due to the attenuation of $Zr_{substrate}$ signal after D_2O dosing, indicating that the clusters are less affected than the trilayer film.

Table 4-1. Summary of different Zr and O species relative to $Zr_{substrate}$ ratios for both pristine oxide and oxide exposed to D_2O

	Zr_{film}:$Zr_{substrate}$	$Zr_{cluster}$:$Zr_{substrate}$	O_{film}:$Zr_{substrate}$	$O_{cluster}$:$Zr_{substrate}$
Pristine at 300 K	0.58	0.24	0.59	0.25
After dosing of D_2O at 190 K	0.52	0.26	0.56	0.27

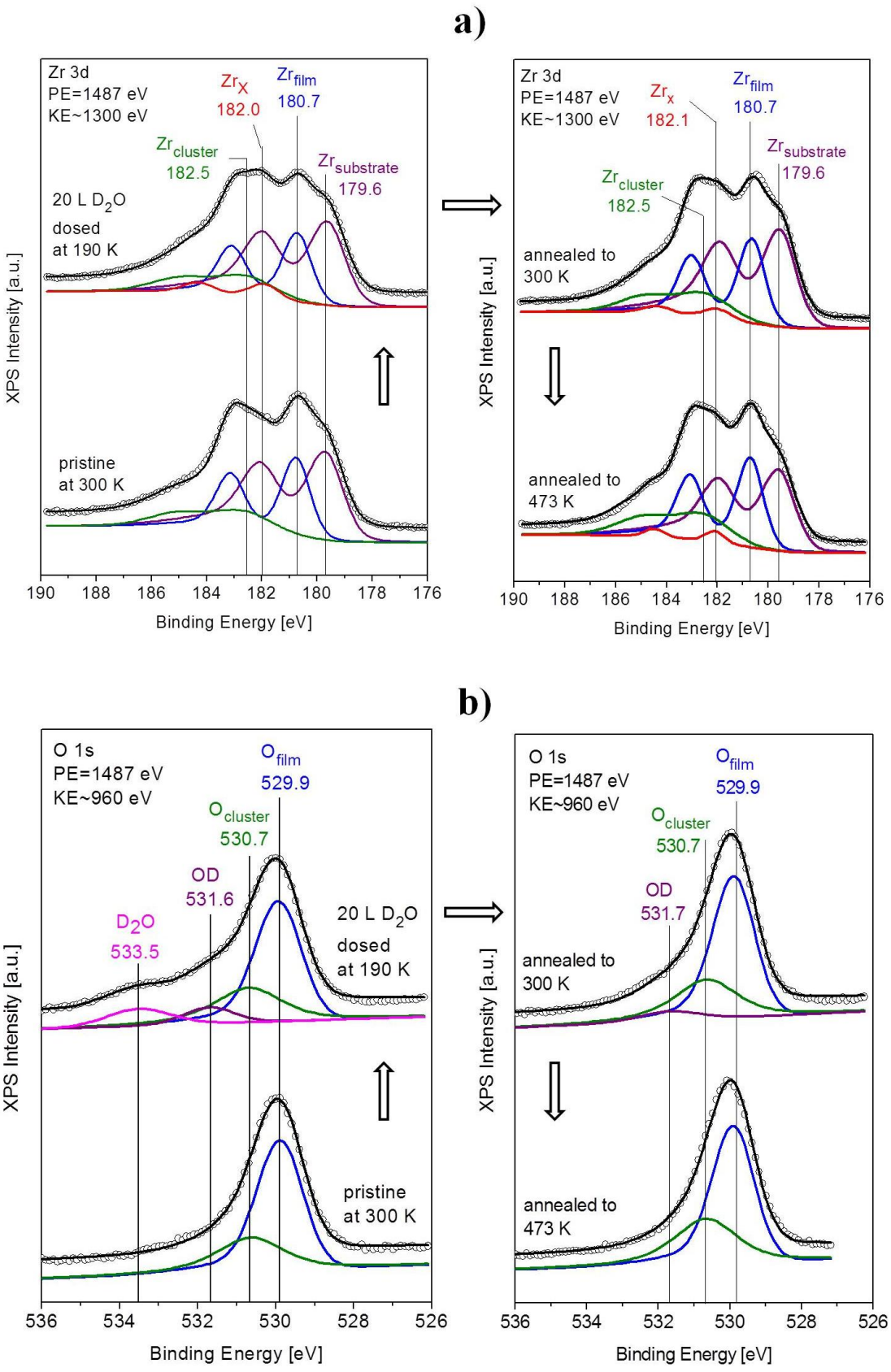
a)
Zr 3d
PE=1487 eV
KE~1300 eV
Zr_X
182.0
Zr_film
180.7
Zr_cluster
182.5
Zr_substrate
179.6
20 L D2O
dosed
at 190 K
pristine
at 300 K
XPS Intensity [a.u.]
190 188 186 184 182 180 178 176
Binding Energy [eV]
Zr 3d
PE=1487 eV
KE~1300 eV
Zr_x
182.1
Zr_film
180.7
Zr_substrate
179.6
Zr_cluster
182.5
annealed to
300 K
annealed to
473 K
XPS Intensity [a.u.]
190 188 186 184 182 180 178 176
Binding Energy [eV]
b)
O 1s
PE=1487 eV
KE~960 eV
O_film
529.9
O_cluster
530.7
OD
531.6
D2O
533.5
20 L D2O
dosed
at 190 K
pristine
at 300 K
XPS Intensity [a.u.]
536 534 532 530 528 526
Binding Energy [eV]
O 1s
PE=1487 eV
KE~960 eV
O_film
529.9
O_cluster
530.7
OD
531.7
annealed to
300 K
annealed to
473 K
XPS Intensity [a.u.]
536 534 532 530 528 526
Binding Energy [eV]

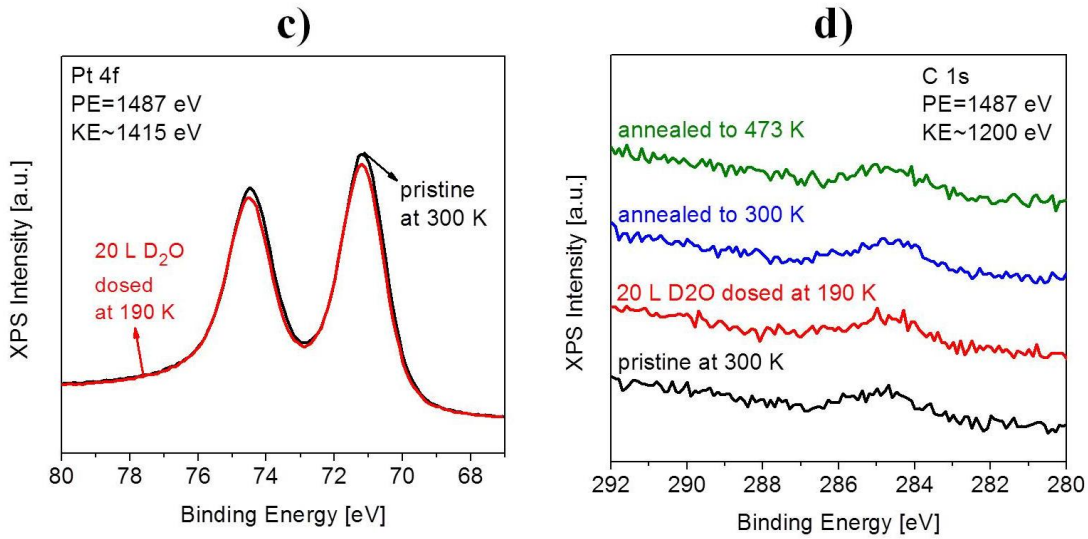

Figure 4-4. a) Zr 3d, b) O1s, c) Pt 4f and d) C 1s XP spectra of pristine oxide (spectra measured at 300 K), of the oxide dosed with 20 L D_2O at 190 K (spectra measured at 190 K), of the D_2O exposed oxide annealed to 300 K and 473 K for 5 min (spectra measured at 190 K, Pt 4f spectra are not shown). The arrows indicate the order of the experiments.

In order to further examine the two species of the O 1s region, we annealed the D_2O exposed sample to different temperatures for 5 min and measured XPS again after cooling back to 190 K. The XP spectra of the sample annealed to 300 K and 473 K are included in Figure 4-4. Figure 4-5 presents the ratios of OD/O_{film}, and D_2O/O_{film} for different annealing temperatures. The ratio D_2O/O_{film} is 17.1% after dosing 20 L D_2O at 190 K, and decreases very fast upon annealing to higher temperature. At 300 K, no signal from D_2O can be detected. In contrast, the ratio OD/O_{film} decreases more slowly, and the signal disappears only after annealing to 473 K. Thus, OD is more strongly bound to the oxide surface than D_2O. However, such observation is not in agreement with the TPD results, as TPD only shows one desorption feature, and the desorption occurs at higher temperature than the desorption temperature deduced by XPS. One way to explain the desorption at lower temperature observed by XPS is the so called photon-stimulated desorption.[27,28] Such process has been observed on both metal

and oxide sufaces,[29,30,31] if sufficient energy is transferred to the translational motion of adsorbates to overcome the activation barrier for desorption.[30]

For Zr 3d, after annealed to 473 K, a species (Zr_X) at a binding energy of 182.1 eV (Zr $3d_{3/2}$) is still observed, while D_2O/OD is completely desorbed from the surface. The Zr_{film} to $Zr_{substrate}$ ratio is 0.72, which is higher than the ratio of pristine oxide (0.58). One possible explanation is that some kind of non-recombinative desorption of dissociated D_2O also occurs (e.g. on defects sites). That is, D_2 is desorbed from the surface and O is left on the sample (the amount of D_2 is so small that it is not possible to detect it by TPD). And in this process the remaining O might diffuse through the Pt (mono- or bi-)layer beneath and bond to Zr atoms of the alloy substrate, and is forming another type of ZrO_x, thus the signal of $Zr_{substrate}$ is decreased.

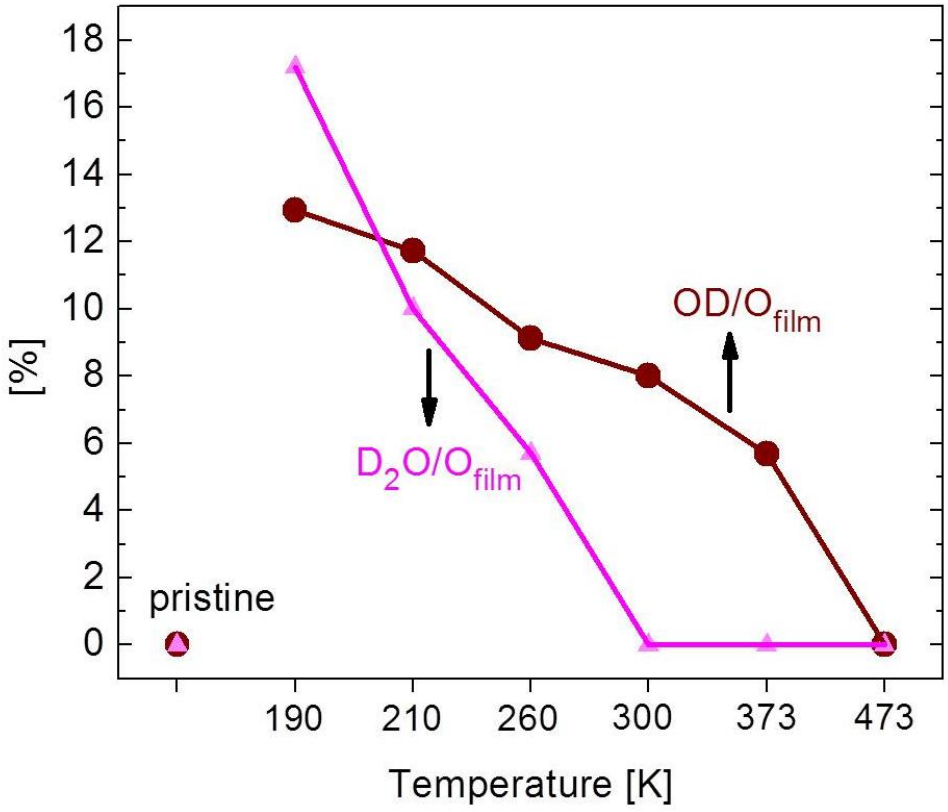

Figure 4-5. The ratios of D_2O /O_{film} and OD/O_{film} (from the peak area of O 1s XP spectra), in percentage for different annealing treatments.

Figure 4-6 shows the corresponding Zr 3d, O 1s Pt 4f and C 1s spectra for the defective (sputtered) oxide, in UHV, after dosing 20 L D_2O at 190 K, as well as after annealing to 300 and 473 K. As shown in section 4.3.1, already before water dosing defective oxide exhibits Zr_x in the Zr 3d region, and hydroxyl (OD or OH) in the O 1s region, due to the residual H_2O or D_2O . After D_2O exposure, both Zr_x and OD grow in intensity, and molecularly adsorbed D_2O is again observed at a binding energy of 532.8 eV. As shown in Table 4-2 Zr_{film} to $Zr_{substrate}$ ratio decreases from 0.48 to 0.38, indicating the trilayer ZrO_2 film is mostly affected by D_2O/OD adsorption. O_{film} to $Zr_{substrate}$ ratio decreases from 0.43 to 0.38, suggesting the conversion of O_{film} to OD. The increase of $Zr_{cluster}$ to $Zr_{substrate}$ and $O_{cluster}$ to $Zr_{substrate}$ ratios are due to the decreased intensity of $Zr_{substrate}$ signal caused by the D_2O/OD covered surface. Again, the Pt 4f signal is attenuated by the adsorbed OD/D_2O species.

Table 4-2. Summary of different species to $Zr_{substrate}$ ratios for both pristine oxide and oxide exposed to D_2O

	Zr_{film}:$Zr_{substrate}$	$Zr_{cluster}$:$Zr_{substrate}$	O_{film}:$Zr_{substrate}$	$O_{cluster}$:$Zr_{substrate}$
Defective at 300 K	0.48	0.30	0.43	0.31
After dosing of D_2O at 190 K	0.38	0.40	0.38	0.41

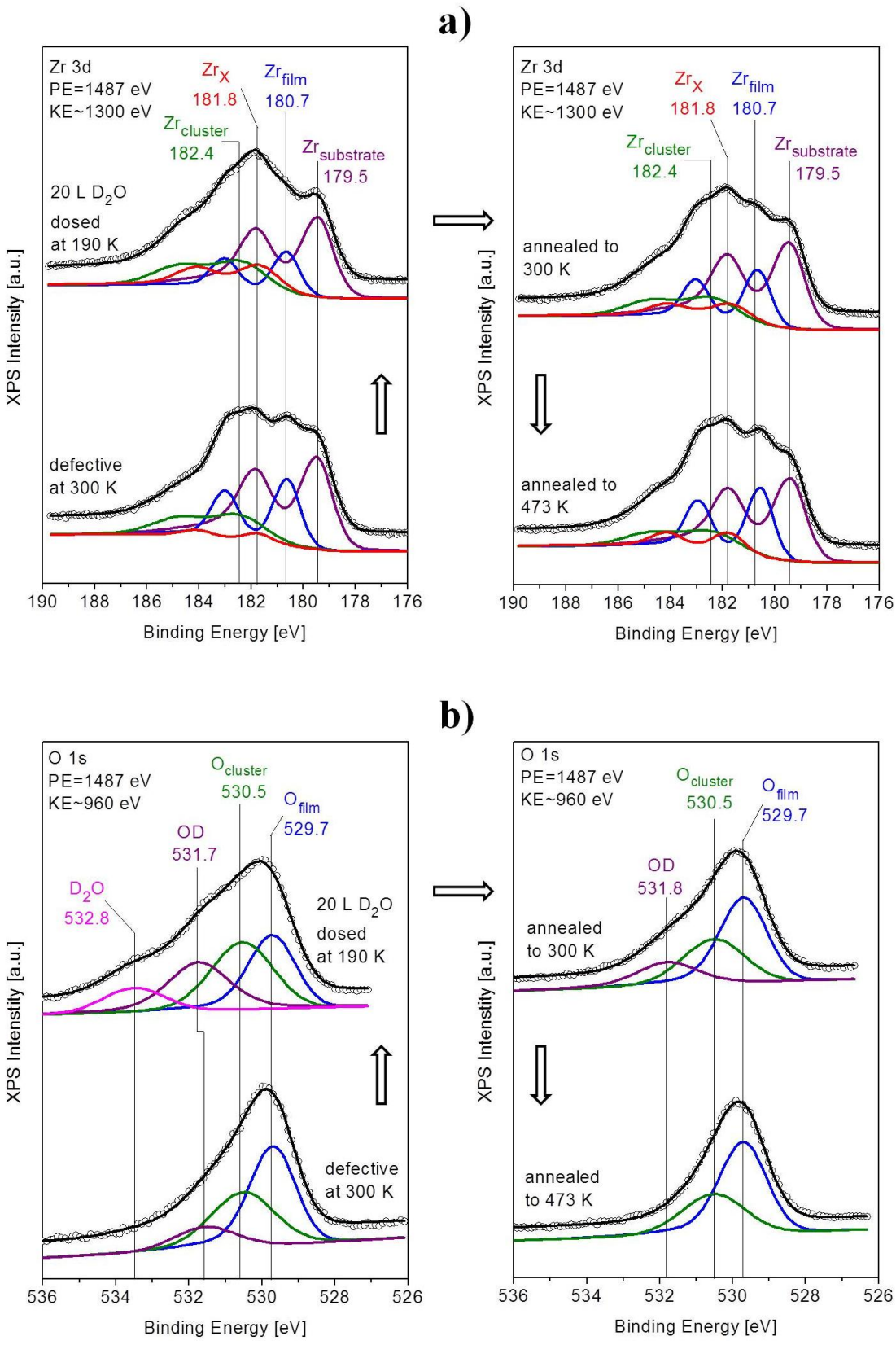
a)
Zr 3d
PE=1487 eV
KE~1300 eV
Zr_X
181.8
Zr_film
180.7
Zr_cluster
182.4
Zr_substrate
179.5
20 L D2O
dosed
at 190 K
defective
at 300 K
annealed to
300 K
annealed to
473 K
XPS Intensity [a.u.]
Binding Energy [eV]
b)
O 1s
PE=1487 eV
KE~960 eV
O_cluster
530.5
O_film
529.7
OD
531.7
D2O
532.8
20 L D2O
dosed
at 190 K
defective
at 300 K
OD
531.8
annealed
to 300 K
annealed
to 473 K
XPS Intenstity [a.u.]
Binding Energy [eV]

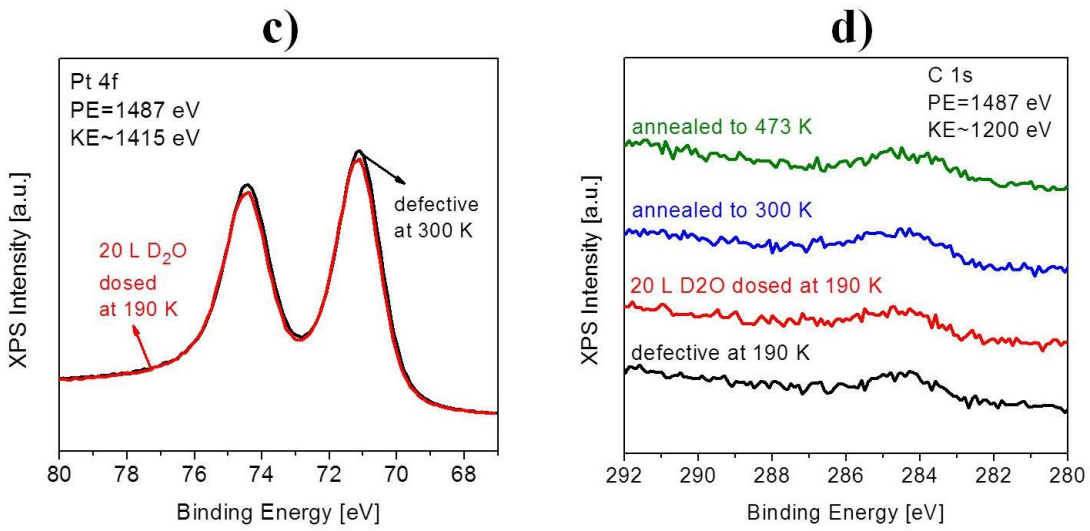

Figure 4-6. a) Zr 3d, b) O1s, c) Pt 4f and d) C 1s XP spectra of defective oxide (spectra measured at 300 K), of the oxide dosed with 20 L D_2O at 190 K (spectra measured at 190 K), of the D2O exposed oxide annealed to 300 K and 473 K for 5 min (spectra measured at 190 K, Pt 4f spectra are not shown). The arrows indicate the order of the spectra.

Figure 4-7 displays, for the sputtered oxide, the ratios of OD/O_{film} and D_2O/O_{film} for different annealing temperatures. Again, OD is more strongly bonded to the surface, as it desorbs only at 473 K. Contrary to the recombinative desorption of OD species as the major pathway for pristine oxide, we suggest that the non-recombinative desorption is the main pathway for defective oxide. After annealing to 473 K the Zr_{film} to $Zr_{substrate}$ ratio is 0.55, which is higher than the ratio for defective oxide, indicating the quenching of defects and the increase of the Zr_{film} signal. In such a quenching process D_2 is released (as shown by TPD), and O is bonded to the defective Zr_{film}, forming a coordinately saturated ZrO_2. It should be also noted that Zr_x can still be detected after annealing the sample to 473 K. Again, O atoms formed from the non-recombinative desorption might migrate to the substrate, bond there to Zr atoms and form a ZrO_x species.

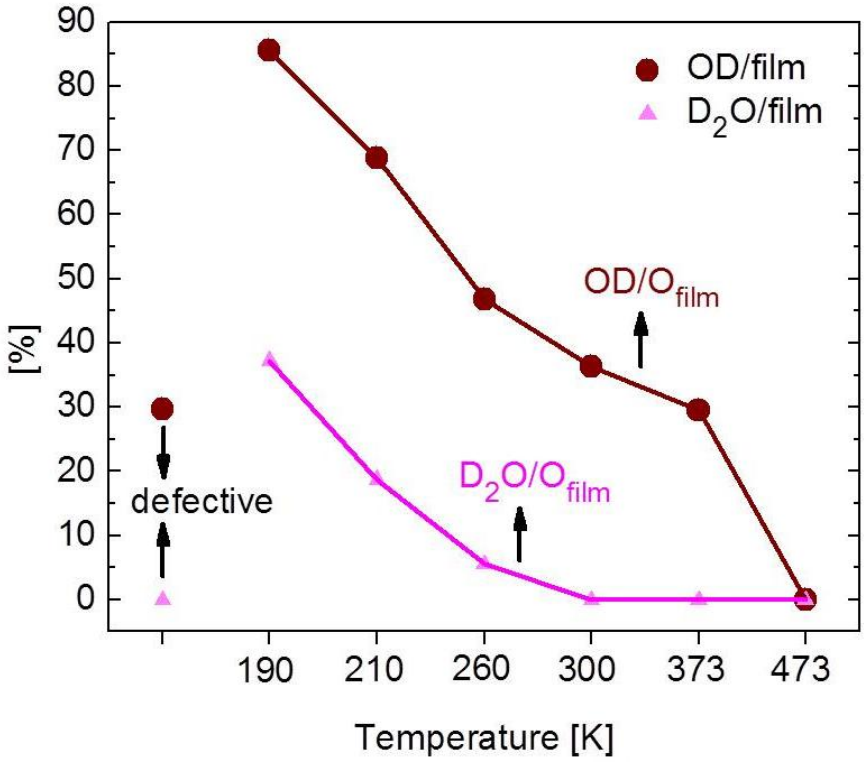

Figure 4-7. The ratio of D_2O /O_{film}, and OD /O_{film} (from the peak area of O 1s XP spectra) for different treatments.

To summarize, D_2O undergoes different pathways when interacting with ultrathin ZrO_2 films. For pristine oxide, it can adsorb and desorb as molecule (see pathway 1), or adsorb dissociatively and form hydroxyls, and desorb recombinatively as molecule (see pathway 2)

Pathway 1: $D_2O_{(g)} \rightarrow D_2O_{(a)} \rightarrow D_2O_{(g)}$

Pathway 2: $D_2O_{(g)} \rightarrow D_2O_{(a)} \rightarrow OD + D \rightarrow D_2O_{(g)}$

For defective oxide a third pathway, which is non-recombinative desorption, occurs on the defects. The remaining O atoms after the D2 desorption fill the O vacancies.

Pathway 3: $D_2O_{(g)} \rightarrow D_2O_{(a)} \rightarrow OD + D \rightarrow D_{2(g)} + O$

4.3.4. IRAS

For further characterization of the different surface species, infrared spectroscopy was applied. Figure 4-8 displays the IRAS spectra of the pristine ZrO_2 film exposed to 20 L D_2O at 190 K, as well as of the D_2O exposed ZrO_2 film heated to the indicated temperatures. At

190 K, an adsorption band with a peak centered around 2530 cm^{-1} was observed (with a FWHM of 120 cm^{-1}). Upon increasing the annealing temperature, a red shift of the peak position occurred, while the intensity remained approximately constant. After annealing to 473 K, the adsorption band had vanished, as expected from the TPD desorption temperature.

A peak centered at 2530 cm^{-1} can be either assigned to amorphous solid water (ice) as shown in the literature,[21,32] to D_2O molecules bounded to the surface,[32,11] or to hydrogen bonded OD.[33] Ice would also exhibit a sharp feature at a wavelength above 2700 cm^{-1} corresponding to the dangling OD bonds at the surface of ice islands, which is not observed in our spectra. Also our spectra were taken at 190 K, which is too high for the ice formation. Thus, we attribute the feature observed at around 2530 cm^{-1} to molecular D_2O and hydrogen bonded OD adsorbed on the ZrO_2 ultrathin film.

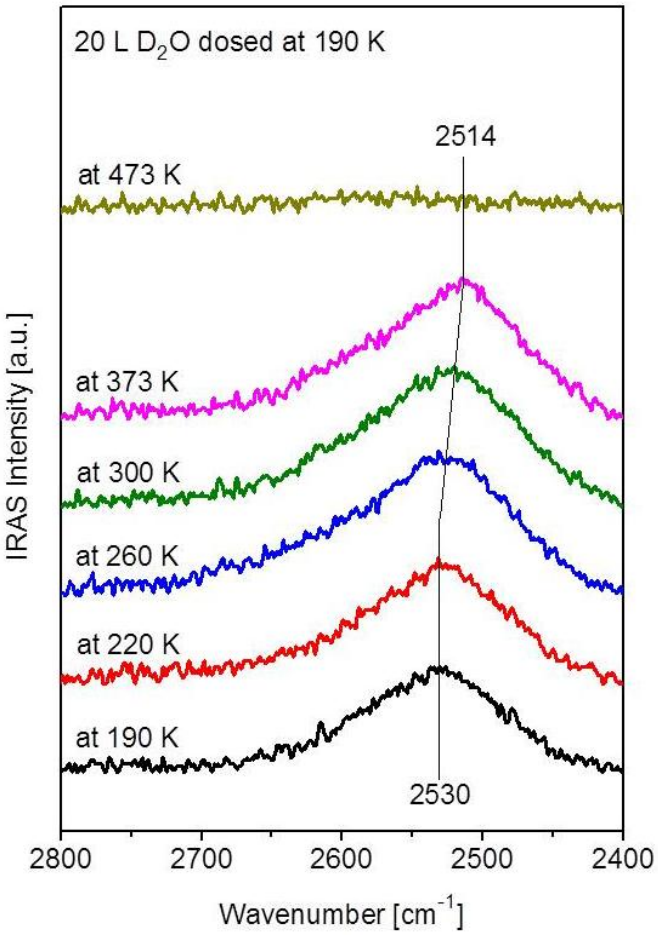

Figure 4-8. IRAS spectra for D_2O adsorption on pristine $ZrO_2/Pt_3Zr(0001)$ (20 L D_2O dosed at 190 K), and annealing of the D_2O exposed sample to the indicated temperatures (spectra measured at 190 K).

Figure 4-9 displays the IR spectra of the defective ZrO_2 film after dosing 20 L D_2O at 190 K, as well as after annealing the exposed sample to the indicated temperatures. After D_2O was dosed at 190 K, a broad adsorption band with a peak around 2536 cm^{-1} was observed (with a FWHM of 120 cm^{-1}). We again assign this broad feature to molecular D_2O and hydrogen bonded OD adsorbed on ZrO_2 ultrathin film. When compared to pristine film, the IR spectra of defective film upon D_2O dosing and subsequent annealing do not show any significant difference.

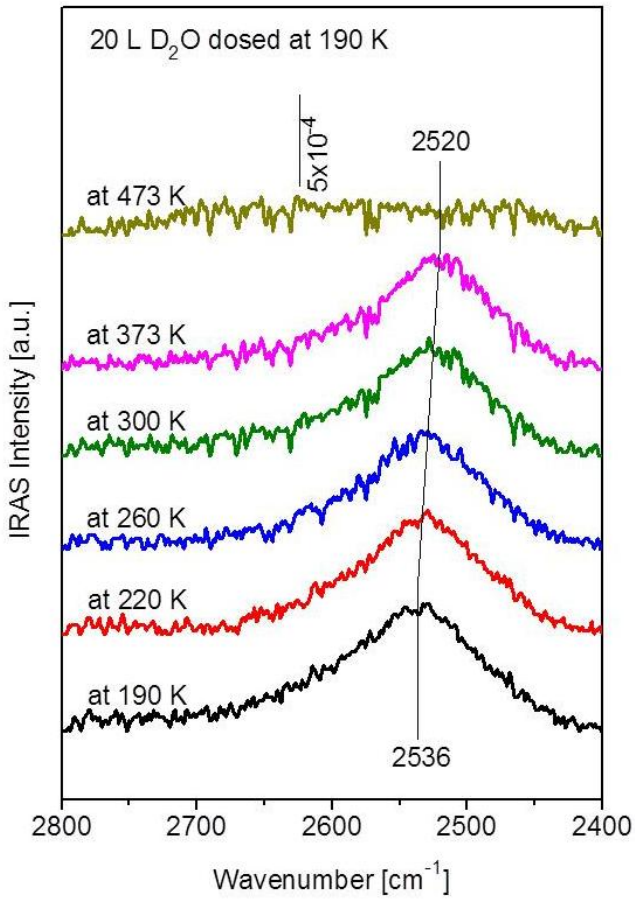

Figure 4-9. IRAS spectra of D_2O adsorption on defective $ZrO_2/Pt_3Zr(0001)$ (20 L D_2O dosed at 190 K), and annealing of the D_2O exposed sample to the indicated temperatures (spectra measured at 190 K).

4.3.5. NAP-XPS: dissociation of x-ray induced desorption

In order to examine the effect of elevated gas pressure, the room temperature interaction of water with the pristine ZrO_2 thin film was also examined by NAP-XPS (Figure. 4-10).

To properly fit the O 1s spectra for pristine oxide, a very weak component at 532.4 eV was included. Most likely, this is due to minute amounts of O dissolved in the subsurface. OH groups or H_2O would be positioned at different binding energies. C 1s did not indicate any carbon so that (adventitious) C-O containing species can be excluded. In any case, this feature was extremely weak. This component was also included in the fitting for O1s spectra of oxide in 1×10^{-6} mbar and 1×10^{-3} mbar H_2O.

In a background of 1×10^{-6} mbar H_2O, additional (low intensity) components are observed both in the Zr 3d and O 1s regions. In the Zr 3d spectra, Zr_x appears at a binding energy of 181.9 eV ($Zr3d_{3/2}$). In the O 1s region, a feature at a binding energy of 531.7 eV is observed, which is assigned to OH on Zr atoms. No signal corresponding to molecularly adsorbed H_2O is detected. The OH to O_{film} ratio is 0.08, which is considerably lower than the saturation coverage (0.15 ML) estimated by STM (20 L H_2O at 300 K, experiments done by M. Schmid and coworkers). This difference again points to the photon induced desorption. In $1x10^{-3}$ mbar H_2O, the signal of Zr_{film} is strongly dampened, and molecularly adsorbed H_2O appears at a binding energy of 533.7 eV. Both Zr_x and OH components grow in intensity, and shift -0.3 eV to the lower binding energy side. A similar shift is also observed for $Zr_{cluster}$, whereas the binding energies of both Zr_{film} and $Zr_{substrate}$ remain the same. It is known that at elevated pressure the gas phase can compensate the core level shift of materials with poor conductivity (i.e. reduce the charging effect).[34] Considering that ZrO_2 clusters show a large band gap (like an insulator), the observed shift of $Zr_{cluster}$ might be due to the compensating effect of the gas phase (the binding energy of $O_{cluster}$ is also shifted by -0.2 eV in 1×10^{-3} mbar H_2O). Potential

C contamination was also detected in 1×10^{-3} mbar H_2O, thus it is necessary to correct the contribution from oxygen-containing C species (C-O and O=C-C) in the O 1s XP spectra, as the O 1s peaks of C-related species are close to those of OH. We obtained the relative sensitivity factor of C 1s to O 1s by measuring the O 1s: C 1s peak intensity ratio of gas phase CO_2. The OH to O_{film} ratio is then calculated as 0.44, which is higher than for the pristine oxide exposed to 20 L D_2O at 190 K (0.17).

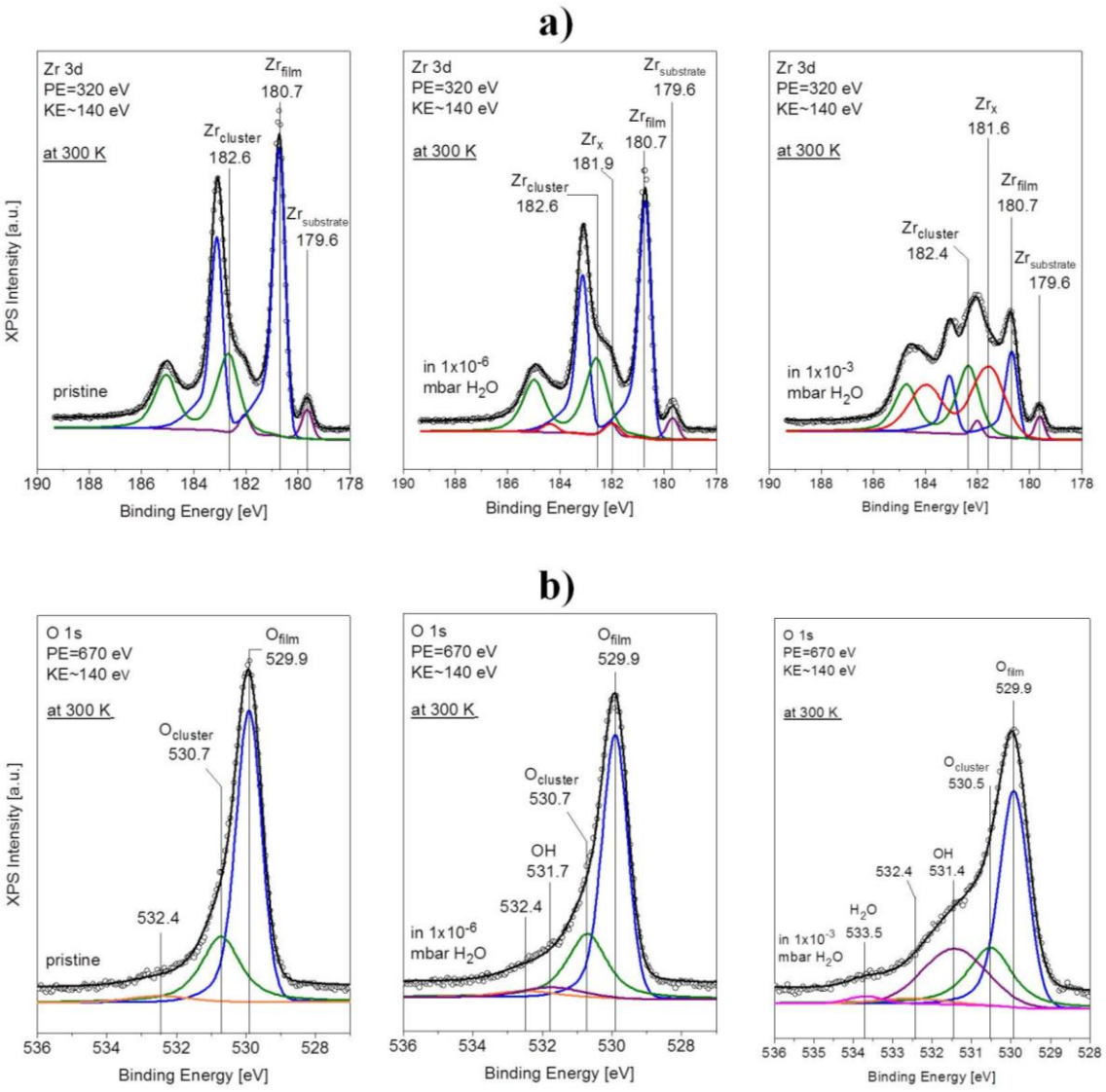

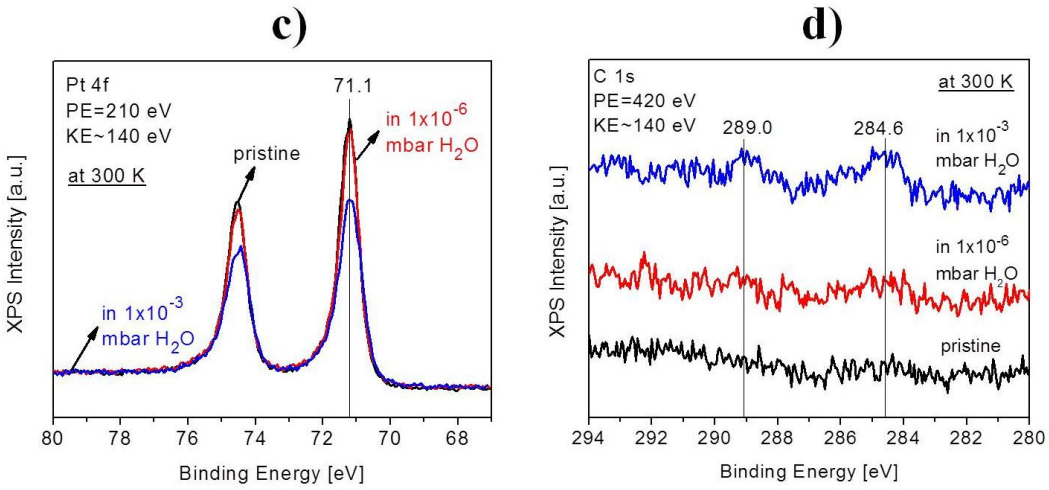

Figure 4-10. a) Zr 3d, b) O 1s c) Pt 4f and d) C 1s photoemission spectra of pristine oxide at 300 K and the indicated H_2O pressures. The lowest trace is the XP spectrum of clean pristine oxide.

4.4. Summary

The interaction of D_2O or H_2O with the ultrathin ZrO_2 film (both pristine and defective) was examined using TPD, (NAP-)XPS and IRAS.

XPS shows that D_2O adsorbs both molecularly (at a binding energy at +3.6 eV relative to O_{film}) and dissociatively (at a binding energy at +1.7 eV relative to O_{film}) at 190 K on pristine oxide. TPD exhibits a single desorption feature of D_2O molecules at 487 K, which is attributed to the desorption of molecularly adsorbed D_2O and the recombinative desorption of dissociated D_2O. IRAS confirms that both molecularly adsorbed D_2O and dissociated D_2O leave the surface above 473 K. More water dissociation occurs when the pristine oxide is subjected to elevated pressure (1×10^{-3} mbar) at room temperature but X-ray induced effects occur.

On defective oxide, D_2O also adsorbs both molecularly and dissociatively, as shown by XPS. TPD exhibits both D_2O and D_2 desorption, indicating that D_2O dissociated on the defects quenches the defects. , and.

Bibiliography

1. Lavalley, J. C.; Bensitel, M.; Gallas, J. P.; Lamotte, J.; Busca, G.; Lorenzelli, V., FT-IR study of the δ(OH) mode of surface hydroxy groups on metal oxides. *Journal of Molecular Structure* **1988,** *175* (0), 453-458.

2. Graf, P. O.; de Vlieger, D. J. M.; Mojet, B. L.; Lefferts, L., New insights in reactivity of hydroxyl groups in water gas shift reaction on Pt/ZrO_2. *Journal of Catalysis* **2009,** *262* (2), 181-187.

3. Fottinger, K.; Schlogl, R.; Rupprechter, G., The mechanism of carbonate formation on $Pd\text{-}Al_2O_3$ catalysts. *Chemical Communications* **2008,** (3), 320-322.

4. Moreau, F.; Bond, G. C.; Taylor, A. O., Gold on titania catalysts for the oxidation of carbon monoxide: control of pH during preparation with various gold contents. *Journal of Catalysis* **2005,** *231* (1), 105-114.

5. Qian, K.; Fang, J.; Huang, W.; He, B.; Jiang, Z.; Ma, Y.; Wei, S., Understanding the deposition–precipitation process for the preparation of supported Au catalysts. *Journal of Molecular Catalysis A: Chemical* **2010,** *320* (1–2), 97-105.

6. Brown, M. A.; Fujimori, Y.; Ringleb, F.; Shao, X.; Stavale, F.; Nilius, N.; Sterrer, M.; Freund, H.-J., Oxidation of Au by Surface OH: Nucleation and Electronic Structure of Gold on Hydroxylated MgO(001). *Journal of the American Chemical Society* **2011,** *133* (27), 10668-10676.

7. Heemeier, M.; Frank, M.; Libuda, J.; Wolter, K.; Kuhlenbeck, H.; Bäumer, M.; Freund, H. J., The influence of OH groups on the growth of rhodium on alumina: a model study. *Catal Lett* **2000,** *68* (1-2), 19-24.

8. Cappus, D.; Xu, C.; Ehrlich, D.; Dillmann, B.; Ventrice Jr, C. A.; Al Shamery, K.; Kuhlenbeck, H.; Freund, H. J., Hydroxyl groups on oxide surfaces: NiO(100), NiO(111) and Cr_2O_3(111). *Chemical Physics* **1993,** *177* (2), 533-546.

9. Hugenschmidt, M. B.; Gamble, L.; Campbell, C. T., The interaction of H_2O with a TiO_2(110) surface. *Surface Science* **1994,** *302* (3), 329-340.

10. Shavorskiy, A.; Müller, K.; Newberg, J. T.; Starr, D. E.; Bluhm, H., Hydroxylation of Ultrathin Al2O3/NiAl(110) Films at Environmental Humidity. *The Journal of Physical Chemistry C* **2014**.

11. Argon, P. A. A.; Fuller, E. L.; Jr; Holmes, H. F., IR Studies of Water Sorption on ZrO_2 Polymorphs. *Journal of Colloid and Interface Science* **1975,** *52* (3), 553-561.

12. Jacob, K.-H.; Knozinger, E.; Benier, S., Adsorption sites on polymorphic zirconia. *Journal of Materials Chemistry* **1993,** *3* (6), 651-657.

13. Merle-Méjean, T.; Barberis, P.; Othmane, S. B.; Nardou, F.; Quintard, P. E., Chemical forms of hydroxyls on/in Zirconia: An FT-IR study. *Journal of the European Ceramic Society* **1998,** *18* (11), 1579-1586.

14. Takeuchi, K.; Perry, S. S.; Salmeron, M.; Somorjai, G. A., The bonding properties of hydrogenated and fluorinated molecules to zirconium oxide thin films: influence of surface defects and water coadsorption. *Surface Science* **1995,** *323* (1-2), 30-38.

15. Maurice, V.; Takeuchi, K.; Salmeron, M.; Somorjai, G. a., The bonding of diethyl ether, ethanol and their fluorinated analogs to zirconium oxide thin films. *Surface Science* **1991,** *250* (1-3), 99-111.

16. Li, H.; Choi, J.-I. J.; Mayr-Schmölzer, W.; Weilach, C.; Rameshan, C.; Mittendorfer, F.; Redinger, J.; Schmid, M.; Rupprechter, G., Growth of an Ultrathin Zirconia Film on Pt_3Zr Examined by High-Resolution X-ray Photoelectron Spectroscopy, Temperature-Programmed

Desorption, Scanning Tunneling Microscopy, and Density Functional Theory. *The Journal of Physical Chemistry C* **2014,** *119* (5), 2462-2470.

17. Weilach, C.; Spiel, C.; Föttinger, K.; Rupprechter, G., Carbonate formation on Al2O3 thin film model catalyst supports. *Surface Science* **2011,** *605* (15–16), 1503-1509.

18. P.A.Redhead, Thermal Desorption of Gases. *VACUUM* **1962,** *12* (4), 203-211.

19. Kim, Y. D.; Stultz, J.; Goodman, D. W., Identification of Defect Sites on MgO(100) Surfaces. *Langmuir* **2002,** *18* (10), 3999-4004.

20. Maurice, V.; Salmeron, M.; Somorjai, G. A., The epitaxial growth of zirconium on Pt (111) single crystal surfaces. *Surface Science* **1990,** *237*, 116-126.

21. Yi, C. W.; Szanyi, J., D_2O Adsorption on an Ultrathin Alumina Film on NiAl(110). *Journal of Physical Chemistry C* **2007,** *111* (47), 17597-17602.

22. Daschbach, J. L.; Dohnálek, Z.; Liu, S.-R.; Smith, R. S.; Kay, B. D., Water Adsorption, Desorption, and Clustering on FeO(111). *The Journal of Physical Chemistry B* **2005,** *109* (20), 10362-10370.

23. Thiel, P. A.; Madey, T. E., The interaction of water with solid surfaces: Fundamental aspects. *Surface Science Reports* **1987,** *7* (6–8), 211-385.

24. Henderson, M. A.; London, A.; York, N.; Paris, O.; Tokyo, S., The interaction of water with solid surfaces : fundamental aspects revisited. *Surface Science Reports* **2002,** *46*, 1-308.

25. Yamamoto, S.; Kendelewicz, O. T.; Newberg, J. T.; Ketteler, G.; Starr, D. E.; Mysak, E. R.; Andersson, K. J.; Ogasawara, H.; Bluhm, H.; Salmeron, M.; Brown, G. E.; Nilsson, A., Water Adsorption on α-Fe_2O_3(0001) at near Ambient Conditions. *Journal of Physical Chemistry C* **2010,** *114*, 2256-2266.

26. Cappus, D.; Haßel, M.; Neuhaus, E.; Heber, M.; Rohr, F.; Freund, H. J., Polar surfaces of oxides: reactivity and reconstruction. *Surface Science* **1995,** *337* (3), 268-277.

27. Stockbauer, R.; Hanson, D. M.; Flodström, S. A.; Bertel, E.; Madey, T. E., Photon stimulated desorption of ions: A new probe of surface bonding and structure. *International Journal of Mass Spectrometry and Ion Physics* **1983,** *47* (0), 51-54.

28. Ageev, V. N., Desorption induced by electronic transitions. *Progress in Surface Science* **1994,** *47* (1–2), 55-203.

29. Zimmermann, F. M.; Ho, W., State resolved studies of photochemical dynamics at surfaces. *Surface Science Reports* **1995,** *22* (4–6), 127-247.

30. Drachsel, W.; Teutsch, T., Photon-induced field desorption of NO from Rh. *Surface and Interface Analysis* **2007,** *39* (2-3), 95-101.

31. Al-Shamery, K., Dynamics of photoinduced reactions at oxide surfaces. *Applied Physics A* **1996,** *63* (6), 509-521.

32. Leist, U.; Ranke, W.; Al-Shamery, K., Water adsorption and growth of ice on epitaxial Fe_3O_4(111), FeO(111) and Fe_2O_3(biphase). *Physical Chemistry Chemical Physics* **2003,** *5* (11), 2435-2441.

33. Carrasco, E.; Brown, M. a.; Sterrer, M.; Freund, H.-J.; Kwapien, K.; Sierka, M.; Sauer, J., Thickness-Dependent Hydroxylation of MgO(001) Thin Films. *The Journal of Physical Chemistry C* **2010,** *114* (42), 18207-18214.

34. Ogletree, D.; Bluhm, H.; Lebedev, G.; Fadley, C; Hussain Z; Salmeron, N., A Differentially Pumped Electrostatic Lens System for Photoemission Studies in the Millibar Range. Review of Scientific Instruments **2002,** 73 (11), 3872-3877.

5. CO_2 and H_2O (co)Adsorption on a ZrO_2 Thin Film

5.1. Introduction

The utilization of CO_2 as carbon source becomes more and more attractive from both an environmental and economical perspective. However, CO_2 is a very stable molecule, thus to induce a reaction the activation of CO_2 by a catalyst is required.[1] One way of activating CO_2 is dry reforming of methane (DRM), where CH_4 is reformed by CO_2 on Ni or Pt particles supported by zirconia, producing CO and H2 (synthesis gas). During DRM, CO_2 is reduced to CO via reaction precursors or intermediates, the released O can oxidize the carbon formed via CH_4 dissociation. Such activation can occur on ZrO_2 or on metal-oxide interfacial sites.[2] As a support, technical ZrO_2 powder material can activate CO_2 by forming carbonates with basic anionic sites, or by forming formate with hydroxyl groups.[2] However, due to the possible different reaction pathways, microscopic mechanisms of the functions of ZrO_2 need to be further examined via a surface science approach. Therefore, a systematic study of the interaction between CO_2 and a pristine ZrO_2 ultra-thin film (CO_2 adsorption on ZrO_2), as well as the interaction between CO_2 and a hydroxylated ZrO_2 ultra-thin film (CO_2 and H_2O co-adsorption and reaction) was carried out.

5.2. Experimental

The procedure for preparing the ultrathin ZrO_2 trilayer has been described in detail in chapter 3. The measurements below were performed in three separate UHV systems. XPS was utilized in all systems to confirm identical sample preparation. The TPD and IRAS experiments were conducted using the Vienna setup, which is described in detail in Chapter 2.

TPD spectra were collected by a differentially-pumped MKS eVision+ quadrupole mass spectrometer, and temperature ramping was performed by a Eurotherm 3216 PID controller, with a heating rate of 60 K/min. For IRAS experiments, CO_2, D_2O, HCOOH and HCHO were dosed via leak valves, and spectra were collected at grazing incidence on a Bruker IFS66v/S spectrometer with a liquid nitrogen-cooled MCT detector. All spectra were obtained by averaging 2048 interferograms with a spectral resolution of 4 cm^{-1}.

The synchrotron-based in situ (NAP-)XPS measurements were performed using the MAX Lab Lund setup. The detailed description of the machine can be found in Chapters 2 and Chapter 3. H_2O and CO_2 were dosed into the high pressure cell via the same leak valve, and a UHV T-piece was used to connect H_2O and CO_2 bottles as well as the leak valves.

The lab-based in situ XPS measurements were performed using the Novosibirsk (NSK) setup, which has been described in detail elsewhere,[3,4] and shortly also in Chapter 2. It consists of three main chambers with a base pressure of 1×10^{-9} mbar. The sample was prepared in the left chamber, then it was transferred into the reaction cell located inside the analyzer chamber for the XPS measurements. The analyzer chamber, X-ray anode and the energy analyzer were differentially pumped. All XP spectra were taken by using a non-monochromatized Al Kα X-ray source. CO_2 and H_2O were dosed into the high pressure cell via two separate valves.

5.3. Results and discussion

5.3.1. CO_2 TPD

CO_2 desorption has been studied by TPD on a variety of oxide surfaces. On a ZnO(0001) surface low exposures (<0.75 L) lead to a peak at 180 K. Further increase of exposure results in the development of a second feature at 125 K. The former is assigned to more strongly adsorbed CO_2 on defect sites, whereas the latter is assigned to weakly adsorbed CO_2 on

pristine sites.[6,7] On the $SrTiO_3$(100) surface, CO_2 features a main desorption peak at a temperature of 132 K, which grows in intensity with increasing exposure up to 1 L.[5] The weakly bonded CO_2 was also observed on the ZrO_2 ultrathin film. Figure 5-1 shows a dosage series of CO_2 TPD spectra. At 0.2 L exposure, only one species at 117 K is observed. The peak intensity increases when the exposure is increased to 0.5 L and 1 L, and stays the same when the exposure further increases to 2 L. No shift of the peak maximum is registered for different exposures. The desorption feature at 117 K can be assigned to CO_2 physisorbed on the surface of the ZrO_2 ultrathin film. The adsorption energy was also estimated by applying the Redhead equation.[8] A pre-exponential factor for desorption of 10^{13} s^{-1} was used. The desorption maximum at a temperature of 117 K corresponds to a desorption energy of $E_{TPD} \approx$ 0.30 eV, which is in agreement of the usual value of E_{TPD} of physisorbed CO_2 (0.3-0.5 eV) on oxides.[7]

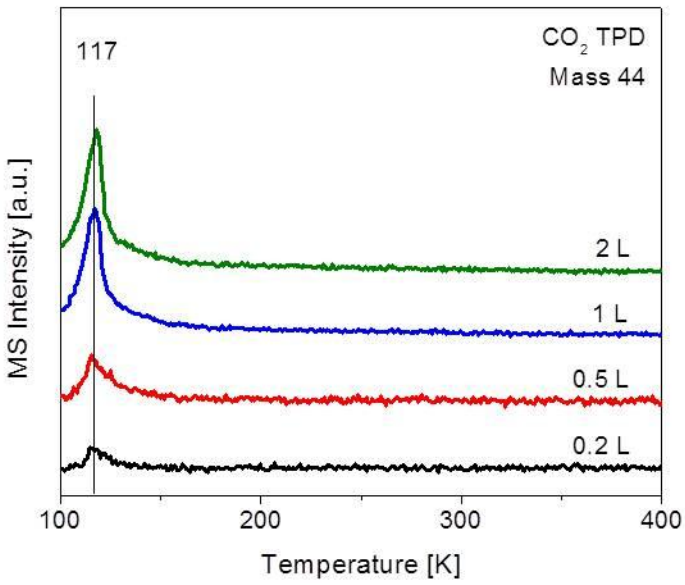

Figure 5-1. CO_2-TPD spectra for a ZrO_2 ultrathin film (0.2 L, 0.5 L, 1 L and 2 L CO_2, dosed at 90 K)

5.3.2. Synchrotron-based in situ NAP-XPS measurements of CO_2 adsorption

TPD results clearly show the weak interaction between CO_2 and ZrO_2 under UHV conditions. In order to examine this system at catalytically more relevant conditions, a pressure dependent CO_2 adsorption experiment (from 1×10^{-6} mbar to 1×10^{-1} mbar) was performed at room temperature, while simultaneously examining the Zr 3d and C 1s core level region by synchrotron based (in situ) NAP-XPS (Lund setup). Both Zr 3d and C 1s spectra are included in Figure 5-2. The lowest traces are the XP spectra of the pristine oxide. As shown in previous chapters, two species exists on the surface, namely the ZrO_2 ultrathin film (at a binding energy of 180.8 eV) and ZrO_2 clusters (at a binding energy of 182.4 eV). The small component (purple) at a binding energy of 179.6 eV is the signal of the Zr from the substrate. No signal could be detected in the C 1s region. When the oxide is exposed to CO_2 (in the pressure range from 1×10^{-6} mbar to 1×10^{-3} mbar) at room temperature, no change in the Zr 3d and C 1s region is detected. However, when the pressure of CO_2 is further increased to 1×10^{-1} mbar, a new species in the Zr 3d spectrum at a binding energy of 182.8 eV is observed. The corresponding C 1s spectrum also exhibits various C related species at different binding energies, as shown in Figure 5-2 (right). According to literature, the feature at a binding energy of 284.6 eV is usually assigned to adventitious elementary carbon.[9] The species at binding energies of 285.5 eV and 286.5 eV might be attributed to H_x-C-O (x=0-3) species.[10,11] For the feature at a binding energy of 289.5 eV the chemical state of the carbon is usually O-C=O and possible candidates are carboxyls, formate and carbonates.[12 13,14] It should be noted that the intensity of the Zr 3d signal is greatly dampened in 1×10^{-1} mbar CO_2, which is caused by the attenuation of photoelectrons by both gas phase and by the formed adsorbate layers of C-related species. The Zr_{film} to $Zr_{substrate}$ ratio is 12.3 for pristine oxide, and it decreases to 7.6

in the presence of 1×10^{-1} mbar CO_2. Thus, the ZrO_2 ultrathin film is partially converted into a new species, named Zr_x.

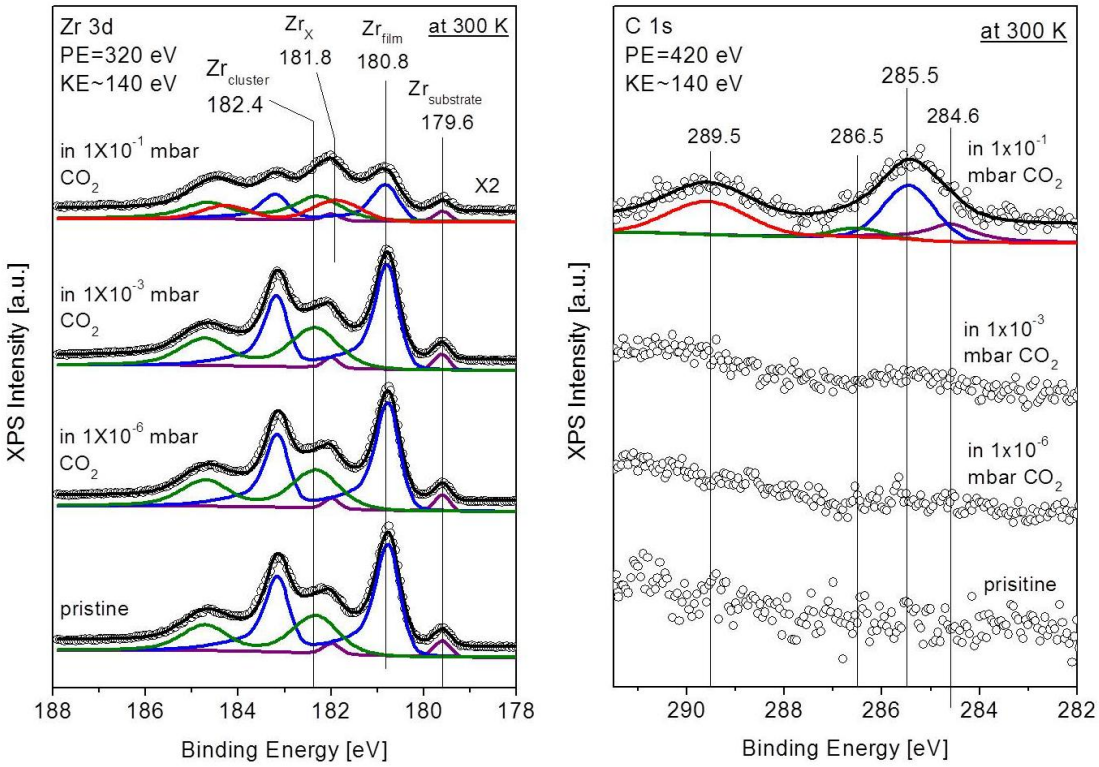

Figure 5-2. Zr 3d (left) and C 1s (right) spectra of pristine oxide recorded at indicated CO_2 pressure. The lowest trace is the XP spectrum of pristine oxide. (spectra taken at 300 K, kinetic energy of photoelectrons ≈ 140 eV).

However, due to the fact that at Max Lab Lund the leak valve for CO_2 dosing was previously used for dosing H_2O, it was suspected that the origin of the different C-related species (H_x-C-O and O-C=O) at 1×10^{-1} mbar CO_2 could be related to residual H_2O in the gas line. Thus, additional experiments were performed in the NSK setup.

5.3.3. Lab-based in situ NAP-XPS measurement of CO_2 adsorption, and CO_2 and H_2O co-adsorption

In order to exclude any effect of water traces and to systematically study the effect of co-dosed H_2O on the CO_2 adsorption on the oxide, two sets of experiments were performed in the NSK setup. . The ZrO_2 ultrathin film was first exposed to clean CO_2 in order to confirm the experimental results obtained in the Lund setup, as shown in Figure 5-3. The distance between sample and X-ray anode was very short, so that the sample temperature was343 K instead of 300 K (the sample temperature during the Lund measurements). In addition, 3×10^{-2} mbar was chosen as the highest pressure in order to ensure a sufficient signal to noise ratio with reasonable measurement time. It can be shown that no C-related species are formed in the presence of pure CO_2 under these conditions (up to 3×10^{-2} mbar), as displayed in Figure 5-3.

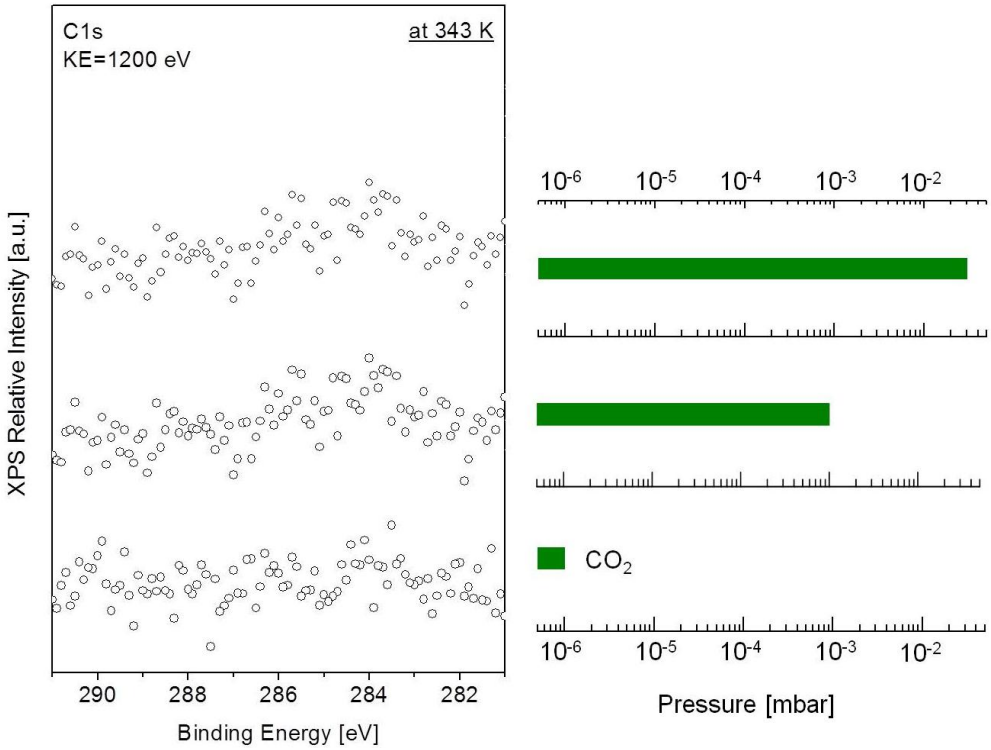

Figure 5-3. C 1s (left) spectra of pristine ZrO_2 at indicated CO_2 pressure (right). The raw data were normalized to a clean sample (spectra taken at 343 K, kinetic energy of photoelectrons ≈ 1200 eV).

Thereafter, a freshly prepared ZrO_2 ultrathin film was subjected to CO_2 and H_2O co-exposure with different CO_2/H_2O ratios. When changing from 1st to 2nd mixture, the H_2O pressure increased whereas the CO_2 pressure was kept constant. When changing from 2nd to 3rd mixture, the CO_2 pressure increased whereas the H_2O pressure was kept constant, and so forth. The measured XP spectra are shown in Figure 5-4. In 1×10^{-6} mbar CO_2 and 1×10^{-6} mbar H_2O (1st mixture), two species are observed at binding energies of 284.4 eV and 286.4 eV. As mentioned above, the former is assigned to adventitious elementary carbon, and the latter is assigned to H_xC-O species. When the pressure of H_2O increases to 3×10^{-4} mbar (2nd mixture), no significant change is registered. Nevertheless, when CO_2 pressure reaches 7×10^{-4} mbar (3rd mixture), a feature appears at a binding energy of 285.5 eV (another H_xC-O species). As the CO_2 pressure further increases to 3×10^{-2} mbar (4th mixture), a new species at a binding energy of 288.3 eV (O-C=O) is observed. When H_2O pressure finally increases to 3×10^{-3} mbar (5th mixture), no more new feature is detected. However, the intensity of the signal of H_xC-O species increases. It should be mentioned that water is important for the activation of CO_2, but the intensity of the different species (e.g. 285.5 eV and 288.3 eV) is stronger influenced by the pressure of CO_2.

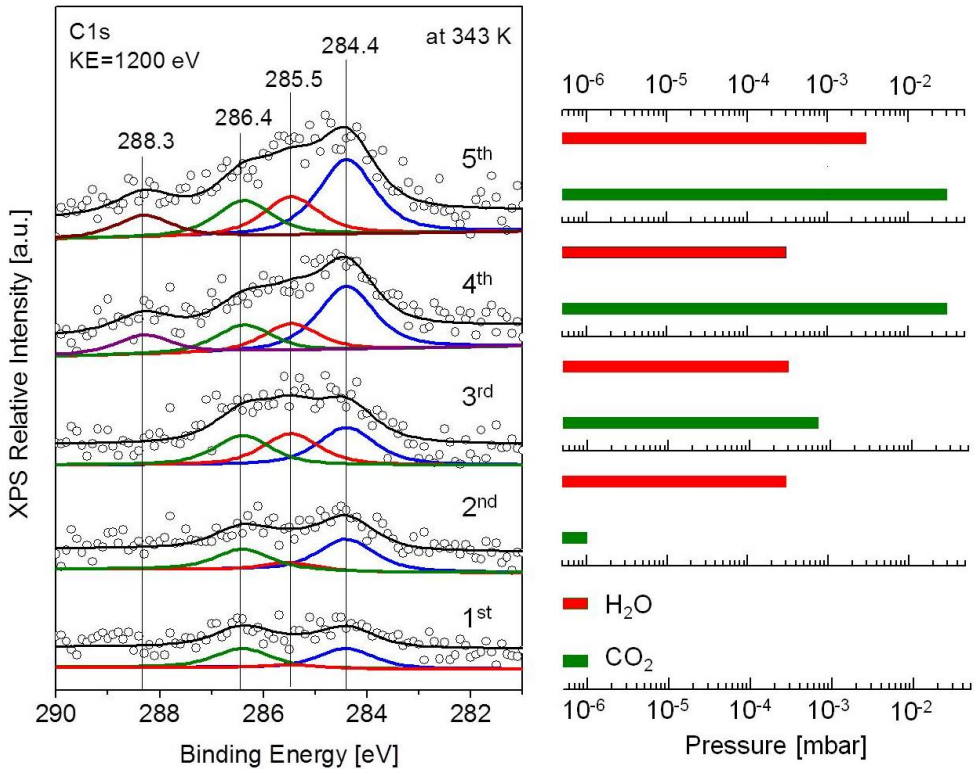

Figure 5-4. C 1s (left) spectra of pristine ZrO_2 in CO_2 and H_2O mixture at indicated pressures (right). The raw data were normalized to a clean sample (spectra taken at 343 K, kinetic energy of photoelectrons ≈ 1200 eV).

.

The Zr 3d region was also monitored during the experiment, and the results are shown in Figure 5-5. In presence of the 5th mixture (3×10^{-3} mbar CO_2 and 3×10^{-2} mbar H_2O), a new species Zr_x is detected at a binding energy of 182.7 eV. Compared with the pristine oxide, the ratio $Zr_{film}/Zr_{substrate}$ decreases from 0.44 to 0.36, whereas the ratio $Zr_{cluster}/Zr_{substrate}$ remains the same. The ratio $(Zr_{film}+Zr_x)/ Zr_{substrate}$ is 0.45, which is similar to the ratio $Zr_{film}/Zr_{substrate}$ of the pristine oxide, indicating that the carbon related species are formed on Zr_{film}, and Zr_{film} is partially converted to Zr_x due to the adsorption.

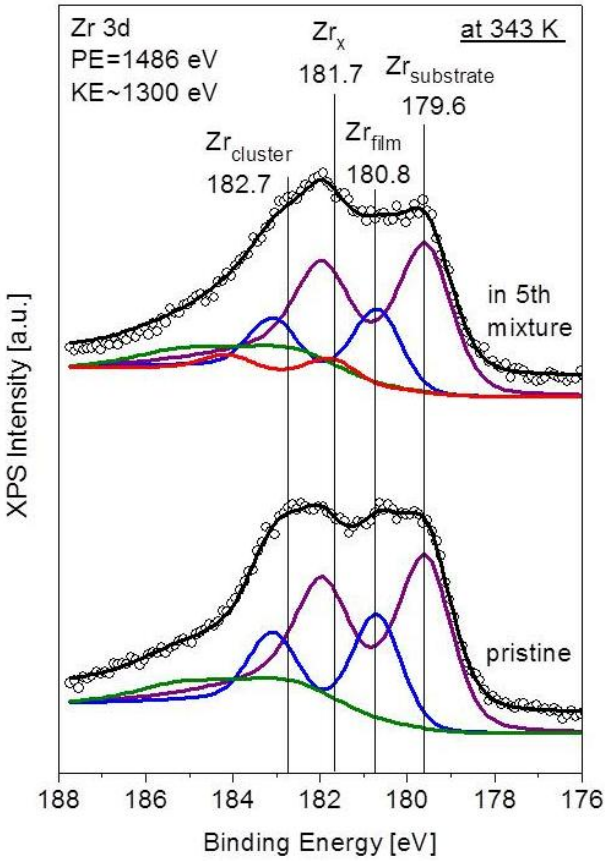

Figure 5-5. Zr 3d spectra of pristine ZrO_2 measured in UHV and in 3×10^{-3} mbar CO_2 plus 3×10^{-2} mbar H_2O (5^{th} mixture). (spectra taken at 343 K, kinetic energy of photoelectrons ≈ 1300 eV).

We have also investigated the thermal stabilities of the formed C-related species. As shown in Figure 5-6, the signal of the 288.6 eV species (O-C=O) completely disappeared when the sample is heated to 423 K in 3×10^{-2} mbar CO_2 and 3×10^{-3} mbar H_2O (5^{th} mixture), and the intensity of H_x-C-O signal decreases. At 523 K, almost no signal of H_x-C-O is detected. When the sample was afterwards cooled down in the reaction mixture to 343 K, we can again observe the reversible formation of H_x-C-O and O-C=O species on the surface, and their signal decreases in intensity upon evacuation.

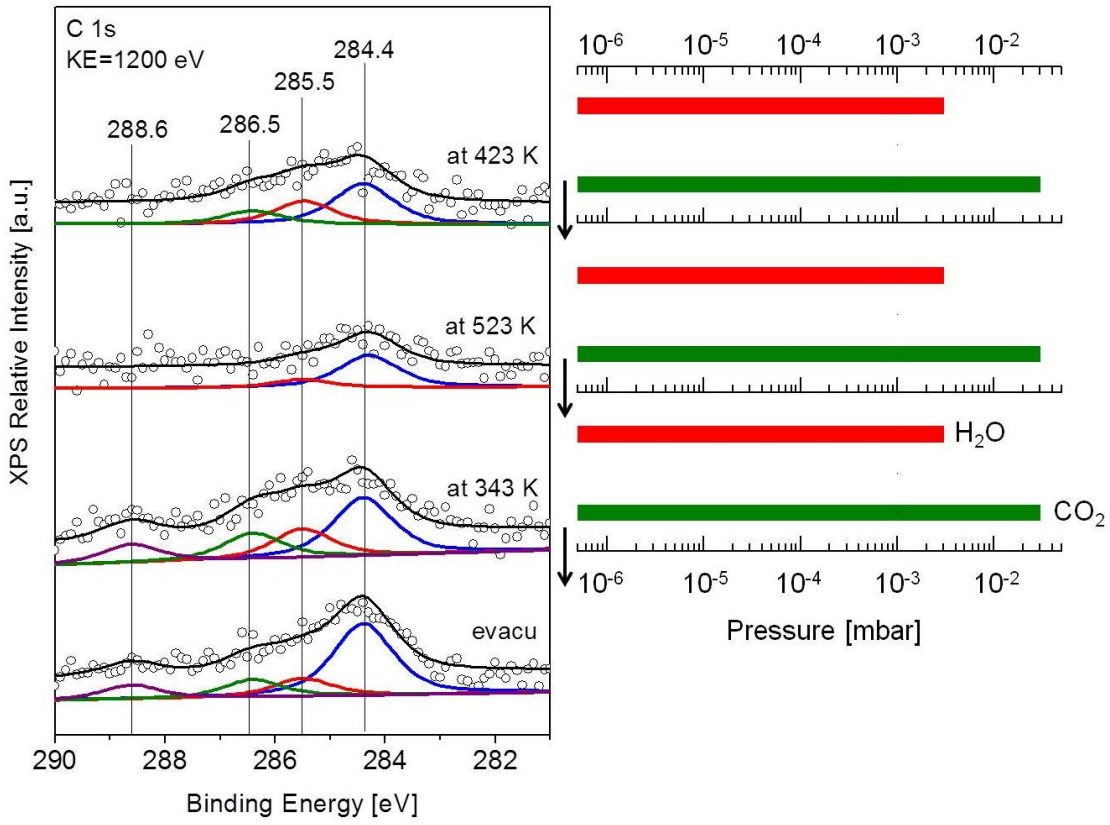

Figure 5-6. C 1s spectra of pristine oxide in 3×10^{-2} mbar CO_2 plus 3×10^{-3} mbar H_2O (5^{th} mixture) at different temperatures and after evacuation. Spectra were taken when the sample temperature was kept in CO_2 and H_2O mixture at 423 K and 523 K, and at 343 K after cooling down in the same gas mixture. The lowest panel was acquired after the evacuation. The raw data were normalized to a clean sample (spectra taken at 343 K, kinetic energy of photoelectrons≈ 1200 eV).

It is worth comparing the binding energies of the newly formed species in the C 1s and Zr 3d region obtained from different experiments. The results are summarized in Table 1. Clearly, clean CO_2 does not interact with the ultrathin ZrO_2 film at 343 K which is in agreement with the TPD results. On the other hand, both dosing "presumably water contaminated" CO_2 (Max Lab Lund experiment) and co-dosing of CO_2 and H_2O (NSK experiment) lead to formation of new species at similar binding energies in the C 1s and Zr 3d region, thus confirming our suspicions of water traces.

Table 5-1. Summary of binding energies of newly formed species in the C 1s and Zr 3d region for the different CO_2 and H_2O experiments

	C related species in C 1s, eV				Zr_x in Zr 3d, eV
Lund (1×10^{-1} mbar CO_2) including H_2O traces	284.6	285.5	286.5	289.5	181.8
NSK (in 3×10^{-2} mbar CO_2)	×	×	×	×	×
NSK (in 3×10^{-2} mbar CO_2 and 3×10^{-3} mbar H_2O)	284.4	285.5	286.5	288.3	181.7

5.3.4. IRAS measurements of HCOOH and HCHO adsorption

In order to assign the H_x-C-O and O-C=O species more precisely, IRAS spectra were acquired, because the expected surface species have different functional groups with exhibit different absorption frequencies. In order to obtain reference data, HCOOH and HCHO were chosen as testing molecules, as they have different vibrational modes: CH, CH_2, O-C-O and C=O. Figure 5-7 shows the IRAS spectrum of HCOOH adsorption on the ZrO_2 thin film. In 1×10^{-6} mbar HCOOH two absorption bands were detected at 1593 cm^{-1} and 1395 cm^{-1}, which is the typical wavenumber splitting (~200 cm^{-1}) of ν(OCO) of bridge bonded bidentate formate (HCOO).[15] Thus, the former band is assigned to ν_{as}(OCO) and the latter is assigned to ν_s(OCO). δ(CH) was not observed because it may overlap with ν_s(OCO).[16]

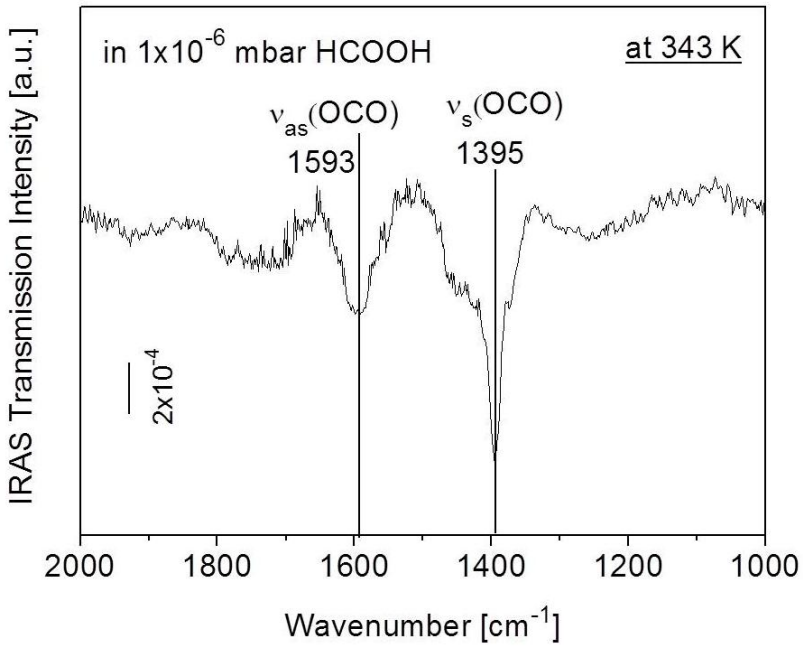

Figure 5-7. IRAS spectra of HCOOH adsorption on a ZrO_2 thin film, spectra taken in presence of 1×10^{-6} mbar HCOOH at 343 K.

Figure 5-8 shows the IRAS spectra of HCHO adsorption on the ZrO_2 thin film. In 1×10^{-6} mbar HCHO absorption features at 1785, 1610, 1395 and 1251 cm^{-1} can be observed. With reference to published results, they are assigned to ν(C=O) modes of physisorbed HCHO, ν(C=O), w(CH_2) and r(CH_2) modes of chemisorbed HCHO, respectively.[17,16] The ν(C=O) mode has a red shift relative to the value reported for solid formaldehyde (1740 cm^{-1}), indicating that the chemisorbed HCHO molecule is bonded to the cationic Zr site through the O end.[17] The observed wavenumbers for the formate ion and molecular formaldehyde are summarized in Table 5-2.

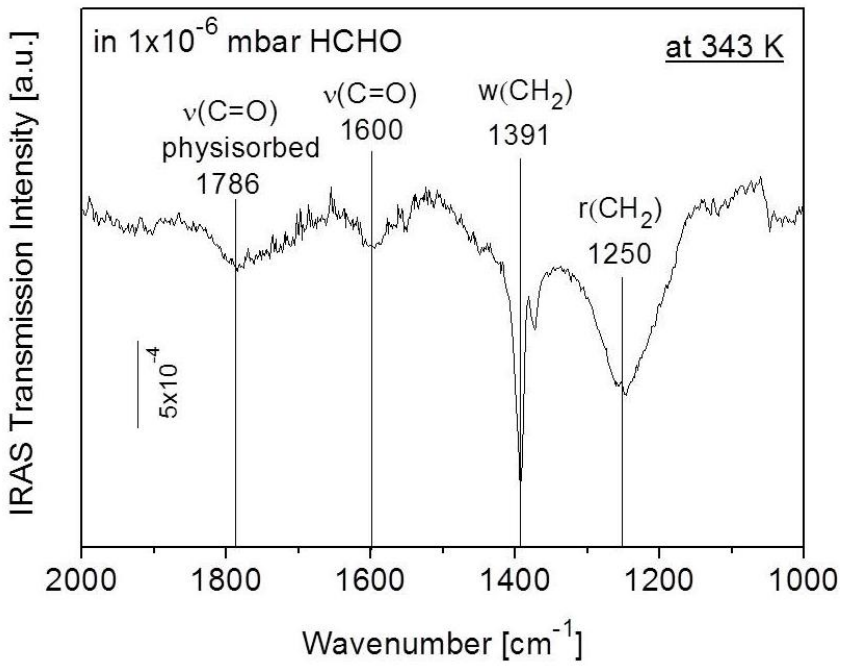

Figure 5-8. IRAS spectra of HCHO adsorption on the ZrO_2 thin film. Spectra taken in presence of 1×10^{-6} mbar HCHO at 343 K.

Table 5-2. Observed wavenumbers of the formate ion and molecular formaldehyde

	ν_s(OCO)	ν_{as}(OCO)	δ(CH)	ν (C=O)	w(CH_2)	r(CH_2)
Wavenumber (cm^{-1})	1395	1593	~1395	1600	1391	1250

5.3.5. IRAS measurements of CO_2 and H_2O co-adsorption

Figure 5-9 shows IRAS spectra acquired during the **C**O_2 and H_2O co-adsorption experiments. The pressure conditions for the IRAS experiments were the same as for the NSK in-situ XPS measurements. Due to technical limitations, the 4th reaction mixture could not be used in the Vienna setup for IRAS experiments. When the ZrO_2 thin film is subjected to a exposure of 1×10^{-6} mbar CO_2 and 1×10^{-6} mbar H_2O (1st mixture), a band at 1265 cm^{-1} is observed, which can be assigned to r(CH_2) mode (see Table 5-2). When the pressure of H_2O is increased to 3×10^{-4} mbar (2nd mixture), the band of r(CH_2) mode increases in intensity. When the H_2O

pressure is increased to 3×10^{-4} mbar, pronounced features at 1383 cm^{-1} and 1455 cm^{-1} are detected, which are typical adsorption bands for $w(CH_2)$ and $\delta(CH_2)$ (see Table 5-2).[16] When the pressure of CO_2 is increased to 7×10^{-4} mbar (3rd mixture), no change is observed. Finally, when the pressure of H_2O and CO_2 increase to 3×10^{-3} mbar and 3×10^{-2} mbar (5th mixture), strong absorption bands at 1735 cm^{-1} and 1290 cm^{-1} appear, which are assigned to ν(C=O) and ν(C-OH) vibrational modes of COOH.[18] Typical vibrational modes of ν(OCO) indicating the formation of formate are not observed for this experiment. Thus, H_x-C-O and O-C=O species detected by in-situ XPS can be attributed to surface bound H_2-C-O and COOH, respectively.

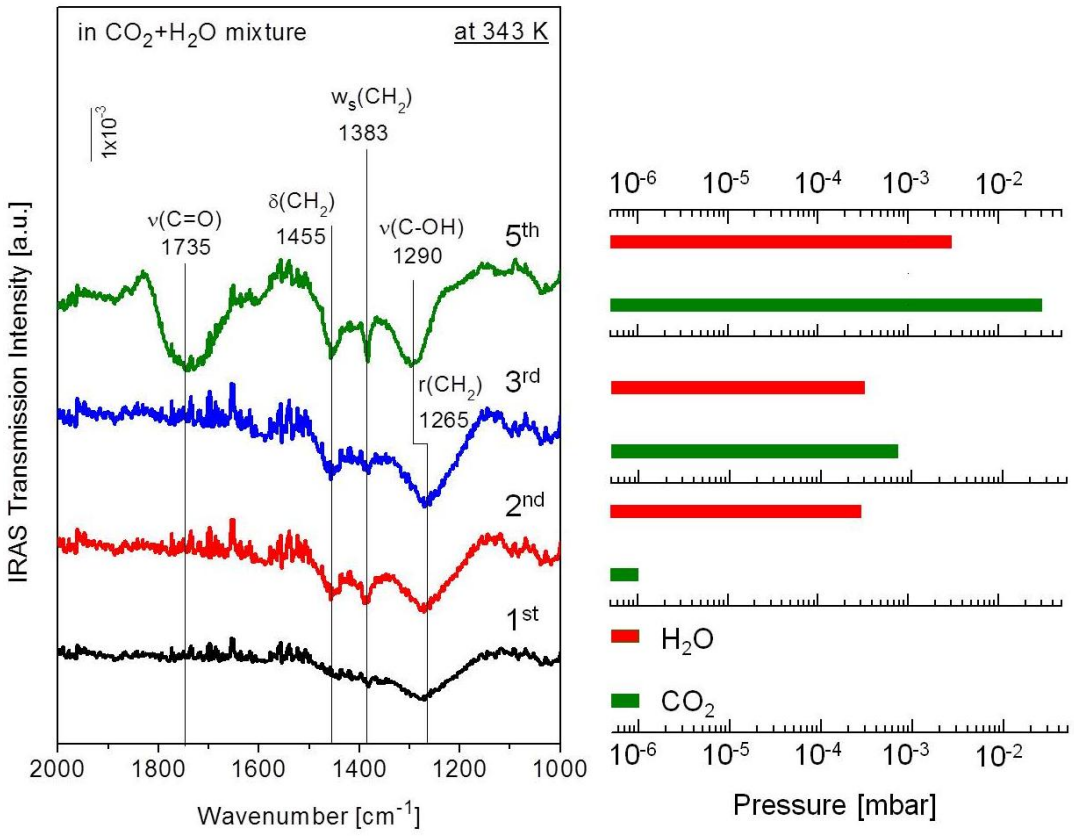

Figure 5-9. IRAS spectra of the ultrathin ZrO_2 film in different CO_2 and H_2O mixtures at 343 K. The spectra for 1st, 2nd and 3rd mixture were measured in situ. The spectra for 5th mixture were measured after evacuation of the reaction mixture (ex situ).

5.4. Summary

Our investigations show that CO_2 adsorbs only weakly on the ZrO_2 ultrathin film at UHV conditions and desorbs at 117 K during TPD experiments. At elevated pressure, pure CO_2 does not adsorb on the ZrO_2 ultrathin film at 343 K. However, CO_2 can be activated by H_2O (even by trace amounts). In situ XPS detects the formation of H_x-C-O and O-C=O species when ZrO_2 ultrathin films are subjected to CO_2 and H_2O reaction mixtures. By forming such C-related species, ZrO_2 within the ultrathin film is partially converted to Zr_x when CO_2 adsorbs on the surface. IRAS measurements of HCOOH and HCHO adsorption reveal the typical adsorption bands of the relevant functional groups. By using them as reference, H_x-C-O and O-C=O are assigned to H_2-C-O and COOH, based on the obtained IRAS absorption bands measured in CO_2 and H_2O reaction mixtures. In situ XPS also shows that the thermal stability of COOH species is less than of H_2-C-O. By cooling down the sample in the reaction mixture, the re-adsorption of COOH and H_2-C-O species is observed, indicating a temperature dependent reversible adsorption/desorption process.

Bibiliography

1. Homs, N.; Toyir, J.; de la Piscina, P. R., Chapter 1 - Catalytic Processes for Activation of CO2. In *New and Future Developments in Catalysis*, Suib, S. L., Ed. Elsevier: Amsterdam, 2013; pp 1-26.

2. Pakhare, D.; Schwartz, V.; Abdelsayed, V.; Haynes, D.; Shekhawat, D.; Poston, J.; Spivey, J., Kinetic and mechanistic study of dry (CO2) reforming of methane over Rh-substituted La2Zr2O7 pyrochlores. *Journal of Catalysis* **2014,** *316*, 78-92.

3. Kaichev, V. V.; Prosvirin, I. P.; Bukhtiyarov, V. I.; Unterhalt, H.; Rupprechter, G.; Freund, H.-J., High-Pressure Studies of CO Adsorption on Pd(111) by X-ray Photoelectron

Spectroscopy and Sum-Frequency Generation. *The Journal of Physical Chemistry B* **2003,** *107* (15), 3522-3527.

4. Bukhtiyarov, V. I.; Kaichev, V. V.; Prosvirin, I. P., X-ray photoelectron spectroscopy as a tool for in-situ study of the mechanisms of heterogeneous catalytic reactions. *Topics in Catalysis* **2005,** *32* (1-2), 3-15.

5. Azad, S.; Engelhard, M. H.; Wang, L.-Q., Adsorption and Reaction of CO and CO2 on Oxidized and Reduced SrTiO3(100) Surfaces. *The Journal of Physical Chemistry B* **2005,** *109* (20), 10327-10331.

6. Wang, J.; Burghaus, U., Structure–activity relationship: the case of CO_2 adsorption on H/Zn–ZnO(0001). *Chemical Physics Letters* **2005,** *403* (1–3), 42-46.

7. Burghaus, U., Surface chemistry of CO2 – Adsorption of carbon dioxide on clean surfaces at ultrahigh vacuum. *Progress in Surface Science* **2014,** *89* (2), 161-217.

8. P.A.Redhead, Thermal Desorption of Gases. *VACUUM* **1962,** *12* (4), 203-211.

9. Barr, T. L.; Seal, S., Nature of the use of adventitious carbon as a binding energy standard. *Journal of Vacuum Science & Technology A* **1995,** *13* (3), 1239-1246.

10. Morkel, M.; Kaichev, V. V.; Rupprechter, G.; Freund, H. J.; Prosvirin, I. P.; Bukhtiyarov, V. I., Methanol Dehydrogenation and Formation of Carbonaceous Overlayers on Pd(111) Studied by High-Pressure SFG and XPS Spectroscopy. *The Journal of Physical Chemistry B* **2004,** *108* (34), 12955-12961.

11. Rodríguez de la Fuente, O.; Borasio, M.; Galletto, P.; Rupprechter, G.; Freund, H. J., The influence of surface defects on methanol decomposition on Pd(111) studied by XPS and PM-IRAS. *Surface Science* **2004,** *566–568, Part 2* (0), 740-745.

12. Lykhach, Y.; Happel, M.; Johánek, V.; Skála, T.; Kollhoff, F.; Tsud, N.; Dvořák, F.; Prince, K. C.; Matolín, V.; Libuda, J., Adsorption and Decomposition of Formic Acid on

Model Ceria and Pt/Ceria Catalysts. *The Journal of Physical Chemistry C* **2013,** *117* (24), 12483-12494.

13. Weilach, C.; Spiel, C.; Föttinger, K.; Rupprechter, G., Carbonate formation on Al2O3 thin film model catalyst supports. *Surface Science* **2011,** *605* (15–16), 1503-1509.

14. Beamson, G.; Briggs, D., *High Resolution XPS of Organic Polymers: The Scienta ESCA300 Database*. Wiley: 1992.

15. Avery, N. R., Reaction of HCOOH with a Pt(111)-O surface; identification of adsorbed monodentate formate. *Applications of Surface Science* **1983,** *14* (2), 149-156.

16. Busca, G.; Lamotte, J.; Lavalley, J. C.; Lorenzelli, V., FT-IR study of the adsorption and transformation of formaldehyde on oxide surfaces. *Journal of the American Chemical Society* **1987,** *109* (17), 5197-5202.

17. Truong, C. M.; Wu, M. C.; Goodman, D. W., Adsorption of formaldehyde on nickel oxide studied by thermal programmed desorption and high-resolution electron energy loss spectroscopy. *Journal of the American Chemical Society* **1993,** *115* (9), 3647-3653.

18. Davydov, A. A.; Sheppard, N., *Molecular spectroscopy of oxide catalyst surfaces*. Wiley: 2003.

6. Conclusions

The objective of this thesis was to investigate the structure and properties of ZrO_2 ultrathin films that are intended to be used as well-defined model oxide support for reforming catalysts. For (UHV-) characterization of the model system, both lab-based and synchrotron-based XPS, LEED, IRAS and TPD have been employed as complementary techniques. For in situ studies, both lab-based and syntrontron-based (NAP-)XPS and IRAS have been applied to study the model system at catalytically relevant conditions of elevated gas pressure.

The ultrathin ZrO_2 film was grown on a Pt_3Zr single crystal. CO-TPD shows that the formed oxide fully covers the substrate. Synchrotron-based XPS detects two species in the oxide layer, which have different core level shifts. Depth profiling suggests that these two species are a ZrO_2 trilayer film (+2.1 eV shift relative to pure Zr) and ZrO_2 clusters (+4.2 eV shift relative to pure Zr). Upon increasing the post-annealing temperature, the oxide clusters decompose, leading to a trilayer film in the remaining area.

As the hydroxylation of metal oxides is of great importance in catalysis, the interaction of D_2O or H_2O with the ultrathin ZrO_2 film was investigated next. D_2O adsorbs on pristine ZrO_2 oxide both molecularly and dissociatively, and the dissociated D_2O desorbs recombinatively from the pristine oxide surface as D_2O molecule. On the defective oxide, D_2O also adsorbs both molecularly and dissociatively, but the D_2O dissociated on the defects quenches the defects. On defective oxide, D_2 desorption was observed. Photon-induced desorption of D_2O or ~~/~~H_2O is observed in both Lab-based and synchrotron-based XPS measurements.

The activation of CO_2 on the ultrathin ZrO_2 film was also examined. Our results show that CO_2 adsorbs only weakly on the ZrO_2 ultrathin film at UHV conditions and desorbs at 117 K

during TPD experiments. At elevated pressure, pure CO_2 does not adsorb on the ZrO_2 ultrathin film at 343 K. However, CO_2 can be activated by H_2O (even trace amounts). In-situ XPS detects the formation of H_x-C-O and O-C=O species when ZrO_2 ultrathin films are subjected to CO_2/H_2O reaction mixtures. By forming such C-related species, ZrO_2 within the ultrathin film is partially converted to Zr_x when CO_2 adsorbs on the surface. IRAS measurements of HCOOH and HCHO adsorption reveal the typical adsorption bands of the relevant functional groups. By using them as reference, H_x-C-O and O-C=O are assigned to H_2-C-O and COOH, based on the obtained IRAS adsorption bands measured in CO_2/H_2O reaction mixtures. In-situ XPS also shows that the thermal stability of COOH species is smaller than that of H_2-C-O. By cooling the sample in the reaction mixture COOH and H_2-C-O species are formed reversibly.

Publications

JOURNAL ARTICLES

H. Li, J. J. Choi, W. Mayr-Schmölzer, C. Weilach, C. Rameshan, F. Mittendorfer, J. Redinger, M. Schmid and G. Rupprechter

Growth of an Ultrathin Zirconia Film on Pt_3Zr Examined by High-Resolution X-ray Photoelectron Spectroscopy, Temperature-Programmed Desorption, Scanning Tunneling Microscopy, and Density Functional Theory

The Journal of Physical Chemistry C **2014,** *119* (5), 2462-2470.

H. Li, J. J. Choi, W. Mayr-Schmölzer, C. Weilach, C. Rameshan, F. Mittendorfer, J. Redinger, M. Schmid and G. Rupprechter

H_2O adsorption and dissociation on model $ZrO_2(111)$: UHV and elevated pressure studies

In preparation

H. Li, K. Anic, C. Weilach, C. Rameshan, A.V. Bukhtiyarov, I.P. Prosvirin, G. Rupprechter

CO_2 (and H_2O) adsorption on ZrO_2/Pt_3Zr

In preparation

J. Yang, L. Lukashuk, H. Li, K. Föttinger, G. Rupprechter, U. Schubert

High Surface Area Ceria for CO Oxidation Prepared from Cerium t-Butoxide by Combined Sol-Gel and Solvothermal Processing

Catalysis Letters, **2014,** 144 (3); 403 – 412.

Oral presentation and posters (with conference proceedings)

2012

1. H. Li, C. Weilach, G. Rupprecther
   Preparation and spectroscopic characterization of ZrO_2 thin film on Pt_3Zr
   Poster: 11th Pannonian International Symposium on Catalysis, Obergurgl, Austria; 03.09.2012-07.09.2012.

2013

1. H. Li, C. Weilach, J Choi, M. Schmid, G. Rupprecther
   Preparation and characterization of ZrO_2 thin film on Pt_3Zr
   Poster: COST Action CM1104, Vienna, Austria; 18.04.2013-19.04.2013.

2. H. Li, C. Weilach, G. Rupprecther
   Interaction of water with ultrathin ZrO2 film: From UHV to elevated pressure
   Oral: 19th International Vacuum Congress (IVC-19), Paris, France; 09.09.2013-13.09.2013

3. H.Li, K. Anic, C. Weilach, C. Rameshan, J. Choi, M. Schmid, G. Rupprechter
   Preparation and characterization of Ni particles supported by ZrO_2 thin films as model catalysts
   Oral: 15th Austrian Chemistry Days, Graz, Austria. 23.09.2013-26.09.2013

2014

1. H. Li, C. Rameshan , C.Weilach, G. Rupprechter
   A combined (in-situ) IRAS, (in-situ) XPS and TPD study of the interaction between water and Zirconium oxide
   Poster: 30th European Conference on Surface Science, Antalya, Turkey. 31.08.2014-05.09.2014

2015

1. H. Li, K. Anic, C. Weilach, C. Rameshan, A.V. Bukhtiyarov, I.P. Prosvirin, G. Rupprechter
   CO_2 (and H_2O) adsorption on ZrO_2/Pt_3Zr
   Oral: 12th European Conference on Catalysis, Kazan, Russia, 30.08.2015-04.09.2015

Oral presentation and posters (without conference proceedings)

2012

1. H. Li, C. Weilach, G. Rupprecther
   Preparation and spectroscopic characterization of ZrO_2 thin films
   Poster: 1st Annual SFB FOXSI PhD Workshop, Vienna, Austria; 10.05.2012-11.05.2012.

2013

1. H. Li, K. Anic, C. Weilach, G. Rupprechter
   Interaction of Water with Zirconium oxide-from UHV to elevated pressure
   Oral: Experimental and theoretical pizza lunch, Institute of Applied Physics; 25.01.2013

2. H. Li, K. Anic, C. Weilach, G. Rupprechter
   Interaction of Water with Zirconium oxide-from UHV to elevated pressure
   Oral: 2nd Annual SFB FOXSI PhD Workshop, Göstling/Ybbs Austria; 18.03.2013 - 21.03.2013.

3. H. Li, K. Anic, H. Holzapfel, C. Weilach, C. Rameshan, G. Rupprechter
   Preparation and characterization of Pd particles grown on ZrO_2 ultra thin film
   Poster: 2nd Annual SFB FOXSI Meeting, Schlaining, Austria; 18.09.2013 - 20.09.2013.

2014

2. H. Li, C. Rameshan , C.Weilach, G. Rupprechter
   A combined (in-situ) IRAS, (in-situ) XPS and TPD study of the interaction between water and Zirconium oxide
   Oral: 3th Annual SFB FOXSI PhD Workshop, Göstling/Ybbs Austria; 07.04.2014 - 10.04.2014.

2015

1. H. Li, K. Anic, C. Weilach, C. Rameshan, A.V. Bukhtiyarov, I.P. Prosvirin, G. Rupprechter
   CO_2 (and H_2O) adsorption on ZrO_2/Pt_3Zr
   Oral: 4th Annual SFB FOXSI PhD Workshop, Haus im Ennstal; 29.03.2015-01.04.2015

CURRICULUM VITAE

Personal Details

Name	Hao Li
Date of Birth	24.07.1986
Nationality	Chinese
Address	Kleistgasse 31/22 1030 Wien Austria
Tel	0043158801165132
E-mail	hao.li@tuwien.ac.at

Working Experience

09.2011- present	Project assistant at Vienna University of Technology, Institute of Materials Chemistry, Vienna, Austria

Education

09.2011-present	Ph.D. studies in technical chemistry, Vienna University of Technology, Vienna, Austria
04.2011-07.2011	German Courses (B1, B2) Institut für Auslandsbeziehungen, Stuttgart, Germany
10.2008-01.2011	Master Program-(Air Quality Control, Solid Waste, Waste Water Process Engineering) University of Stuttgart, Stuttgart, Germany
09.2004-07.2008	Department of Environmental Engineering Beihang University, Beijing, China

Researches

09.2011-present	In-situ spectroscopy of chemical reactions on pure and doped zirconia thin films and zirconia-based metal-oxide systems

05.2010-10.2010	Optimization of performance of catalytic system at BASF Catalysts Germany GmbH (The thesis for Master degree) ● Set up of the experiment ● Preparing the catalysts ● Characterization of the catalysts ● Tests of catalysts activities

Internship

07.2007-08.2007	Waste water treatment Department of Avic Beijing Keeven Aviation Instrument CO..LTD ● Waste water treatment using ion exchange

Internship

07.2007-08.2007	Waste water treatment Department of Avic Beijing Keeven Aviation Instrument CO..LTD ● Waste water treatment using ion exchange

Computer Abilities

Microsoft Office	Very Good
Origin	Very Good
Auto CAD	Good
Matlab and Simulink	Basic knowledge

Language Skills

English	Excellent written and spoken English
German	Good spoken German
Chinese	Mother language